

1

AD-A273 835

AFIT/GAE/ENY/93D-15



DTIC
SELECTE
DEC 16 1993

INVESTIGATION OF COMPRESSIVE
BEHAVIOR OF METAL MATRIX
COMPOSITES WITH A CIRCULAR HOLE

THESIS

Janet L. Gooder, Captain, USAF

AFIT/GAE/ENY/93D-15

93-30487

Approved for public release; distribution unlimited

93 12 15105

AFIT/GAE/ENY/93D-15

INVESTIGATION OF COMPRESSIVE BEHAVIOR OF METAL MATRIX
COMPOSITES WITH A CIRCULAR HOLE

THESIS

Presented to the Faculty of the Graduate School of Engineering
of the Air Force Institute of Technology
Air University
In Partial Fulfillment of the
Requirements for the Degree of
Master of Science in Aeronautical Engineering

Janet L. Gooder
Captain, USAF

December 1993

Accession For	
NTIS CRA&I	<input checked="" type="checkbox"/>
DTIC TAB	<input checked="" type="checkbox"/>
Unannounced	<input type="checkbox"/>
Justification	
By	
Distribution/	
Availability Codes	
Dist	Availability or Special
A-1	

Approved for public release; distribution unlimited

DTIC QUALITY INSPECTED 1

Acknowledgements

This research project was completed thanks to many generous people, to whom I owe a debt of gratitude. I thank my advisor Dr. Mall, who took time to keep me focused on an achievable goal. I am extremely grateful for Jacob Roush and Mark Derriso for their unselfish commitment to us, the graduate students. I would like to extend thanks to my sponsors at Wright Laboratory, Capt. John Pernot, NIC, Materials Directorate, and Capt. K. A. Hart, Flight Dynamics Directorate, for providing me with the materials for this study. I thank the many individuals at the Materials Directorate who generously gave of their time and expertise to help me in my research. In addition, the AFIT Model Shop responded promptly to all my fabrication requests. Their efforts were crucial to this research. Finally, my husband, Kevin, was amazing throughout this experience. I am immensely grateful for his patience, and especially for his unfailing support.

Table of Contents

Acknowledgements	ii
List of Figures	v
List of Tables	x
Abstract	xi
I. Introduction	1
II. Background	4
Sigma/Beta 21S, in Tension	5
MMCs in Tension, with Holes	5
MMCs in Compression	8
Graphite/Epoxy in Compression, with Holes	9
METCAN	10
STRESS	11
III. Methodology	13
Equipment	13
Material Fabrication	13
Specimen Preparation	16
Examination of Various Compression Test Methods	18
Test Setup and Procedure	22
Edge Replication Procedure	27
Data Acquisition	28
Post-Mortem Specimen Preparation	28
Sectioning	29
Matrix Etching	30
IV. Results	31
Analysis Based on METCAN	31
Analysis based on STRESS	35
Macromechanical Response	39
Notch Sensitivity	39
Sigma/Beta 21S, Room Temperature	46
Micromechanical Response	60
Sigma/Beta 21S, Room Temperature	60
SCS-6/Beta 21S, Room Temperature	74
SCS-6/Beta 21S, Elevated Temperature	80
V. Discussion	95
Analytical Predictions	95
METCAN	95
STRESS	97

Micro/Macromechanical Relations	98
Sigma/Beta 21S, Room Temperature	98
SCS-6/Beta 21S, Room Temperature	98
SCS-6/Beta 21S, Elevated Temperature	98
Elevated Temperature Effect	99
Macromechanical Behavior	99
Micromechanical Behavior	99
Notch Sensitivity	99
Comparison with A Previous Unnotched Compression Study	103
Comparison with Previous Notched Tension Study	103
 VI. Conclusions and Recommendations	 105
 Bibliography	 108
 APPENDIX A	 113
 APPENDIX B	 117
 APPENDIX C	 120
 Vita	 121

List of Figures

Figure 1. Room Temperature Compression Fixture	14
Figure 2. Elevated Temperature Compression Fixture	14
Figure 3. Circular Hole Produced by Ultrasonic Drill	17
Figure 4. Circular Hole Produced by Wire EDM	17
Figure 5. SCS-6/Beta 21S, Polished Edge, 100X	19
Figure 6. Sigma/Beta 21S, Polished Edge, 625X	19
Figure 7. Room Temperature Compression Fixture	23
Figure 8. Elevated Temperature Compression Fixture	25
Figure 9. Sectioning Pattern	29
Figure 10. METCAN Predictions for Room Temperature Sigma/Beta 21S	34
Figure 11. METCAN Predictions for Room Temperature SCS- 6/Beta 21S	36
Figure 12. METCAN Predictions for Elevated Temperature SCS- 6/Beta 21S	37
Figure 13. STRESS Routine Output, Stress Concentration Factors for $d/w=0.167$	40
Figure 14. STRESS Routine Output, Stress Concentration Factors for $d/w=0.4$	41
Figure 15. STRESS Routine Output, Stress Concentration Factors for $d/w=0.167$ and $d/w=0.4$, Sigma/Beta 21S	42
Figure 16. STRESS Routine Output, Stress Concentration Factors for $d/w=0.167$ and $d/w=0.4$, SCS-6/Beta 21S	43
Figure 17. Stress Concentration for SCS-6/Beta 21S and Sigma/Beta 21S, $d/w=0.167$ and $d/w=0.4$	44
Figure 18. Room Temperature Compression, Sigma/Beta 21S	48
Figure 19. Room Temperature Compression Strength, Based on Remote Area, Sigma/Beta 21S	49

Figure 20.	Normalized Strength, Room Temperature Compression, Sigma/Beta 21S	50
Figure 21.	Room Temperature Compression, SCS-6/Beta 21S	52
Figure 22.	Room Temperature Compressive Strength, Based on Remote Area, SCS-6/Beta 21S	54
Figure 23.	Normalized Strength, Room Temperature Compression, SCS-6/Beta 21S	55
Figure 24.	Elevated Temperature Compression, SCS-6/Beta 21S	57
Figure 25.	Elevated Temperature Compressive Strength, Based on Remote Area, SCS-6/Beta 21S	58
Figure 26.	Normalized Strength, Elevated Temperature Compression, SCS-6/Beta 21S	59
Figure 27.	Unnotched Sigma/Beta 21S Compression Failure	61
Figure 28.	Unnotched Sigma/Beta 21S Compression Failure	61
Figure 29.	Sigma/Beta 21S, Polished Edge of Specimen, before Testing, 850X	62
Figure 30.	Sigma/Beta 21S, Polished Edge of a Specimen Tested to 25% of Ultimate Strength, 750X	62
Figure 31.	Sigma/Beta 21S, Longitudinal Matrix Cracks at 0° Fibers, 186X	64
Figure 32.	Sigma/Beta 21S, Longitudinal Matrix Cracks at 0° Fibers, 418X	64
Figure 33.	Sigma/Beta 21S, Longitudinal Matrix Cracks between 90° Fibers, 296X	65
Figure 34.	Unnotched Sigma/Beta 21S, Fracture Surface, 25X	65
Figure 35.	Unnotched Sigma/Beta 21S, Fracture Surface, 100X	66
Figure 36.	Unnotched Sigma/Beta 21S, Fracture Surface, Showing Matrix Plasticity, 1000X	66
Figure 37.	Notched Sigma/Beta 21S, Room Temperature Compression Failure, d/w=0.167	67

Figure 38.	Notched Sigma/Beta 21S, Room Temperature Compression Failure, $d/w=0.4$	67
Figure 39.	Notched Sigma/Beta 21S, Fracture Surface, 25X	69
Figure 40.	Notched Sigma/Beta 21S, Fracture Surface, 100X	69
Figure 41.	Notched Sigma/Beta 21S, Longitudinal Fracture Surface, 150X	70
Figure 42.	Notched Sigma/Beta 21S, Longitudinal Fracture Surface, 1000X	70
Figure 43.	Notched Sigma/Beta 21S, Etched Face, Hole Boundary at 90° , 50X	71
Figure 44.	Notched Sigma/Beta 21S, Etched Face, Lateral Hole Boundary, 150X	71
Figure 45.	Notched Sigma/Beta 21S, Etched Face, Top of Hole, Showing Matrix Cracking, 50X	72
Figure 46.	Notched Sigma/Beta 21S, Etched Face, Top of Hole, Showing Matrix Cracking, 150X	72
Figure 47.	Notched Sigma/Beta 21S, Etched Face, Showing 90° Fiber Cracking, 300X	73
Figure 48.	Unnotched SCS-6/Beta 21S, Room Temperature Compression Failure	75
Figure 49.	SCS-6/Beta 21S, Polished Edge of an Untested Specimen, 45° and 90° Fibers, 400X	75
Figure 50.	SCS-6/Beta 21S, 45° and 90° Fibers of a Specimen Tested to 20% of Ultimate Strength, 334X	76
Figure 51.	SCS-6/Beta 21S, 45° Fiber of a Specimen Tested to 40% of Ultimate Strength, 500X	76
Figure 52.	SCS-6/Beta 21S, 45° Fibers Tested to 40% of Ultimate Strength, Showing Matrix Plasticity, 300X	77
Figure 53.	SCS-6/Beta 21S, Edge Replica of 90° Fibers, 50% of Ultimate Strength, Showing Radial Cracks, 300X	77
Figure 54.	SCS-6/Beta 21S, Polished Edge of a Failed Room Temperature Specimen, 100X	78

Figure 55.	SCS-6/Beta 21S, Polished Edge of a Failed, Room Temperature Specimen, Showing Slip Bands, 1000X	78
Figure 56.	SCS-6/Beta 21S, Room Temperature Specimen, Showing Matrix Deformation, 350X	79
Figure 57.	Unnotched SCS-6/Beta 21S, Fracture Surface, Showing Matrix Plasticity, 1000X	79
Figure 58.	Unnotched SCS-6/Beta 21S, Fracture Surface, Bulging Cross Section, 25X	81
Figure 59.	Unnotched SCS-6/Beta 21S, Fracture Surface, 100X	81
Figure 60.	Notched SCS-6/Beta 21S, Room Temperature Compression Failure, $d/w=0.167$	82
Figure 61.	Notched SCS-6/Beta 21S, Room Temperature Compression Failure, $d/w=0.4$	82
Figure 62.	Notched SCS-6/Beta 21S, Fracture Surface of Room Temperature Specimen, 25X	83
Figure 63.	Notched SCS-6/Beta 21S, Fracture Surface of Room Temperature Specimen, 200X	83
Figure 64.	Unnotched SCS-6/Beta 21S, Elevated Temperature Compression Failure	84
Figure 65.	SCS-6/Beta 21S, Edge Replica of Elevated Temperature Specimen, Tested to 20% of Ultimate Strength, Showing 90° Fiber Debonding	84
Figure 66.	SCS-6/Beta 21S, Elevated Temperature Specimen, 90° Fibers at 90% of Ultimate Strength, 750X	85
Figure 67.	SCS-6/Beta 21S, Elevated Temperature Specimen, 90° Fibers at 90% of Ultimate Strength, 3500X	85
Figure 68.	SCS-6/Beta 21S, Elevated Temperature Specimen, 90° Fiber at 90% of Ultimate Strength, Showing Diffusiveness of Slip and Matrix Cracking, 2000X	86
Figure 69.	Unnotched SCS-6/Beta 21S, Fracture Surface of Elevated Temperature Specimen, 34X	88

Figure 70. Unnotched SCS-6/Beta 21S, Fracture Surface of an Elevated Temperature Specimen, Showing Fiber Debonding, 100X	88
Figure 71. Unnotched SCS-6/Beta 21S, Fracture Surface of Elevated Temperature Specimen, Showing Separated C/TiB ₂ Fiber Coating, 1000X	89
Figure 72. Notched SCS-6/Beta 21S, Elevated Temperature Failure Specimen, d/w=0.167	89
Figure 73. Notched SCS-6/Beta 21S, Elevated Temperature Failure Specimen, d/w=0.4	90
Figure 74. Notched SCS-6/Beta 21S, Etched Face of Elevated Temperature Specimen, 0° Fibers at 90% of Ultimate Strength, d/w=0.4, 50X	90
Figure 75. Notched SCS-6/Beta 21S, Face of Failed Elevated Temperature Specimen, d/w=0.167, Showing 0° Fiber Debonding Near the Hole, 50X	91
Figure 76. Notched SCS-6/Beta 21S, Elevated Temperature d/w = 0.167 Specimen, Showing 45° Fiber Debonding, 39X	93
Figure 77. Notched SCS-6/Beta 21S, Elevated Temperature d/w=0.167 Specimen, 150X	93
Figure 78. Notched SCS-6/Beta 21S, Etched Face of Elevated Temperature d/w=0.167 Specimen, 10X	94
Figure 79. Notched SCS-6/Beta 21S, Etched Face of Elevated Temperature d/w=0.167 Specimen, 25X	94
Figure 80. Room and Elevated Temperature Compression, SCS-6/Beta 21S	100
Figure 81. Room and Elevated Temperature Compressive Strength, Based on Remote Area, SCS-6/Beta 21S	101
Figure 82. Normalized Strength, Room and Elevated Temperature Compression, SCS-6/Beta 21S	102

List of Tables

Table 1. METCAN Residual Stresses	32
Table 2. Sigma/Beta 21S, Room Temperature Results	46
Table 3. SCS-6/Beta 21S, Room Temperature Results	51
Table 4. SCS-6/Beta 21S, Elevated Temperature Results	53
Table 5. METCAN and Experimental Results	96
Table 6. METCAN Definitions	117
Table 7. Fiber Properties from METCAN Database	118
Table 8. Matrix Properties from METCAN Database	119

Abstract

The notched and unnotched compressive behavior of a quasi-isotropic, $[0/\pm 45/90]_n$, SCS-6/Beta 21S and a cross-ply, $[0/90]_2$, Sigma/Beta 21S metal matrix composites (MMCs) were investigated at room temperature. The compressive behavior of SCS-6/Beta 21S was also investigated at elevated temperature (650° C). The mechanical response in the presence of a circular hole was explored. Two hole sizes were used, with diameter-to-width ratios of 0.167 and 0.4. The material properties and behavior of these materials under the compressive loading condition were quantified. The progressive nature of damage, which ultimately resulted in failure, was investigated. The hole size effect in these laminates was shown. The effect of elevated temperature was illustrated for SCS-6/Beta 21S.

The ultimate compressive strength of unnotched Sigma/Beta 21S was 1943 MPa at room temperature. The elastic modulus in compression was 157 GPa, similar to the elastic modulus in tension. The ultimate compressive strength of unnotched SCS-6/Beta 21S was 2079 MPa at room temperature. The elastic modulus in compression was 139 GPa, similar to the elastic modulus in tension. The ultimate compressive strength of unnotched SCS-6/Beta 21S was 1218 MPa at 650° C. The elastic modulus was 81 GPa, similar to the elastic modulus in tension.

The failure mechanism, in both materials, involved the failure of the fibers, preceded by failure of the matrix. Therefore, ultimate compressive strength of the MMC was dependent on the strength of the fibers.

The hole size effect in the compressive loading condition had not been

previously explored for MMCs. Hole size effect was quantified through the concept of notch sensitivity. Notch sensitivity was defined as a reduction in strength more than the reduction expected solely due to the reduced area carrying the load. Notch sensitivity was assessed by a comparison of theoretical strength of the reduced area specimen and the measured ultimate strength.

This investigation showed, at room temperature, Sigma/Beta 21S exhibited a divergent trend in notch sensitivity. That is, the laminate was insensitive to the small hole size (diameter-to-width ratio = 0.167), but sensitive to the large hole size (diameter-to-width ratio = 0.4). At room temperature, SCS-6/Beta 21S exhibited mild notch sensitivity, very slightly increasing with hole size. At 650° C, SCS-6/Beta 21S exhibited mild notch sensitivity, linearly increasing with hole size.

INVESTIGATION OF COMPRESSIVE BEHAVIOR OF METAL MATRIX COMPOSITES WITH A CIRCULAR HOLE

I. Introduction

The advancement of engineering technology hinges on the discovery and creation of new materials. The properties of these new materials must be quantified in order to utilize them. Depending upon the application, certain material characteristics are more desirable than others. Light weight, high strength, and temperature resistance are material characteristics for most MMCs. These characteristics are very desirable in the aircraft and spacecraft industries.

The beauty of composite materials lies in the potential to tailor their properties for the desired application. These materials are the subject of much investigation in areas where conventional materials have limited performance of a system. MMCs are being considered for many aircraft and spacecraft designs, especially for high temperature applications. Many design possibilities arise when the material can be manufactured with the required properties in mind. (Duffy, 1990)

The notched compressive properties of MMCs are required as part of an overall mechanical behavior characterization. The notched compressive behavior of MMCs, at room and elevated temperatures, has not previously been investigated. Numerous studies are reported on the unnotched behavior of MMCs in tension (Bearden, 1992, Johnson and others, 1990, Majumdar and Newaz, 1992b and 1992c). Some research efforts have been published on the

notched behavior, at room temperature and elevated temperature, of MMCs in the static tension mode (Rattray, 1991, Roush, 1992, and Prewo, 1974). Little research work has been published on the compressive behavior of MMCs (Newaz and Majumdar, 1993 and 1992a, and Bearden, 1992). Although many graphite/epoxy composites have been characterized in the notched, compression realm (Soutis and others, 1991, Lee and Mall, 1988), no published reports are available with MMCs as the subject of such research efforts. The focus of this study is the notched behavior of MMCs subjected to static compression, at room and elevated temperatures.

The compressive behavior of two MMCs with a circular hole at room temperature is characterized and quantified. The MMCs considered are $[0/\pm 45/90]_1$, SCS-6/Beta 21S, not heat treated, and $[0/90]_2$, Sigma/Beta 21S, heat treated at 650° C for four hours in a vacuum. The notched compressive behavior of SCS-6/Beta 21S is also investigated at 650° C. Limited quantities of the Sigma/Beta 21S laminate prevented elevated temperature testing of this material. The differences between the two materials include the type of fiber, the lay-up of the lamina, and the method of preprocessing. The mechanical response of these materials is discussed through the use of strength characteristics for notched and unnotched specimens. Each material's micromechanical behavior was studied using edge replication and post-mortem analysis.

Two FORTRAN computer routines were used to predict micromechanical and macromechanical behavior. One is used to predict stress concentrations around the periphery of a circular hole in a MMC. The other is designed to predict micromechanical stresses of a MMC subjected to a variety of loading

conditions.

The specific objectives of this research are (i) to quantify the material properties and behavior under the compressive loading condition, (ii) to provide a clear description of the progressive nature of micromechanical damage prior to failure, (iii) to show the effect of holes in these materials under the given conditions, and (iv) to show the effect of loading at elevated temperature on the above characteristics.

II. Background

Research work related to this research effort is presented in this chapter. Aircraft and spacecraft must withstand compressive loads in areas where holes are included in the design. Therefore, an area of serious concern is the notched behavior of MMCs under compressive loading. However, characterization of MMCs in this condition is considerably deficient. No reports investigating the notched behavior of a MMC in the compressive loading condition were discovered.

MMCs have been the subject of many research efforts, from which insight into their mechanical behavior can be gained. MMCs have been extensively studied under the tensile loading condition. The results of a tensile behavior study presently being conducted on Sigma/Beta 21S are included in the first section. Three studies completed on MMCs in tension, with holes, are also discussed in the second section. Limited work has been completed on MMCs in the static compression realm. However, the results of two studies are presented in the third section of this chapter.

Outside of the MMCs field, many studies have been completed on the behavior of notched composite materials under static compression. The conclusions from one such study, on graphite/epoxy in the notched compression condition, are included in the fourth section.

Analytical predictions were made for this research effort through two structural analysis programs. The strengths and limitations of each is discussed, along with the application of each to the present investigation. A background on METCAN, a computer program used for mechanical response predictions, is

included in the fifth section. Finally, a background on STRESS, a computer program used to predict stress concentrations around a hole, is included in the sixth section.

Sigma/Beta 21S, in Tension

At the time of this research, the Materials Directorate of Wright Laboratory was conducting a tension study on Sigma/Beta 21S. The results of this study included the modulus of elasticity, ultimate tensile strength, and tensile yield strength of cross-ply laminates. All testing was accomplished on unnotched specimens (Ontko, 1993).

MMCs in Tension, with Holes

Awerbuch and Madhukar (1985) performed an extensive review on the notched tensile behavior of various composite materials. They collected results from multiple sources on 2800 notch strength tensile tests, covering 70 different laminate configurations. They listed intrinsic and extrinsic variables upon which fracture behavior and notch sensitivity depend. The intrinsic variables included "laminate configuration, stacking sequence, constituent properties, fiber volume fraction [sic], fiber-matrix interface characteristics, fabrication procedure, etc." The extrinsic parameters were listed as "specimen geometry, shape of discontinuity, test temperature, moisture content, loading function and history, loading rate, etc." (Awerbuch and Madhukar, 1985: 3, 89).

In this extensive study, Awerbuch and Madhukar concentrated on three composite materials: graphite/epoxy, boron/aluminum, and graphite/polyimide. They provided a discussion on the effect of laminate configuration on notch

sensitivity. In all cases, laminate configuration strongly affected notch strength and sensitivity of specimens with circular holes. Generally, multidirectional laminates were more notch sensitive than unidirectional laminates. An exception, however, was shown for boron/aluminum in a quasi-isotropic configuration. The quasi-isotropic laminate exhibited a lower notch sensitivity than unidirectional laminates. The cross-ply laminate clearly showed a stronger notch sensitivity than either unidirectional or quasi-isotropic laminates (Awerbuch and Madhukar, 1985: 104,105).

This study also provided a brief discussion of the temperature effect on notch sensitivity. While temperature had little effect on notch sensitivity of the cross-ply configuration of boron/aluminum, the results showed that the quasi-isotropic laminate became more notch sensitive at elevated temperatures (Awerbuch and Madhukar, 1985: 112).

Finally, a discussion on the effect of material system on notch sensitivity was included. The authors suggested that the comparison of notch sensitivity curves of two materials might be different for certain laminate configurations. They showed that notch sensitivity curves for the $[0/\pm 45/90]_n$ laminates of boron/aluminum and graphite/epoxy indicated graphite/epoxy was much more notch sensitive. However, when the comparison was made for the cross-ply lay-up, $[0/90]_{2n}$, the notch sensitivity was assessed to be the same for both composites. In addition, boron/aluminum showed more notch sensitivity in the $[\pm 45]_{2n}$ configuration. The discussion on the effect of the material was inconclusive due to the conflict which arose for different laminate configurations (Awerbuch and Madhukar, 1985: 123-126).

Rattray's research effort (1991) covered the characterization of SCS-

6/Beta 21S with holes under static tensile loading conditions. The MMC used in Rattray's study is virtually the same as one of the materials in this study. The fiber, matrix and lamina lay-up are the same, but the specimens were not cut from the same panel.

Rattray characterized the mechanical response of this MMC at room temperature and elevated temperature (650° C). The ultimate tensile strength was shown to be reduced by approximately 50% at high temperature. Mild notch sensitivity was evident for this quasi-isotropic lay-up of SCS-6/Beta 21S at room and elevated temperatures. That is, the strength of the notched specimens was reduced to a value less than predicted from the specimen with a reduced area. This effect was shown through the use of a net strength evaluation and a normalized strength evaluation (Rattray, 1991:65, 71, 112, 113).

The micromechanical behavior was observed through acetate replica and microscopy techniques. The damage progression was reported to begin with debonding of the fibers from the matrix at 10% of the ultimate stress of an unnotched specimen. Fiber damage occurred in the region of stress concentration adjacent to the hole at both room temperature and elevated temperature. The "strong matrix" prevented ply failure at the onset of fiber failure. Failure occurred when the matrix reached failure stress at the hole. Therefore, the notched tensile strength of the MMC was dependent upon the matrix strength (Rattray, 1991:89, 97, 100).

Roush (1992) investigated the behavior of MMCs subjected to static tension. His research focused on the characterization of cross-ply and quasi-isotropic SCS-9/Beta 21S laminates with open and filled holes. Notch

sensitivity and damage progression was discussed for room temperature and elevated temperature (Roush, 1992: 7).

Notch sensitivity assessments were made based on data collected on unnotched and notched laminates at various temperatures. The comparison of ultimate unnotched tensile strength and notched net strength showed clearly that both laminates exhibited pronounced notch sensitivity at room temperature, and complete notch insensitivity at 650° C (Roush, 1992: 128).

Damage progression, leading to failure, was identified for the laminates at room temperature and elevated temperature. Damage progression was recorded as fiber debonding, fiber failure, matrix cracking, and plasticity. This scenario occurred similarly in all laminates, with more intense evidence occurring in the vicinity of the hole (Roush, 1992: 61-62, 123).

MMCs in Compression

Newaz and Majumdar tested SCS-6/Beta 21S, in a transverse ply orientation, $[90]_8$, as opposed to the quasi-isotropic ply orientation, $[0/\pm 45/90]_{2a}$, of the present study. The tests were conducted at room temperature and at 650°C. A specially designed compression fixture, by Battelle, was used for these tests (Newaz and Majumdar, 1993:551).

Test results showed "the failure modes of a ply under transverse compressive loads may be listed as matrix shear failure or matrix shear failure with constituent debonding and/or fibre [*sic*] crushing." Also, radial fiber cracks in the loading direction were observed in sectioned specimens, indicating a low radial fiber strength (Newaz and Majumdar, 1993: 551).

In an earlier study, Majumdar and Newaz determined the mechanical response, identified inelastic deformation (in the form of plasticity and damage),

and evaluated the failure mechanisms of a MMC under compression. The MMC tested in this study was SCS-6/Ti 15-3, in unidirectional (0° and 90°) laminate configurations. Battelle's compression fixture was utilized to perform the compression testing (Majumdar and Newaz, 1992a: 49.1-49.2).

The mechanical response showed the elastic modulus in compression was identical to that in tension. Plasticity was found to be the dominant inelastic deformation mechanism in the $[0]_8$ laminates. This deformation mechanism was illustrated by the parallelism of the loading and unloading curves. However, a combination of plasticity and damage appeared in the $[90]_8$ laminates. Plasticity was shown to begin at much higher stress levels in compression than in tension (Majumdar and Newaz, 1992a: 49.3).

In the post-mortem analysis, through acetate replication and microphotography, matrix plasticity in the form of slip bands was observed in both the $[0]_8$ and $[90]_8$ specimens. Reaction zone cracks were widespread only in $[90]_8$ specimens. Additional damage was observed in the $[90]_8$ specimens as debonding of the fibers at locations 90° to the loading direction and radial fiber cracks. Radial fiber cracks were attributed to "(i) the fiber's inner soft carbon core, which provides a stress-concentration effect, and (ii) the radial columnar structure of the [chemical vapor deposition] CVD SiC fiber, with grain boundaries having lower strength than the interior of the grains" (Majumdar and Newaz, 1992a: 49.4).

Graphite/Epoxy in Compression, with Holes

Soutis and others completed one of numerous studies on the effect of holes on carbon fiber/epoxy composites under static compressive loading. The compressive strength of these carbon/epoxy composites was shown to be 30%

less than its tensile strength. They showed the mechanical response of unnotched specimens included failure of the 0° fibers due to microbuckling. The failure of these fibers occurred on two planes approximately 8-10 fiber diameters apart. This phenomenon was referred to as a "kink band". The introduction of hole in the specimens allowed them to study the compressive failure modes in greater detail, since the unnotched compressive failures occurred catastrophically (Soutis and others, 1991: 31-32).

Specimens with a centered circular hole, of diameter-to-width ratio 0.1, were tested under static compression for the purpose of analyzing failure modes. Delamination and fiber microbuckling were observed near the hole, but little damage was evident elsewhere. The introduction of a hole that reduced the area by 10% resulted in a 47% reduction in compressive strength from the unnotched specimen. The concept of notch sensitivity was exhibited through this excessive strength reduction. At 75% of the ultimate compressive strength, splitting occurred at the top and bottom of the hole boundary. At 80-85% of the failure strength, "fiber microbuckling surrounded by delamination" occurred at the edges of the hole (Soutis and others, 1991:33-34,38).

METCAN

Metal Matrix Composite Analyzer (METCAN) was developed by researchers at NASA Lewis Research Center to perform analysis of fiber reinforced MMCs (Hopkins and Murthy, 1989). METCAN, a FORTRAN program, was designed to provide a thorough analysis of thermal and mechanical behavior of MMCs through the use of mathematical models developed by Hopkins and Chamis (Hopkins and Chamis, 1988:4).

Several assumptions were involved in the formulation of the program:

(i) force equilibrium and Fourier's law for heat conduction were assumed, (ii) fibers were continuous and parallel, (iii) all fibers and their properties were identical, (iv) complete bonding existed between the fibers and the matrix, and (v) the fibers and matrix were individually isotropic or transversely isotropic (Hopkins and Chamis, 1988: 1-3).

METCAN was used to evaluate microstresses and microstrains in each ply of a multiple lamina composite. The residual microstresses and microstrains produced during processing were estimated. Using this analytical tool, the failure mechanisms and damage progression were predicted.

METCAN utilized a database containing material properties of various fibers and matrices. Utilizing this database, compression test simulations were performed for Sigma/Beta 21S and SCS-6/Beta 21S. Thermal and mechanical loads were input in the loading profile. METCAN output included micromechanical stress predictions for room temperature tests and 650° C tests.

STRESS

In 1989, Harmon, Saff, and Graves developed an analysis routine with the capability of predicting strength of notched MMC specimens. The program was capable of predicting elastic modulus, stresses around a notch, stresses through the thickness of the laminate, crack growth, and residual strength (Harmon and others, 1989: 222). The strength predictions around the periphery of a hole in a MMC were based on analysis derived by Lekhnitskii (1968: 171-186).

Roush used the equations from Lekhnitskii, Harmon, Saff, and Graves to develop a FORTRAN routine, STRESS, for the purpose of predicting stress concentrations around a hole (Roush, 1992: 149-152). STRESS required MMC

properties and geometric features as input. The longitudinal modulus of elasticity (E_x), transverse modulus of elasticity (E_y), shear modulus (G_{xy}), and Poisson's ratio (ν_{xy}) were required. For the prediction of stresses around a circular hole, the radius of the hole and the width of the specimen were required.

The value of E_x was obtained using the Rule of Mixtures. Halpin-Tsai equations were utilized to predict the transverse modulus, shear modulus, and Poisson's ratio (Agarwal and Broutman, 1990: 61, 76-86). Calculations are included as part of the Appendix of this study (Appendix A).

The STRESS program was run using the calculated properties for Sigma/Beta 21S and SCS-6/Beta 21S. Diameter-to-width ratios of $d/w = 0.167$ and $d/w = 0.4$ were used for each MMC. The output of the program included predictions of concentration factors for longitudinal, transverse, and shear stresses as a function of location on the periphery of the hole (angle from loading axis). The stress concentration factor was also provided as a function of distance from the edge of the hole.

III. Methodology

This section contains information on the equipment and techniques required to perform this research. A general description of the equipment used is presented, followed by a discussion on the composite material fabrication. Techniques used to prepare the material for testing are described in a discussion on specimen preparation. An extensive discussion on various compression test methodologies is included, along with detailed descriptions of the test fixtures utilized in this investigation. The procedures used during and following all tests are documented.

Equipment

The equipment used for this research effort included a 22 kip Materials Test System (MTS) screw machine, a high temperature MTS 25.4 mm extensometer, a Microcon 823 process control system, and a Zenith personal computer with data acquisition capabilities.

Two basic designs of compression fixtures were necessary to complete the experimentation. An adaptation of the Battelle compression fixture design was custom made for the 22 kip MTS (Fig. 1) and used for room temperature tests. A second adaptation of the Battelle design was used for elevated temperature tests (Fig. 2).

Material Fabrication

The two materials used for testing were SCS-6/Beta 21S and Sigma/Beta 21S. The common matrix, Beta 21S (also known as TIMETAL 21S), is an alloy of titanium, molybdenum, niobium, aluminum, silicon, iron,

THIS
PAGE
IS
MISSING
IN
ORIGINAL
DOCUMENT

14

and traces of oxygen, carbon, nitrogen and hydrogen. Manufacturers suggest that this alloy offers "high specific strength and good cold formability", but is especially designed for "improved oxidation resistance, elevated temperature strength, creep resistance and thermal stability" (TIMET, undated: 1).

The 142 μm diameter SCS-6 fibers were manufactured by Textron in the following manner:

A continuous SiC [Silicon Carbide] filament is produced in a tubular glass reactor by [chemical vapor deposition] CVD. The process occurs in two steps on a carbon monofilament substrate which is resistively heated. During the first step, pyrolytic graphite (PG) approximately [*sic*] 1 μm thick is deposited to smooth the substrate and enhance electrical conductivity. In the second step, the PG coated substrate is exposed to silane and hydrogen gases. The former decomposes to form beta silicon carbide (βSiC) continuously on the substrate. (Mittnick and McElman, 1988: 395)

The SCS-6 fiber surface was then coated with a 3 μm thick carbon rich compound. Coating the fiber produced a surface that would readily bond to a titanium based matrix (Mittnick and McElman, 1988: 395-398).

The 100 μm diameter Sigma fiber was developed by British Petroleum and is a continuous monofilament, composed of βSiC deposited on a tungsten core. Fiber production required two processing steps. First the Silicon carbide was deposited on the tungsten core by CVD. Then the Sigma fibers were coated with a carbon-titanium diboride (C/Ti B₂) compound that was compatible with the titanium based matrix (British Petroleum, 1991: 1-3).

Sigma/Beta 21S and SCS-6/Beta 21S were fabricated using a hot isostatic press technique. Thin sheets of matrix material (foils) alternated with layers of fibers were consolidated at high temperature and pressure to form the laminates.

Specimen Preparation

Both Sigma/Beta 21S and SCS-6/Beta 21S specimens were cut from panels using high speed diamond impregnated blades (Cooke and others, 1982: 225). The cross ply, $[0/90]_{2n}$, Sigma/Beta 21S panel was delivered in the heat treated state. The quasi-isotropic, $[0/\pm 45/90]_n$, SCS-6/Beta 21S was not heat treated before testing. Rattray tested this material without heat treating, because methods for heat treatment vary. The material properties depend on the method of heat treatment, so he tested the as fabricated material (Rattray, 1991:15). Majumdar and Newaz (1992b) examined behavior of SCS-6/Ti 15-3 in the as fabricated state. For the purpose of comparison with Rattray's unnotched and notched tensile test results, the material was not heat treated for the present study.

Notches may be machined in MMCs using various methods. Two methods were examined, in which one produced an acceptable result. An ultrasonic drilling method was to fabricate circular holes were fabricated in some specimens. The resulting holes were unsatisfactory for material testing (Fig. 3). An electronic discharge machining (EDM) method was used to produce clean holes in all the tested specimens (Fig. 4). These machining procedures were recommended by the Materials Directorate of Wright Laboratory (Larson and Russ, 1991:1-2).

All specimens were cut to 12.7 mm width. Lengths varied from 127 mm to 165 mm. Specific specimen length was not necessary because the gage length was determined by the placement of aluminum tabs prior to testing. Holes of 2.12 mm and 5.08 mm diameter were machined into the center of selected specimens. These produced specimens with diameter-to-width ratios of

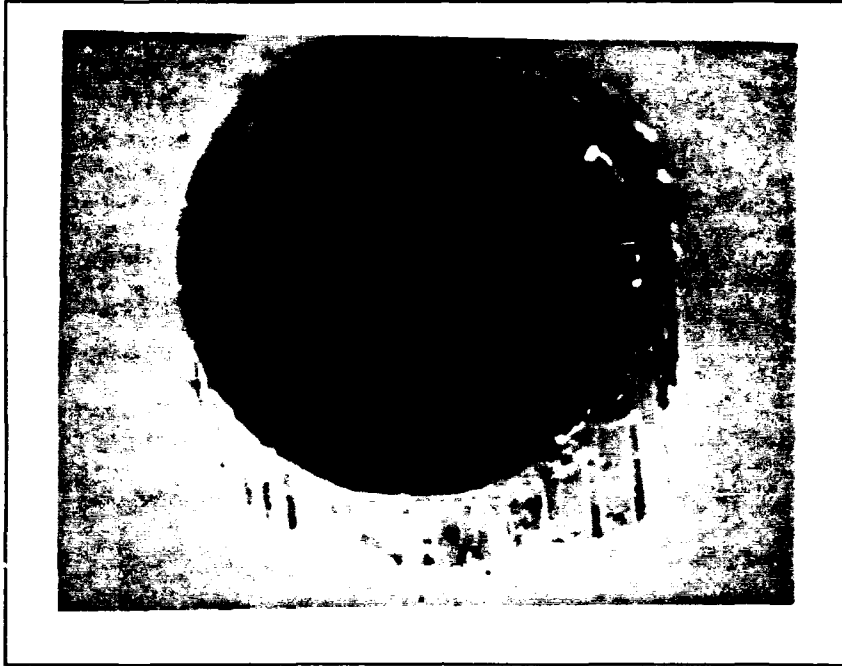


Figure 3. Circular Hole Produced by Ultrasonic Drill

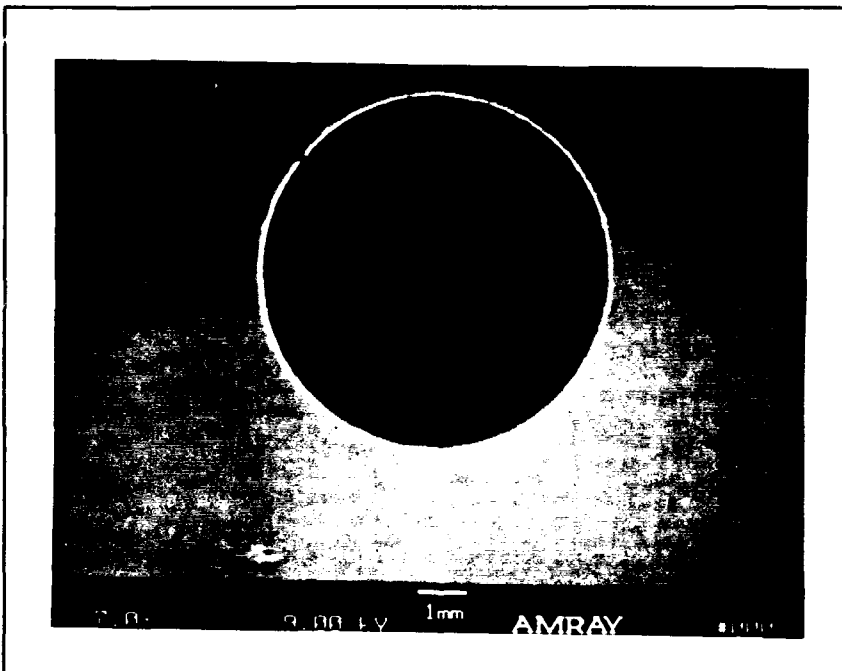


Figure 4. Circular Hole Produced by Wire EDM

$d/w=0.167$ and $d/w=0.4$.

All specimen edges were initially polished with 45 micron diamond suspension on a Metlap #8 wheel using a Buehler Maximet Specimen Preparation System (Roush, 1992:28). This initial polishing step removed any burrs from the edge of the specimens, and served to flatten the edges. Smooth, flat edges were required to prevent stress concentrations along the edges and to allow for secure placement of the extensometer rods.

For the purpose of replication of the edge surface, the edges of selected specimens were polished to a very fine finish (Figs. 5 and 6). The Metlap #8 wheel was used with 15 micron, and then 6 micron, diamond suspension to remove surface flaws. The specimens were polished using Performat cloths saturated with 15 micron smaller diamond particles. The Performat step was repeated with progressively smaller diamond suspension. The specimens were polished until the largest flaw was 1 micron. One micron clarity was necessary to detect damage in edge replicas.

Once the specimens were cut and polished to the appropriate level, aluminum tabs were applied to the ends. Aluminum tabs were used on all test specimens to insure load transfer to the specimen (Lamothe and Nunes, 1983: 243 and Tarnopol'skii and Kincis, 1985: 229). Tabs were applied, with epoxy resin compound, allowing the free gage length to exceed the buckling guide length by 2.54-3.8 mm. Tabs were held in place while the compound cured for 24 hours. Specimen width, thickness, gage length, and hole diameter measurements were recorded prior to testing.

Examination of Various Compression Test Methods

Compression testing of MMCs is one of the most difficult types of

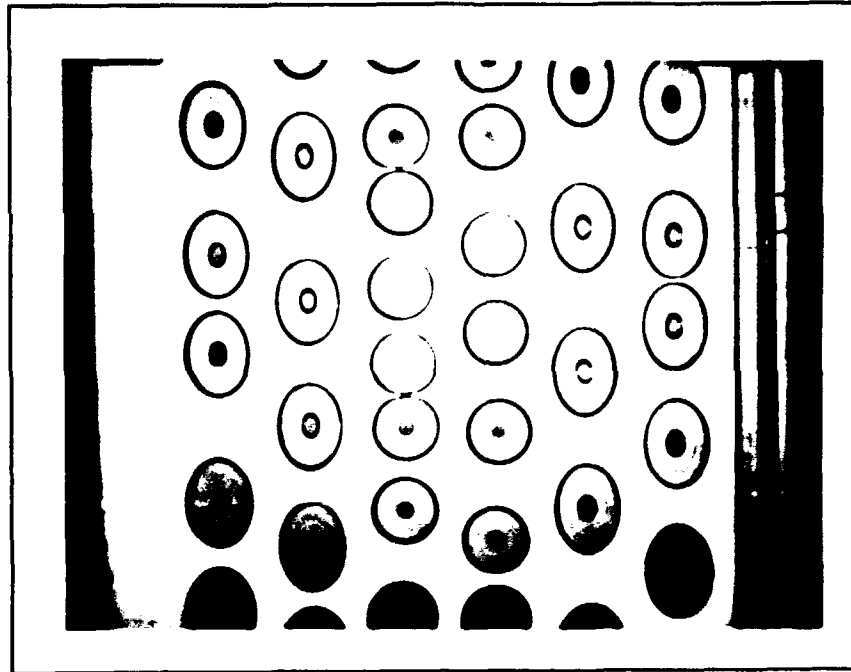


Figure 5. SCS-6/Beta 21S, Polished Edge, 100X

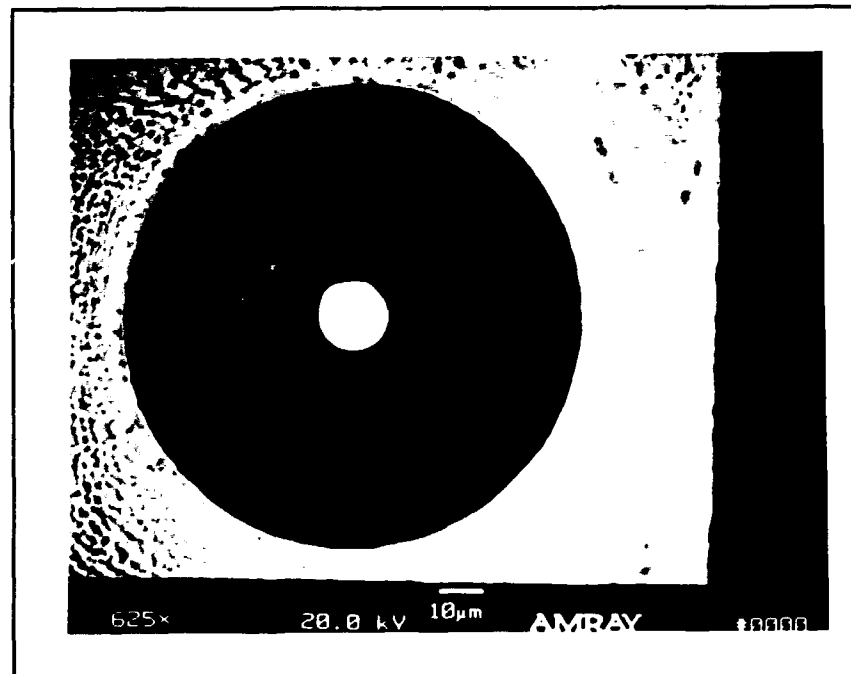


Figure 6. Sigma/Beta 21S, Polished Edge, 625X

testing because of the tendency for premature failure due to structural buckling. Several compression test methods were considered. The following discussion describes the research involved in selecting the ideal test method.

Daniel (1985) classified compression test methods into three broad categories. Type I utilized a very short, but unsupported gage length, with the load applied through end tabs. Type II used a longer gage length, with side supports on the specimen. Again, the load was applied through end tabs. In Type III, the specimen was bonded to a honeycomb core which provided the lateral support to prevent global buckling. A variation of Type III bonded the composite specimen to a honeycomb beam and produced uniform compression on the specimen through bending of the beam (Daniel, 1985:320-327).

Type I included the Illinois Institute of Technology Research Institute (IITRI) fixture, which is one of the most widely used compression testing devices. However, evidence exists supporting the possibility that the IITRI fixture provides an unsatisfactory method for compression testing of MMCs. Camponeschi reported that the IITRI fixture was not suitable for MMCs, because the required loads induced premature failure in the tab, not in the gage length. To prevent failure from occurring in the tab, thinner specimens were used. When thinner specimens were used to encourage compression failure in the gage section, structural buckling plagued the tests. The reduction of gage length, required to prevent structural buckling, made strain measurements difficult to obtain (Camponeschi, 1991:557).

Lamothe and Nunes (1983) also reported difficulty when testing MMCs with a Type I method. "Poor results were primarily attributed to buckling instability in the gage section and, in several instances, failure of the adhesive

between the aluminum tabs and the specimen" (Lamothe and Nunes, 1983: 242-245).

A Type II design, one with lateral support, is more desirable for a MMC test. Majumdar and Newaz (1992a) showed that for MMCs with 0-degree plies buckling guides were required to prevent premature failure, due to buckling and bending, in the gage section. They showed that buckling guides did not influence the stress-strain response, but prevented structural buckling in high strength composites (Majumdar and Newaz, 1992a: 49.2-49.3).

Kennedy (1989) discussed the advantages and disadvantages of the three types of compression test methods. He showed through experimental and analytical results that Type III methods (those which utilize a honeycomb structure to sandwich the specimen) were effective in preventing structural buckling without suppressing the local buckling failure mode. For Type I methods, he suggested that in order to avoid structural buckling, specimens must be relatively thick. He pointed out that, typically, MMCs were composed of thin plies and the resulting laminate was relatively thin. The expense of fabricating a thick MMC laminate was not worth the effort. The manufacturing procedure would be significantly different from that of a thin laminate, changing the properties of the laminate. Also, most applications of MMCs require thin laminates (Kennedy, 1989: 11).

Further, Kennedy claimed Type II methods inhibited the occurrence of microbuckling, which he considered a valid failure mode in compression. The steel plates bolted tightly to the specimen also carried a portion of the compressive load, because of load transfer through friction. The load carried by the fixture was determined by a strain gage mounted on the fixture. Failure in

these type of tests normally occurred outside the gage section at the end of the tab (Kennedy, 1989:11).

At Battelle, an adaptation to the IITRI fixture for testing MMCs in compression was developed. The IITRI fixture was equipped with buckling guides which provided lateral support to the specimen without carrying a significant amount of the compressive load. The guides were not designed to be in contact with the specimen until structural buckling occurred. The buckling guides were designed to limit structural buckling so that compression was the dominant loading condition, yet the failure was most likely to occur in the gage section due to the slight bending allowed. Newaz suggested that other possible buckling guide designs could produce the same buckling deterrent, while still allowing failure in the gage length mainly due to compressive loading (Newaz, 1993).

The success of Type II methods was well documented and readily available, therefore it was chosen for use in this investigation. Type III methods for testing were not considered due to the excessive cost required to fabricate the honeycomb structure.

Test Setup and Procedure

The test apparatus used for all tests was based on the Battelle compression fixture, including buckling guides (Fig. 7). The Battelle design restricted buckling of the specimen allowing failure to occur in axial compression. The guides were required to prevent the specimen's lateral movement outside of the designed buckling allowance. This crucial feature was not achievable with the original design, due to the relatively large specimen dimensions and extreme loads necessary to reach failure. To prevent excessive

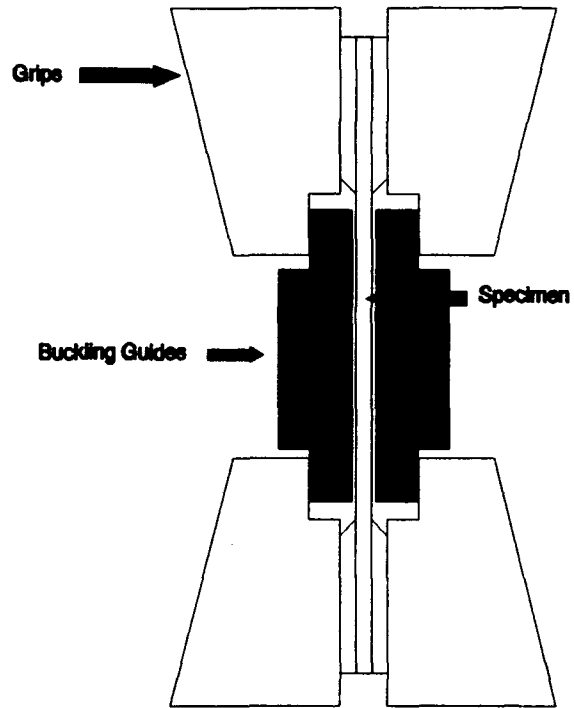


Figure 7. Room Temperature Compression Fixture

lateral movement, the buckling guides were redesigned to support the large specimen under an extreme load. The new design employed a reinforcement spar along the outside of the guide. The design effectively prevented lateral movement beyond 100 μm .

Elevated temperature tests required another design modification to the Battelle fixture. The specimen in the original fixture failed to reach 650° C, due to the heat sink produced by the direct connection of the buckling guides to the water cooled grips. The buckling guides were redesigned for elevated temperature tests. These buckling guides did not make contact with the grips (Fig. 8). Similar designs have been used in compression testing on non-metallic composites (Adams, 1991).

Using the appropriate fixture, the top tab of the specimen was first held in place using the upper servo hydraulic grips in the MTS machine. The alignment of the specimen was accomplished by the use of an aluminum block (which had previously been leveled with the test machine) held against the edge of the specimen.

Buckling guides were used for all test data. The buckling guides were lubricated using graphite machine lubricant to ensure a smooth, frictionless interface between the specimen and the guides. For room temperature tests, the buckling guides were placed in the guide slots which were custom machined into the grips. For elevated temperature tests, the buckling guides were bolted to the specimen with approximately 100 μm clearance. The lower head of the MTS was then raised such that the grip was 2.54-3.8 mm below the buckling guides.

Once the lower head was in place, the DC error was set to zero in the

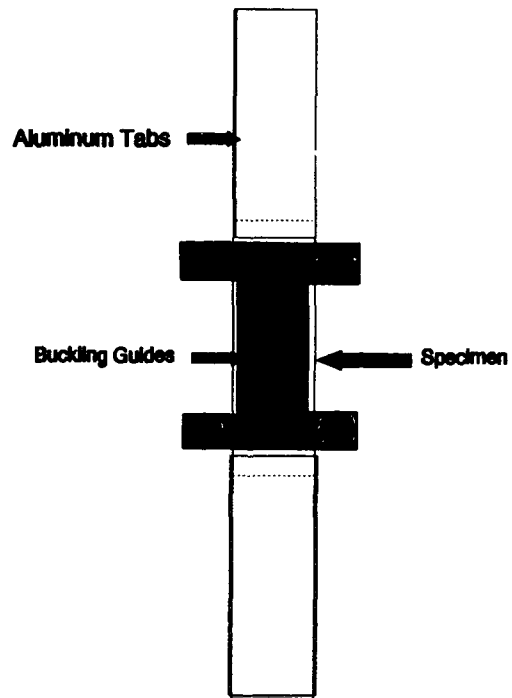
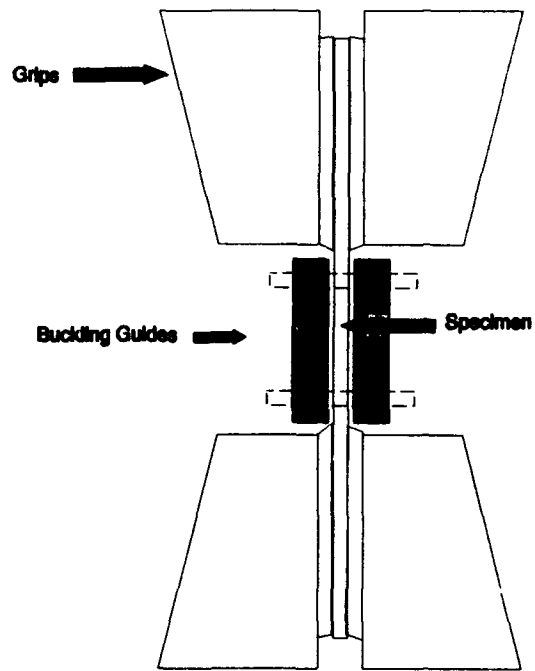


Figure 8. Elevated Temperature Compression Fixture

microprofiler, and load control was enabled. The lower tab of the specimen was immediately gripped at this point. This technique resulted in a negligible initial tensile load on the specimen (approximately 20 N).

Both room temperature and elevated temperature buckling guides were designed such that extensometer rods could be used on the edge of the specimen. The extensometer, equipped with 101.6 mm beveled quartz rods, had a gage length of 25.4 mm, as suggested by Johnson (1988: 3). The rods were securely placed on the edge of the specimen when strain measurements were necessary. For notched specimens, the extensometer always encompassed the hole.

For elevated temperature tests, radiant heat lamps were used to heat the specimen to 650° C. Newaz explained that the specimen and buckling guides reach equilibrium over time, so a thermocouple mounted to the outside of the buckling guides gave accurate specimen temperatures (Newaz, 1993). An experiment to obtain the time necessary to reach thermal equilibrium was performed. One thermocouple was tack welded to the surface of a dummy specimen and one was tack welded to the outside of the buckling guide. Ten minutes after the exterior thermocouple reached 650° C, the interior thermocouple also reached 650° C. For testing of SCS-6/Beta 21S, fifteen minutes of soak time was allotted to insure thermal equilibrium, so both thermocouples were mounted on the outside of the buckling guides.

The loading sequence used to load the specimen was input to the microprofiler. The load rate was 44.48 N/s, as recommended by the American Society for Testing and Materials standard (ASTM, 1993:5). This rate was used to compare data with results from the Rattray tensile testing (Rattray, 1991:21).

This constant load rate was used for all tests.

The load and displacement limits were set in the microprofiler to prevent the heads from forcefully coming together. The upper load limit was set to -4.448 kN. Since the test was performed under load control, the machine stopped when the specimen failed. As a precaution, the lower displacement limit was set to the location of the head when the buckling guides were in place. This precaution also prevented inadvertent loading of the buckling guides.

Edge replicas were used to evaluate the progressive nature of damage which occurred on the edge of the specimen during loading. During room temperature tests, the load was held at the desired level while the replication procedure was followed. During elevated temperature test, the load was returned to zero before the radiant heat lamps were removed and the specimen was allowed to return to room temperature. The replication procedure was followed at this point.

Edge Replication Procedure

The acetate manufacture's directions were used as a reference to obtain an effective replication procedure (Macoma, Undated). For consistency, the same replication procedure was used in all tests. A strip of acetate was attached, lengthwise, to a synthetic rubber eraser using cellophane tape. Acetone was sprayed in a narrow stream onto the highly polished edge of the test specimen. The acetate edge of the eraser was then immediately pressed to the edge with moderate hand pressure. The eraser was held still for 35 to 40 seconds. After the replication was achieved, the acetate was removed from the eraser and transferred to a glass plate. After several replicas were taken, a

second glass plate was placed on top of the replicas and held in place. The glass plate combination was then heated to approximately 70° C for 30 minutes to prevent curling of the replicas. Due to the success of this procedure, it was used for all tests. Upon completion of the replication procedure, the loading resumed at the original rate.

Data Acquisition

The stress-strain data was recorded using a data acquisition program called STATIC (Derriso and Sanders, 1992). The program required the input of the area of the specimen, the extensometer gage length used for calibration, and various user preferences for graphing. The specimen geometry and gage length information was necessary for STATIC to calculate stress and strain. During the test, the stress-strain curve was displayed on the monitor as it was being generated. The stress-strain data was automatically stored in a data file.

Post-Mortem Specimen Preparation

A great deal of post-mortem analysis through fractography and microscopy was necessary to clearly obtain the damage progression of these materials. Both optical and scanning electron microscopes (SEM) were used extensively in this research. Proper specimen preparation was critical to ensure valid analysis.

At the specimen's failure point, the MTS machine automatically stopped as it exceeded the load or displacement limits set in the microprofiler. In all cases, specimen failure occurred before the machine automatically stopped. The machine was manually stopped for tests that were accomplished to a certain percentage of the ultimate load.

Following the test, the specimen was removed from the apparatus and photographed to show the macromechanical type of failure it exhibited. The gage section was examined using an optical microscope to note any visible damage at the edge of the specimen.

Edge replicas were examined under the optical microscope to determine the existence of damage. Replicas that showed indications of damage were coated with gold-palladium (Johnson, 1988: 5). The tinted coating enhanced the features of the originally clear edge replica.

Sectioning. For post-mortem analysis, the specimen was divided into small sections for close examination. The gage section was cut from the tab section using a low speed diamond saw. Some gage sections were then carefully sectioned such that the longitudinal, transverse and face sections of the specimen could be observed (Fig. 9).

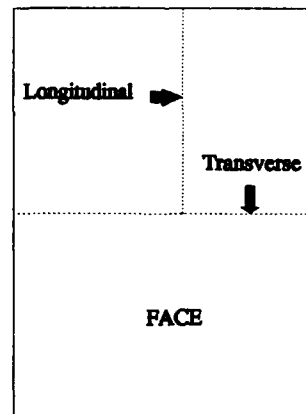


Figure 9. Sectioning Pattern

The sections were cleaned to remove grease, moisture, or other impurities that detract from the specimen features. The fracture surfaces were ultrasonically cleaned in acetone, followed by freon, and baked in a vacuum furnace (90° C) for 72 hours. Longitudinal and transverse surface sections were mounted in Epomet molding compound and polished, in the same fashion as the pre-test specimen, to a 3 micron surface. The polished surface was essential to facilitate examination under high magnification in the SEM. The mounted sections were ultrasonically cleaned in the same manner as for the fracture surface sections.

Matrix Etching. Several notched specimens were prepared for examination, after testing, by removing matrix material to expose the fibers. This technique of matrix removal is called etching. The area of the specimen surrounding the hole was exposed to an acidic compound, Kroll's etching compound (Roush, 1992: 87). Following the etching procedure, the specimens were ultrasonically cleaned with acetone and freon to remove contaminants, then baked in a vacuum furnace (90° C) for 72 hours.

IV. Results

Sigma/Beta 21S and SCS-6/Beta 21S laminates were analytically and experimentally examined in this study. Computer codes were used to provide theoretical analysis, while compression testing was used to produce experimental results. Composite properties and mechanical behavior were quantified, and the progressive nature of damage was evaluated. The hole size effect on these two MMCs was studied. Variations in these characteristics, resulting from elevated temperature testing, were quantified. Comparisons between theoretical predictions and experimental results are included in chapter V.

This chapter is divided into four sections. The first section is a presentation of analytical predictions for composite properties and damage progression. The second section includes the analytical predictions for the hole effect in a MMC. The third section is a presentation of macromechanical behavior of the MMCs. Macromechanical behavior consists of the composite properties and behavior, in terms of stress-strain response and notch sensitivity. The last section contains information on the micromechanical behavior of the MMCs. Micromechanical behavior consists of damage progression, leading ultimately to specimen failure.

Analysis Based on METCAN

METCAN (Hopkins and Murthy, 1989) was used to simulate compressive loading on a MMC specimen. This computer program was used to predict micromechanical stresses, composite properties, and failure progression.

METCAN calculated micromechanical stresses in each lamina at

incremental loading steps. The mechanical load profile was defined in an input file. The input file also contained the thermal loading profile, ply orientation, lamina thickness, and output format. The output provided composite properties, constituent (component) total stresses and strains for each ply, and information for current load/time step (Hopkins and Murthy, 1989).

Residual stresses are the stresses produced while cooling the laminate from its fabrication temperature. These residual stresses are created when the matrix and fiber have different coefficients of thermal expansion (Agarwal and Broutman, 1990: 235). Beta 21S matrix has a greater coefficient of thermal expansion than either the Sigma or SCS-6 fiber. Thus, residual stresses exist in Sigma/Beta 21S and SCS-6/Beta 21S laminates.

METCAN predicted residual stresses in the laminates at room temperature. The residual stresses were assumed to be negligible at the fabrication temperature of 815° C (Majumdar and Newaz, 1992a, and Santhosh and others, 1992). METCAN simulated cooling the specimen from 815° C to room temperature, 23.9° C, to predict residual stresses. The simulated cooling process was accomplished in three thermal load steps. The maximum residual stresses in each laminate are tabulated from the METCAN output in Table 1.

Table 1. METCAN Residual Stresses

Maximum Residual Stresses			
Sigma/Beta 21S		SCS-6/Beta 21S	
Matrix	Fiber	Matrix	Fiber
297.5 MPa	-486.6 MPa	272.0 MPa	-397.1 MPa

METCAN required a database of material properties containing the

component (fiber, matrix, and interface) properties. The Sigma fiber properties were obtained from the manufacturer (British Petroleum, 1991). The SCS-6 fiber properties were obtained from Hansen's work (1991: 119). The Beta 21S properties, at room temperature and 650° C, were obtained from the Materials Directorate of Wright Laboratory (Ashbaugh, 1993). The interface was not modeled because the properties are unknown. The database, for the relevant fibers and matrix, is included in Appendix B.

"METCAN implements a model which simulates the degradation of constituent material properties due to cumulative mechanical and thermal load cycles" (Hopkins and Murthy, 1989: 5). The load cycles are defined in the input file by specification of consecutive load steps. For room temperature simulations, mechanical loading began immediately after the cooling sequence, which was accomplished in three thermal load steps. Thermal loading for elevated temperature simulations began after the cooling sequence, or load step three. The heating sequence was accomplished in five thermal load steps to reach the test temperature, 650°C. For elevated temperature test simulations, mechanical loading began immediately following the heating sequence, or load step eight. The mechanical load steps correspond to stress applied to the laminate.

The investigation of simulated damage progression began by plotting the maximum stresses in each ply against the current load step, beginning with the last thermal load step. The room temperature simulation for Sigma/Beta 21S showed that matrix yielding may occur in the 90° plies at 600-800 MPa of applied stress (Fig. 10). Matrix yielding may occur in the 0° plies at 1600-1800 MPa of applied stress. The fibers would not break at 2000 MPa of

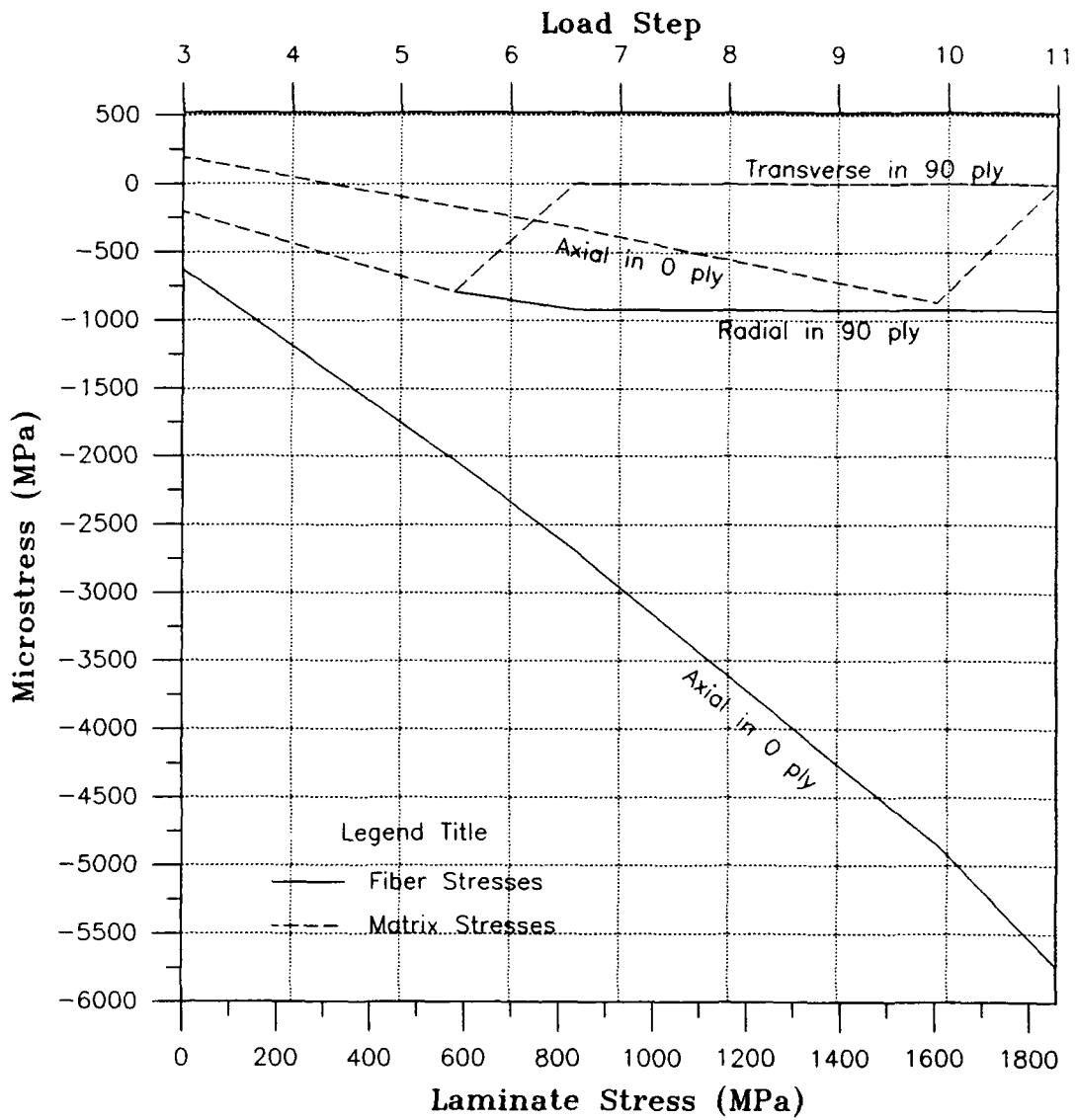


Figure 10. METCAN Predictions for Room Temperature Sigma/Beta 21S

applied stress on the laminate.

The room temperature simulation for SCS-6/Beta 21S showed that fibers may break in the 45° plies at 600-800 MPa of applied stress (Fig. 11). Matrix yielding may occurred in the 90° plies at 800-1000 MPa of applied stress.

Fiber breakage may occur in the 0° plies at 1200-1400 MPa of applied stress.

The elevated temperature simulation on SCS-6/Beta 21S showed trends, similar to those for the room temperature predictions (Fig. 12). Matrix yielding may occur in the 45° and 90° plies at 350-400 MPa of applied stress. Fiber breakage may occur in the 45° plies at 500-550 MPa of applied stress.

Analysis based on STRESS

The FORTRAN routine, STRESS, written by Roush, was used to predict the circular hole effect in the MMC laminates (1992: 149-153). STRESS calculated the stress concentration factor, due to the presence of a circular hole, in a composite specimen. The program was based on a mathematical formulation by Harmon, Saff, and Graves (1989). The formulation was an adaptation of Lekhnitskii's mathematical model for stress distribution around a circular hole in an infinitely wide orthotropic plate (Lekhnitskii, 1968). The model was adapted for finite width composite materials by Harmon, Saff and Graves.

The required inputs for STRESS were the laminate's longitudinal, transverse, and shear moduli. Additional input requirements included the geometric features of hole radius and specimen width. The output was the stress concentration factor, as a function of angle from the loading axis. An optional output was stress concentration factor at 90° from the top of the hole, $\theta=90^\circ$, along the transverse axis.

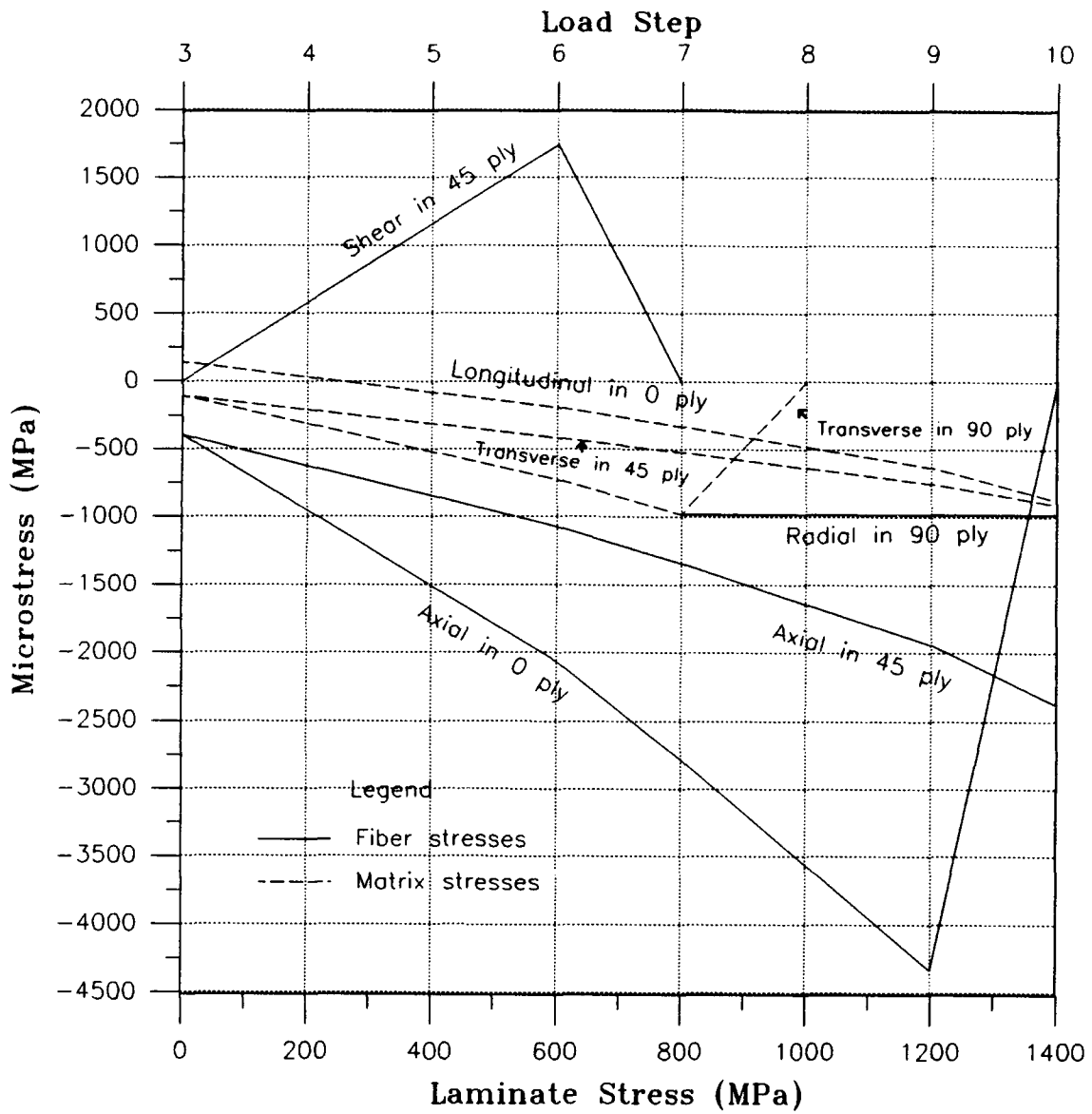


Figure 11. METCAN Predictions for Room Temperature SCS-6/Beta 21S

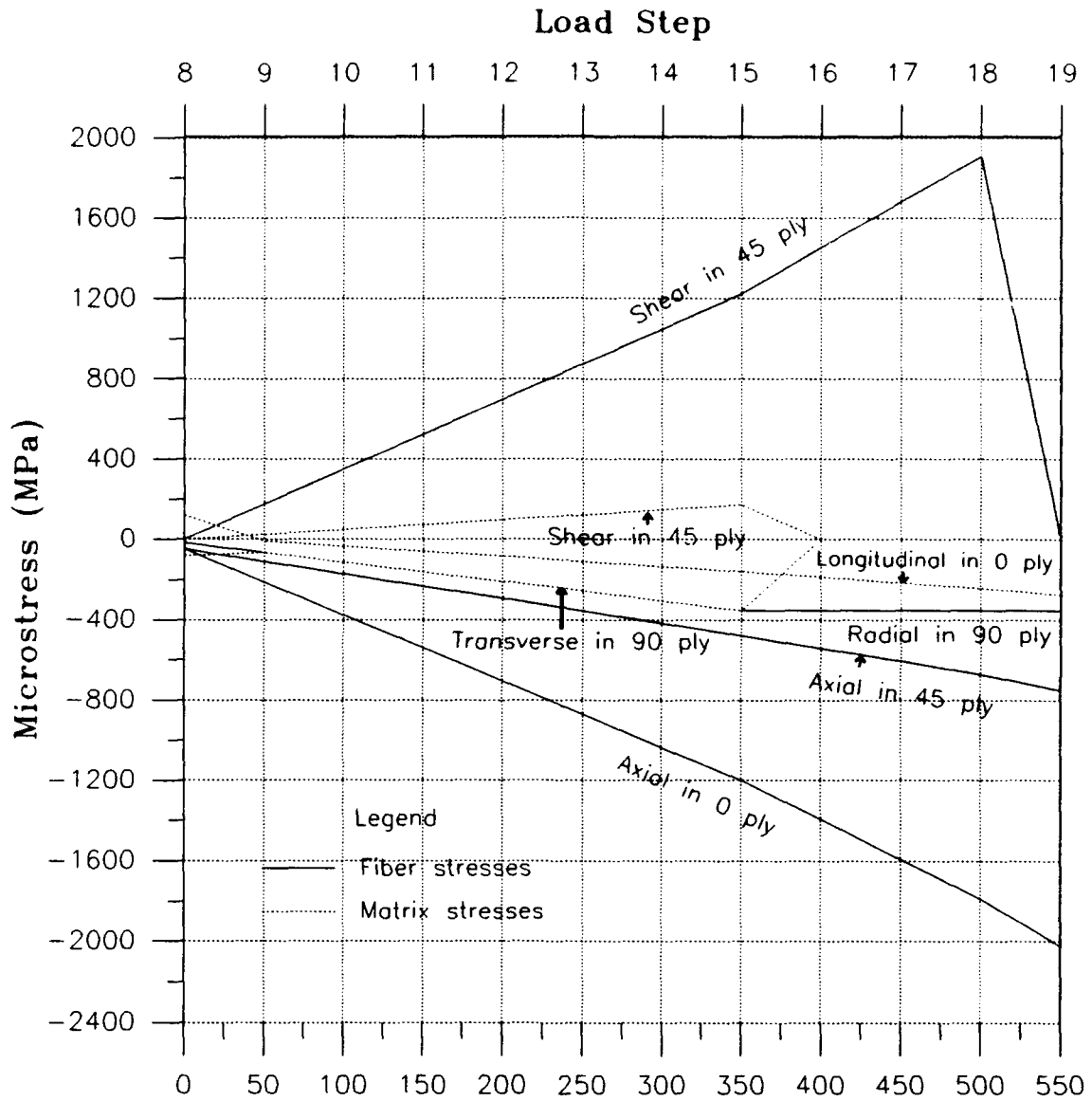


Figure 12. METCAN Predictions for Elevated Temperature SCS-6/Beta 21S

Roush's program utilized equations from Lekhnitskii's model for unidirectional loading of a laminate with a circular hole. Stress concentration factors relating tangential stress at the hole, σ_{tan} , to the gross applied stress, σ_{gross} , were calculated :

$$\sigma_{tan}/\sigma_{gross} = \frac{E_t}{E_x} \left[\frac{1}{2} (1 + \eta - \sqrt{\frac{E_x}{E_y}}) - \frac{1}{2} (1 + \eta + \sqrt{\frac{E_x}{E_y}}) \cos 2\theta \right] \quad (1)$$

where

$$\eta = \sqrt{\frac{E_x}{G_{xy}} - 2\nu_{xy}} + \sqrt{\frac{E_x}{E_y}} \quad (2)$$

and θ is the angle measured from the loading axis, x. The stress concentration factor at the top of the hole, $\theta=0$, was defined as K_{t0} . Equation (1) reduced to $K_{t0} = -(E_y/E_x)^{1/2}$, when $\theta=0$. The stress concentration factor at the edge of the hole, $\theta=90$, was defined as K_t . Equation (1) was simply $K_t = 1 + \eta$ for that case. These relations were substituted into equation (1) and the resulting equation was coded in the STRESS program:

$$\sigma_{tan}/\sigma_{gross} = \frac{1}{2} \left[\frac{E_t}{E_x} K_t + \frac{E_t}{E_y} K_{t0} \right] - \frac{1}{2} \left[\frac{E_t}{E_x} K_t - \frac{E_t}{E_y} K_{t0} \right] \cos 2\theta \quad (3)$$

Roush incorporated a finite width correction factor into the program. The correction factor, developed by Tan, mathematically changed the circular hole to an elliptical hole to account for finite width (Tan, 1988).

STRESS's output showed that stress concentration factors for each laminate were extreme at the edge of the hole, where $\theta=90^\circ$. The program was run for two hole sizes, $d/w=0.167$ and $d/w=0.4$. Slightly higher longitudinal and transverse stress concentrations were predicted for the Sigma/Beta 21S than for SCS-6/Beta 21S (Figs. 13 and 14). The shear stress concentration factor was not significantly affected by the change in materials. The same data showed a more significant increase in longitudinal and transverse stress concentration factor, caused by the increased hole size. These factors at $\theta=90^\circ$ increased by 20% for the larger hole size. This increase was observed in the data of both Sigma/Beta 21S and SCS-6/Beta 21S (Figs. 15 and 16).

The stress concentration factor for both laminates was graphed as a function of transverse distance from the center of the hole (Fig. 17). This graph showed the stress concentration gradient was very similar for each hole size, but the larger hole produced a significantly higher stress concentration factor at the edge of the hole. These results led to the prediction that damage would occur at the edge of the hole, because of the magnification of stresses at that point.

Macromechanical Response

The macromechanical response is the external behavior of the material. In this section, the laminate as a whole is considered. External behavior analysis included the evaluation of the laminate's modulus of elasticity and strength properties. The stress-strain information is part of the macromechanics discussion. A notch sensitivity assessment is made in this section through the use of net strength and normalized strength curves. Finally, the effect of elevated temperature on these characteristics is included for SCS-6/Beta 21S.

Notch Sensitivity. Notch sensitivity has been used to describe the

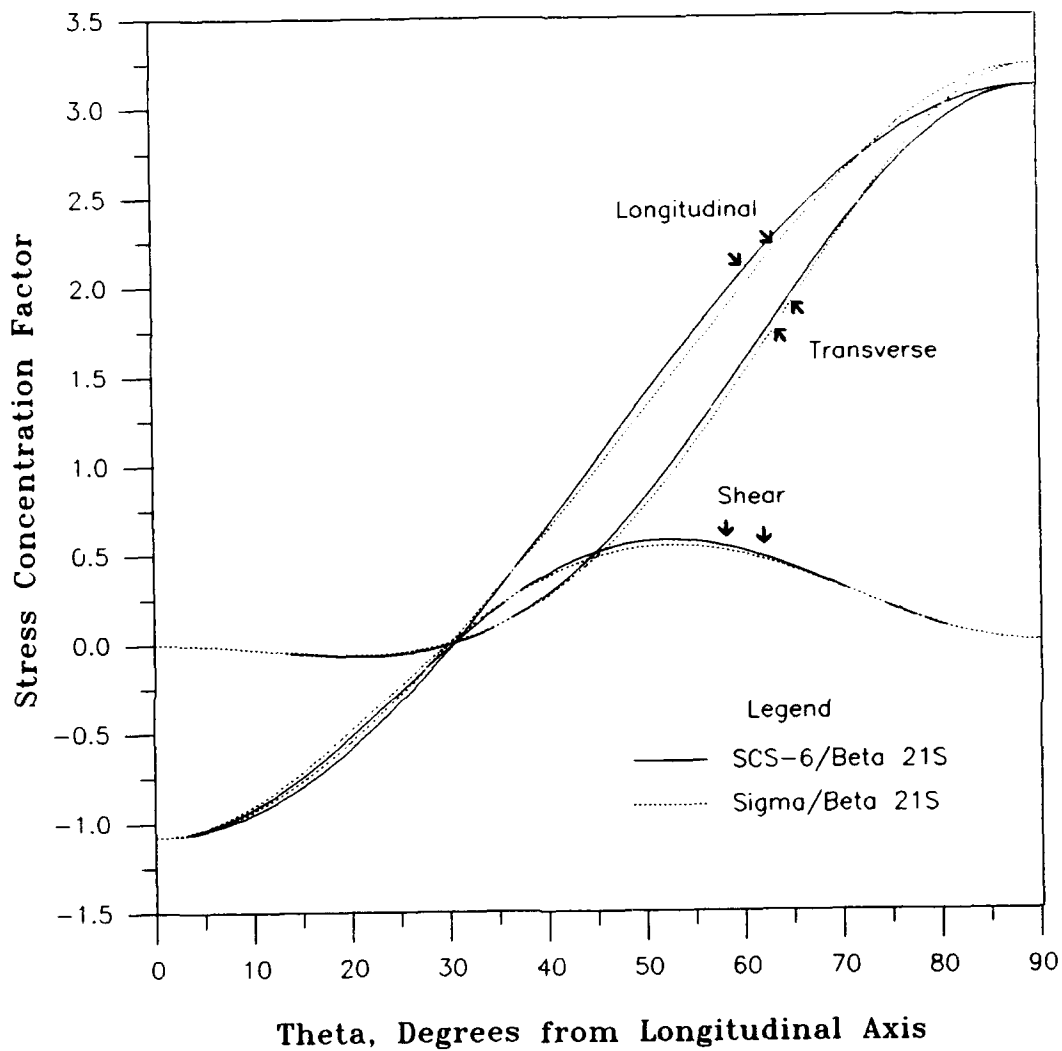


Figure 13. STRESS Routine Output, Stress Concentration Factors for $d/w=0.167$

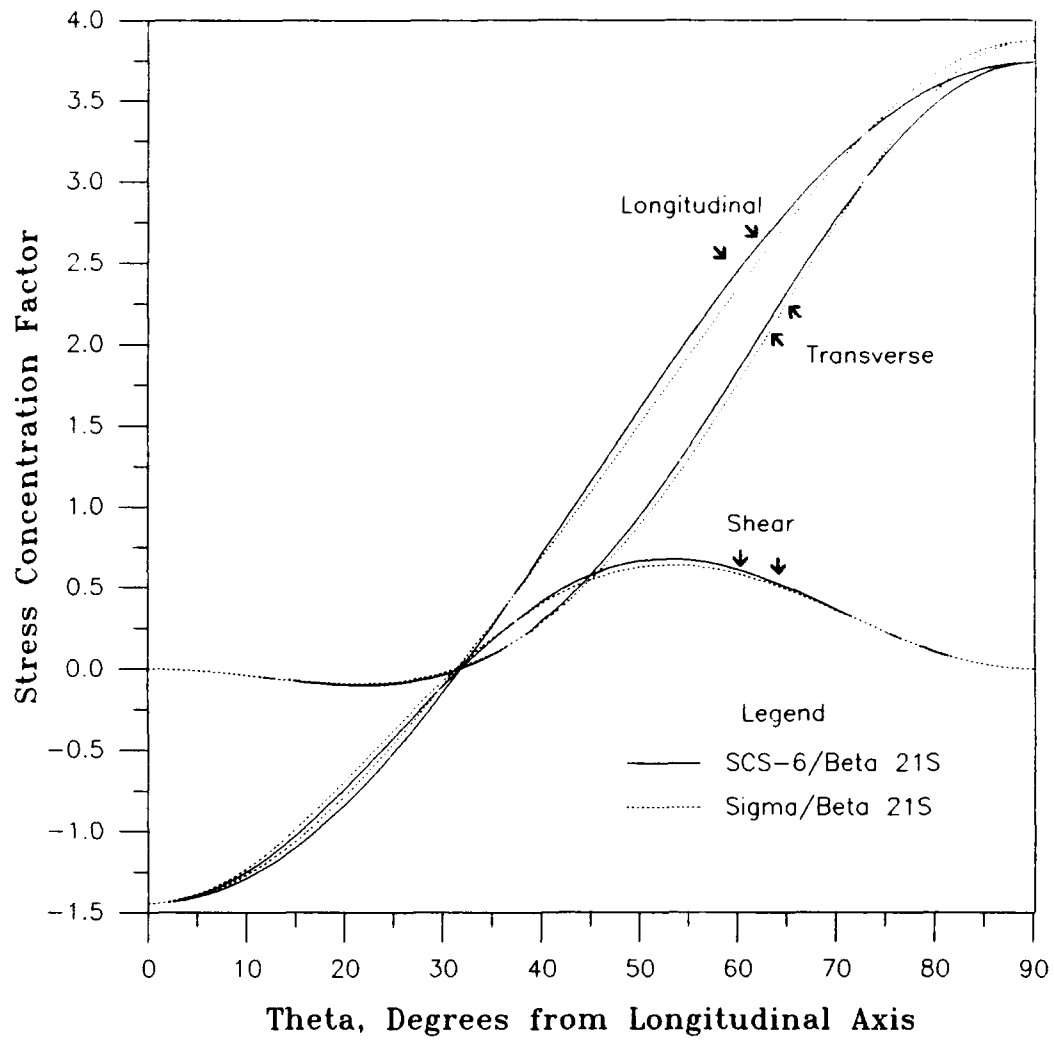


Figure 14. STRESS Routine Output, Stress Concentration Factors for $d/w=0.4$

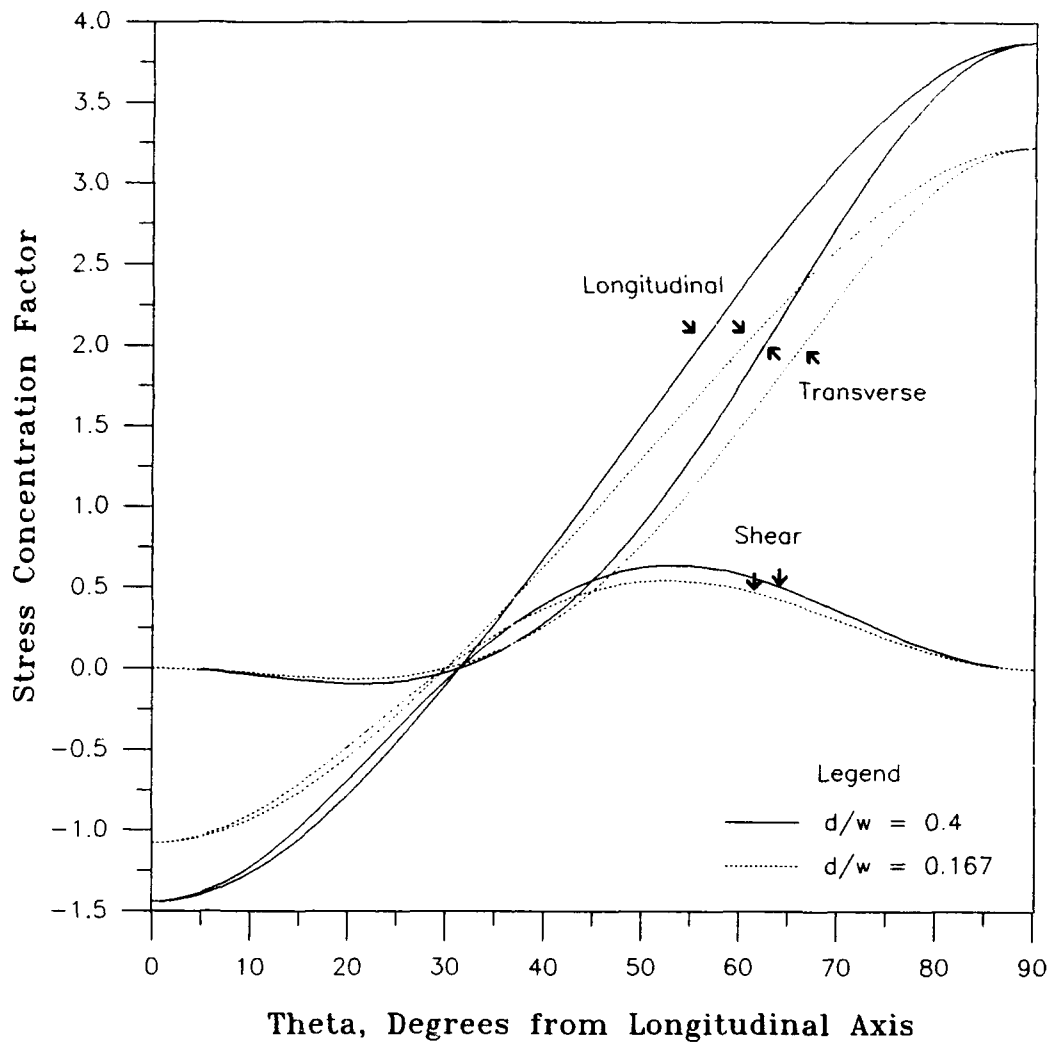


Figure 15. STRESS Routine Output, Stress Concentration Factors for $d/w=0.167$ and $d/w=0.4$, Sigma/Beta 21S

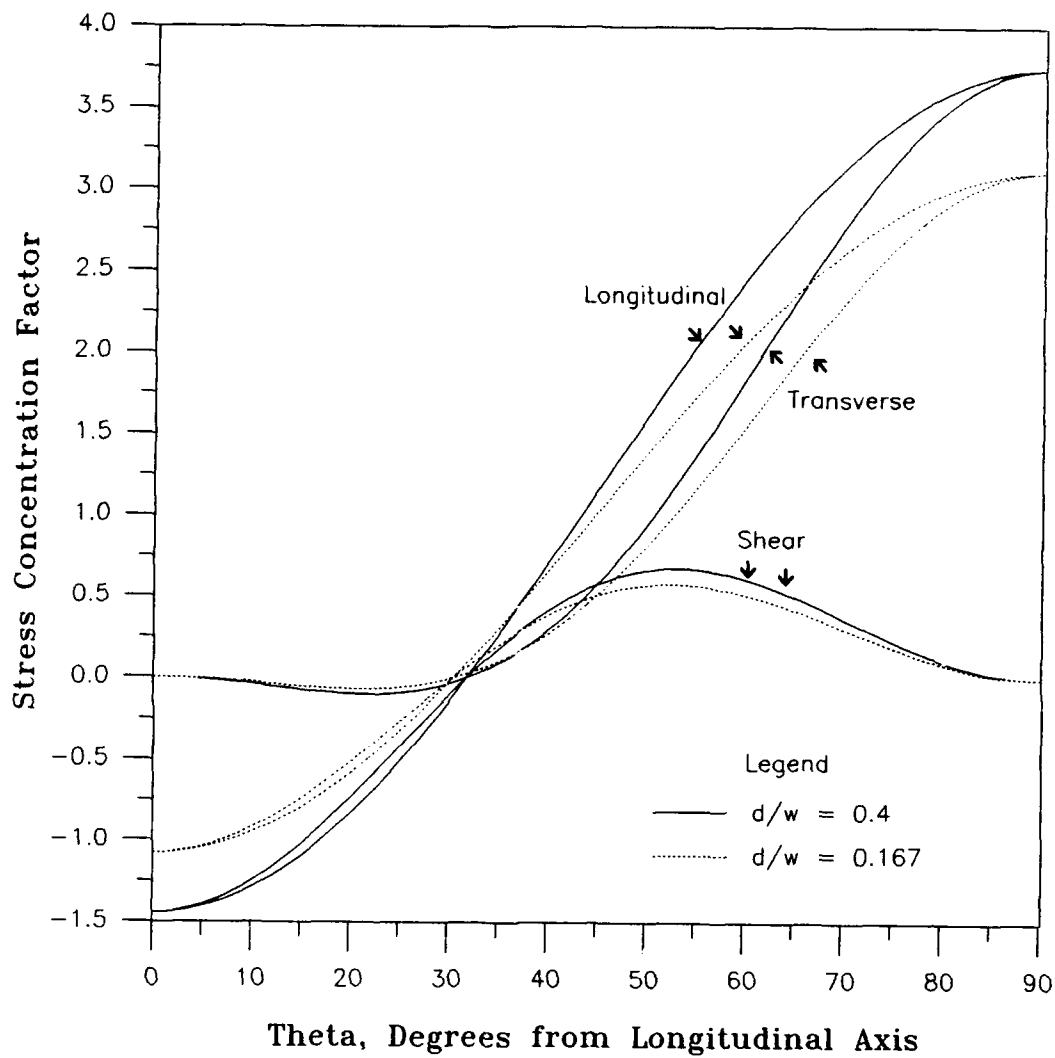


Figure 16. STRESS Routine Output, Stress Concentration Factors for $d/w=0.167$ and $d/w=0.4$, SCS-6/Beta 21S

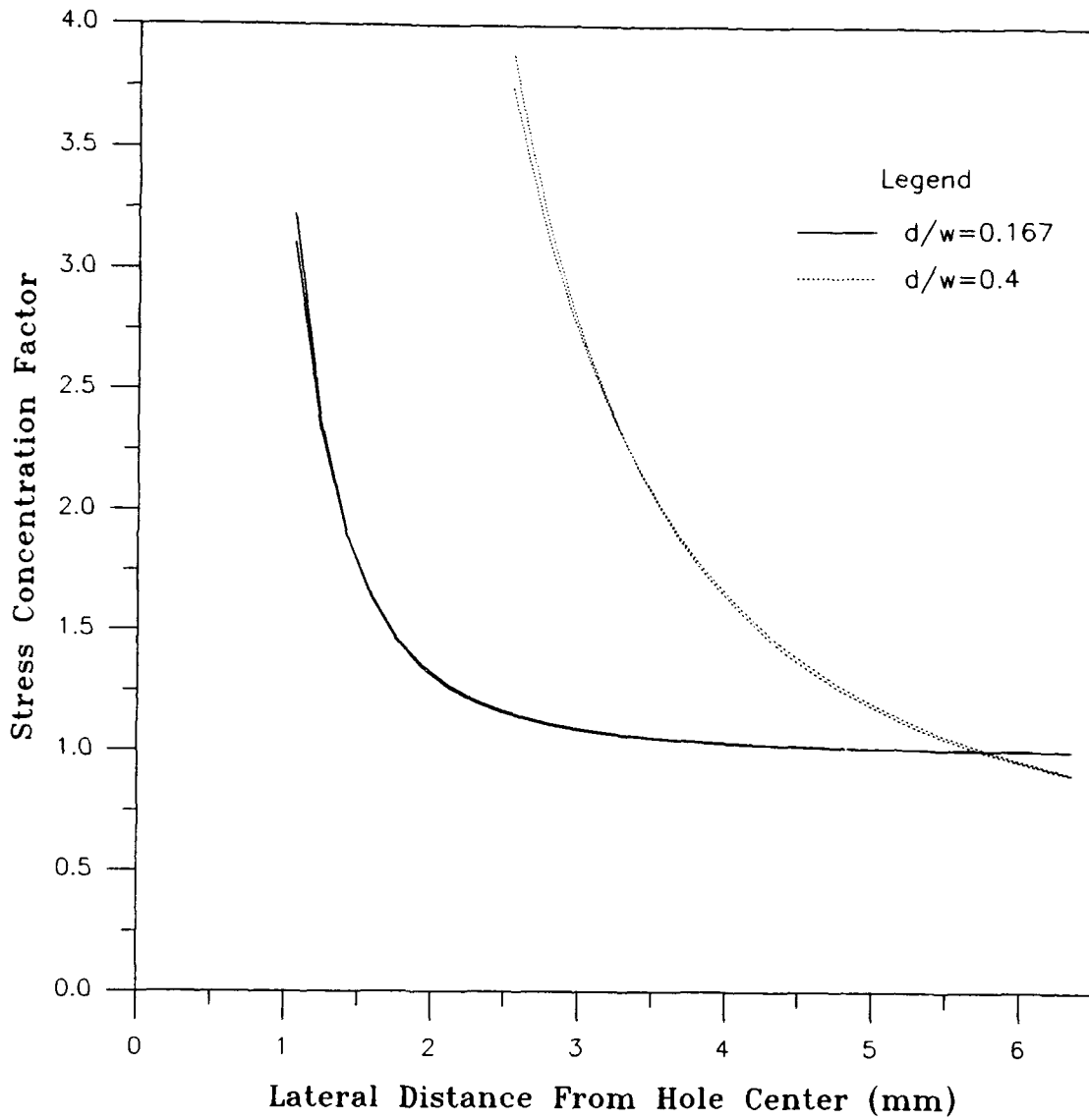


Figure 17. Stress Concentration for SCS-6/Beta 21S and Sigma/Beta 21S, $d/w=0.167$ and $d/w=0.4$

response of a material in the presence of a notch (or hole). Notch sensitivity is defined as a reduction in strength more than the reduction expected solely due to the reduced area carrying the load (Roush,1992:98).

Notch sensitivity was assessed utilizing the laminate's theoretical net strength. Net strength of a notched specimen was defined as the strength of a rectangular specimen with a cross sectional area equivalent to the reduced area of the notched specimen (Roush, 1992:98). Mathematically, $\sigma_{net} = P_f / A^*$, where σ_{net} is the net strength, P_f is the measured failure load, and A^* is the area of the reduced cross section. The net strength can also be shown as:

$$\sigma_{net} = \frac{\sigma_o}{1-d/w} \quad (4)$$

given

$$\sigma_o = \frac{P_f}{A} \quad (5)$$

where σ_o is the applied stress, d/w is the diameter-to-width ratio, and A is the remote area (see Appendix C).

Two techniques for notch sensitivity assessment were duplicated from Rattray's work. The first technique utilized net strength to show the effect of a circular hole in the cross section of a tensile specimen. The theoretical net strength was calculated, based on the corresponding strength of the unnotched specimen. Notched specimen strengths, based on remote area, were compared to the theoretical net strength curve. The second technique utilized the normalized strength of the notched and unnotched specimens. Normalization

was achieved by dividing net strength by unnotched strength:

$$\sigma_{norm} = \frac{\sigma_{net}}{\sigma_{unnotched}} \quad (6)$$

Rattray explained that a material was notch insensitive when its normalized strength is unity, regardless of the hole size (Rattray, 1991:65).

The net strength and normalized strength analysis techniques were employed in this study for all room temperature and elevated temperature tests to aid in the assessment of notch sensitivity. A comparison of notch sensitivity of SCS-6/Beta 21S, for room and elevated temperatures, is included in chapter V.

Sigma/Beta 21S, Room Temperature. The macromechanical behavior of Sigma/Beta 21S at room temperature was observed through a series of compression tests. The summary of these test results are provided in Table 2.

Table 2. Sigma/Beta 21S, Room Temperature Results

Material	Test Temp. (°C)	d/w	Area (mm ²)	Ultimate Load (kN)	Ultimate Strength (MPa)	Net Strength σ_{net} (MPa)	Norm Strength σ_{net}/σ_o	Elastic Modulus (GPa)
Sigma/B 21S	22.2	0	15.01	29.15	1943	1943	1	157
Sigma/B 21S	22.8	0.17	13.80	21.94	1590	1910	0.98	149
Sigma/B 21S	22.2	0.17	13.57	21.68	1597	1928	0.99	
Sigma/B 21S	23.9	0.39	14.05	13.90	990	1630	0.84	
Sigma/B 21S	23.3	0.40	13.58	13.03	960	1599	0.82	125

Sigma/Beta 21S exhibited an ultimate compressive strength at room

temperature was nearly three times its tensile strength. The ultimate compressive strength was 1943 MPa, while Ontko reported an average ultimate tensile strength of 710 MPa (Ontko, 1993). The elastic modulus in compression, 157 GPa, was similar to the elastic modulus in tension, 153 GPa (Newaz, 1992, and Ontko, 1993).

Stress-strain curves for unnotched and notched Sigma/Beta 21S specimens were plotted on one graph to show the variations due to the circular hole (Fig. 18). The reduction in elastic modulus (slope of the linear portion of the curve) of notched specimens was due to the extensometer used over the gage length encompassing the hole. The curves were predominantly linear, indicating mostly elastic deformation. Non-linearity, due to plasticity and damage, occurred only in the last 20% of loading. The strength reduction, due to the hole, can clearly be seen in the graph.

Notch sensitivity was evaluated through the use of a theoretical net strength line. Points on the line were calculated using Equation (4). The net strength line was the basis to which experimental values were compared to assess notch sensitivity.

Using the net strength line, Sigma/Beta 21S was assessed to exhibit a divergent trend in notch sensitivity (Fig. 19). The curve showed that the smaller hole did not reduce specimen strength, however, the larger hole reduced the strength 16% from the theoretical net strength.

The normalized strength of the laminate was calculated for each experimental ultimate compressive strength, using Equation (6). The normalized strengths were displayed in a graph as a function of diameter-to-width ratio (Fig. 20). The data points showed the same divergent trend in notch sensitivity

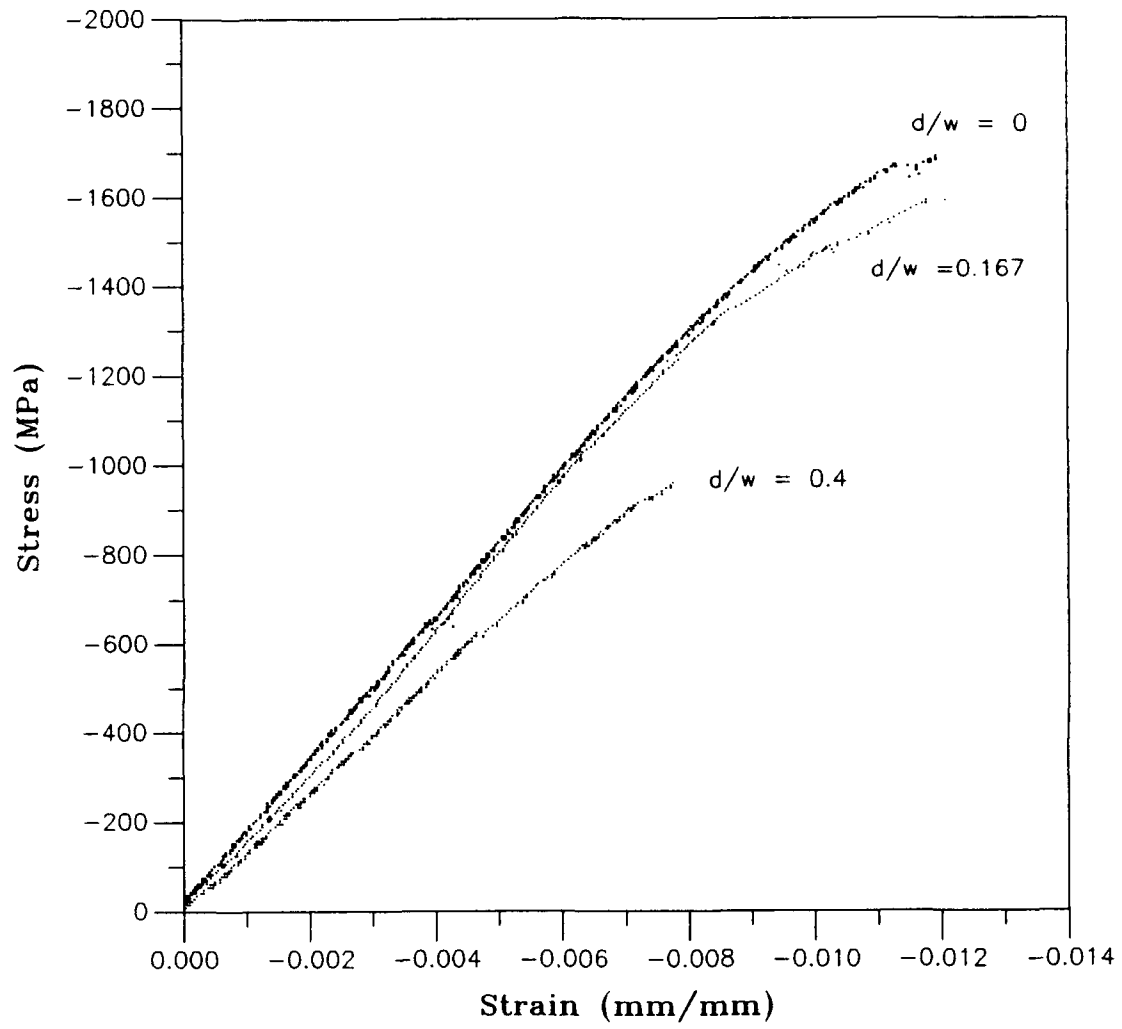


Figure 18. Room Temperature Compression, Sigma/Beta 21S

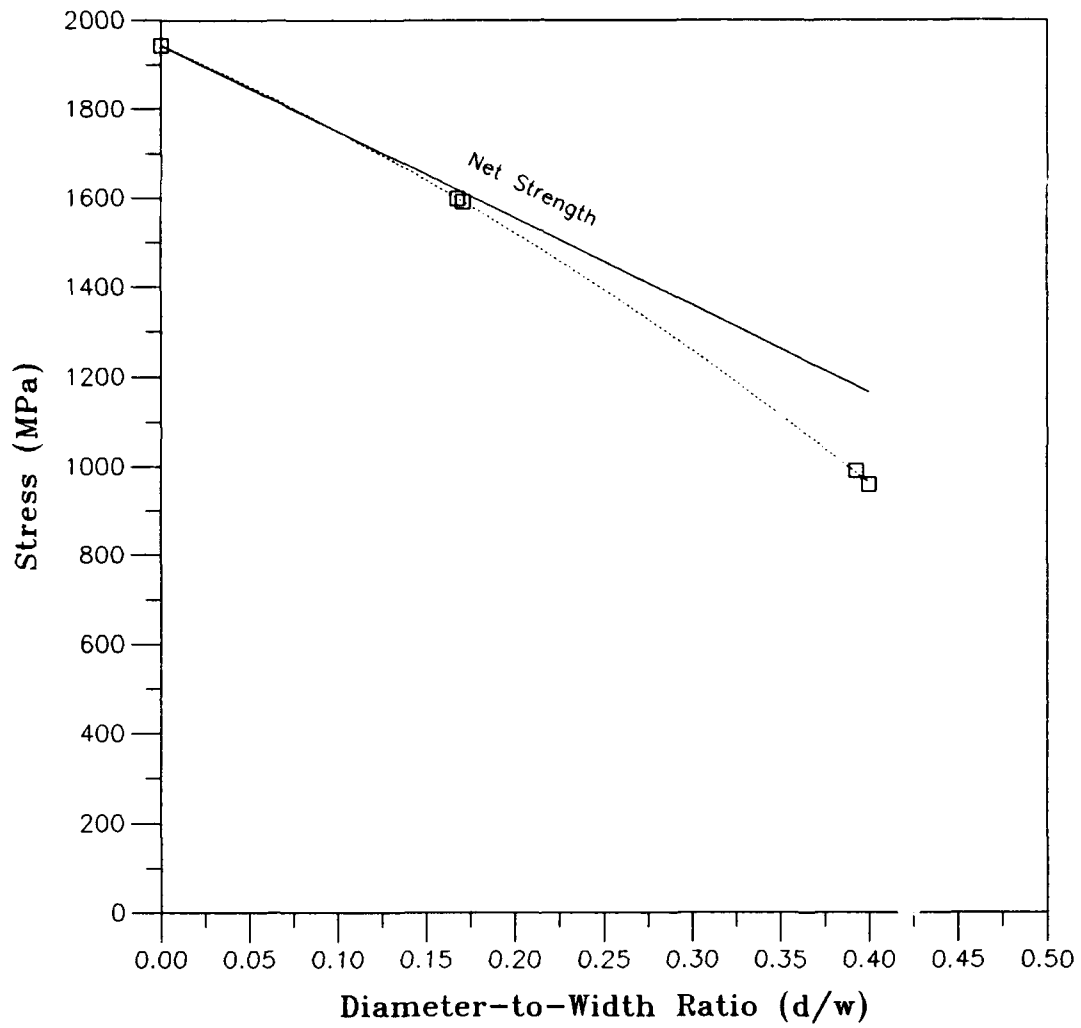


Figure 19. Room Temperature Compression Strength, Based on Remote Area, Sigma/Beta 21S

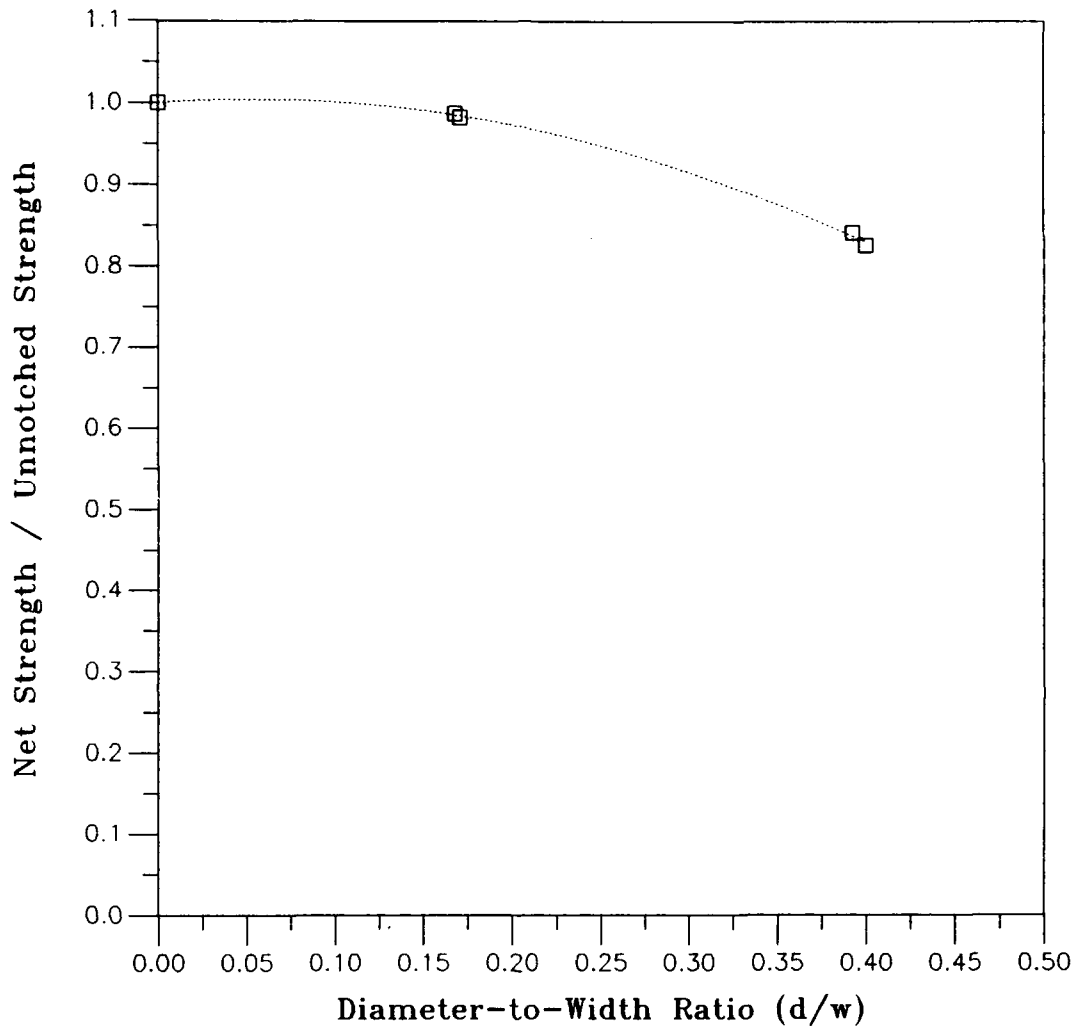


Figure 20. Normalized Strength, Room Temperature Compression, Sigma/Beta 21S

with increased diameter-to-width ratio.

SCS-6/Beta 21S, Room Temperature. The macromechanical behavior of SCS-6/Beta 21S at room temperature was observed through the a series of compression tests. The summary of these test results are provided in Table 3.

Table 3. SCS-6/Beta 21S, Room Temperature Results

Material	Test Temp. (°C)	d/w	Area (mm ²)	Ultimate Load (kN)	Ultimate Strength (MPa)	Net Strength σ_{net} (MPa)	Norm Strength σ_{net}/σ_o	Elastic Modulus (GPa)
SCS-6/B 21S	23.3	0	20.69	43.02	2079	2079	1	139
SCS-6/B 21S	22.8	0.18	21.31	32.10	1506	1826	0.88	125
SCS-6/B 21S	25.0	0.17	22.42	33.55	1497	1796	0.86	
SCS-6/B 21S	21.1	0.41	20.78	21.77	1048	1776	0.85	96
SCS-6/B 21S	22.8	0.41	21.80	21.72	997	1695	0.82	

SCS-6/Beta 21S exhibited an ultimate compressive strength at room temperature more than twice its tensile strength. The ultimate compressive strength was 2079 MPa, while Rattray reported an average tensile strength of 842 MPa (Rattray, 1992: 49-50). The elastic modulus in compression, 139 GPa, was similar to the elastic modulus in tension, 145 GPa (Rattray, 1992: 50).

Stress-strain curves for unnotched and notched SCS-6/Beta 21S specimens were plotted on one graph to show the variations due to the circular hole (Fig. 21). The reduction in elastic modulus was attributed to the use of the extensometer over the gage length encompassing the hole. The curves were initially linear, indicating elastic deformation. In the last 50-60% of the loading the curves were non-linear, indicating plasticity and damage. The strength

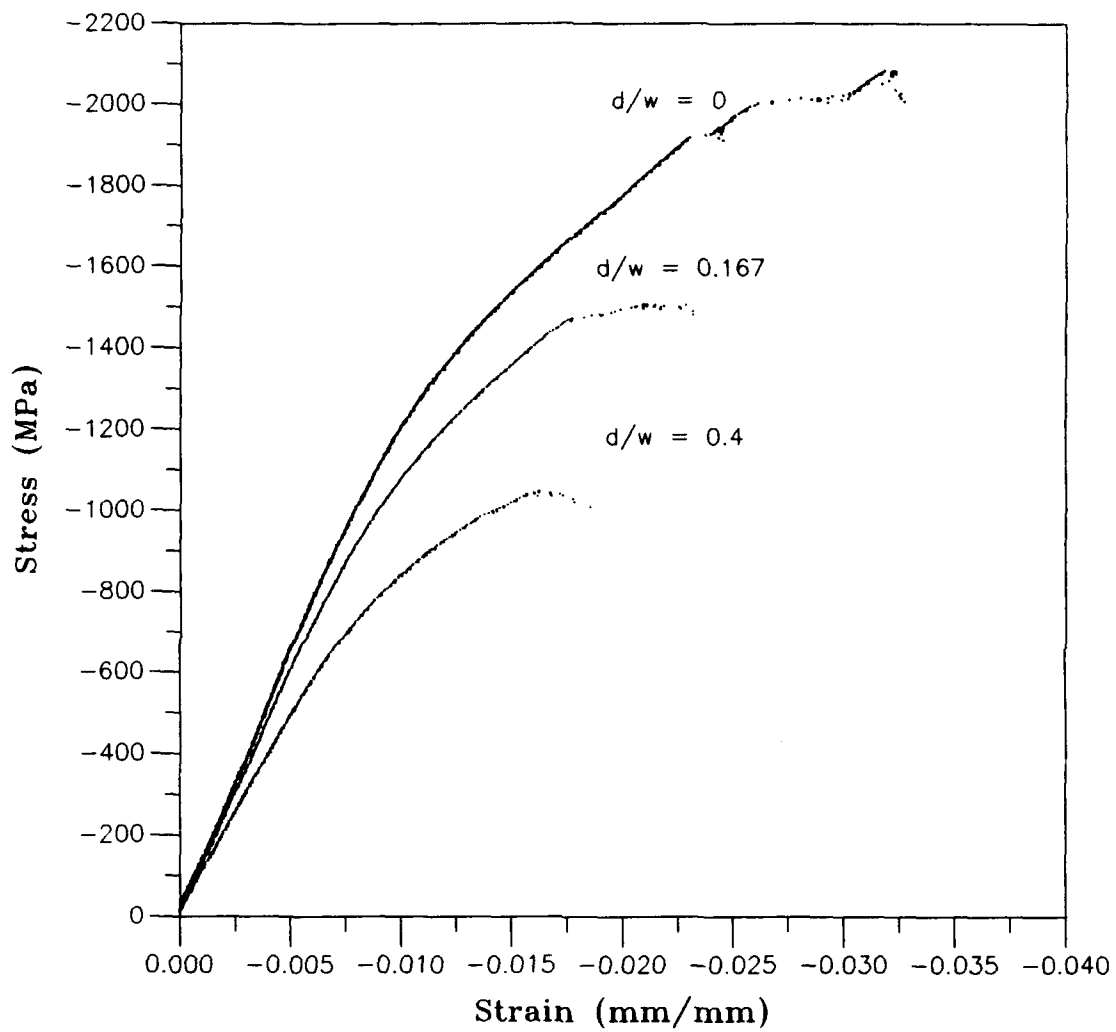


Figure 21. Room Temperature Compression, SCS-6/Beta 21S

reduction due to the hole can be clearly seen in the graph.

Notch sensitivity was evaluated through the use of a theoretical net strength line. Points on the line were calculated using Equation (4). The net strength line was the basis to which experimental values were compared to assess notch sensitivity.

Using the net strength line, SCS-6/Beta 21S was assessed to exhibit mild notch sensitivity, slightly increasing with hole size (Fig. 22). The curve showed that small and large diameter holes reduced the strength 13% and 18% from the theoretical net strength, respectively.

The normalized strength of the laminate was calculated for each experimental ultimate compressive strength, using Equation (6). The normalized strengths were displayed in a graph as a function of diameter-to-width ratio (Fig. 23). The data points showed the same trend of notch sensitivity, slightly increasing with diameter-to-width ratio.

SCS-6/Beta 21S, Elevated Temperature. This macromechanical behavior of SCS-6/Beta 21S at 650° C was observed through a series of compression tests. The summary of these test results are provided in Table 4.

Table 4. SCS-6/Beta 21S, Elevated Temperature Results

Material	Test Temp. (°C)	d/w	Area (mm ²)	Ultimate Load (kN)	Ultimate Strength (MPa)	Net Strength σ_{net} (MPa)	Norm Strength σ_{net}/σ_o	Elastic Modulus (GPa)
SCS-6/B 21S	650	0	21.90	26.67	1218	1218	1	81
SCS-6/B 21S	650	0.17	21.41	20.51	958	1156	0.95	73
SCS-6/B 21S	650	0.17	22.16	21.21	958	1149	0.94	
SCS-6/B 21S	650	0.40	22.45	13.69	610	1018	0.84	60
SCS-6/B 21S	650	0.41	22.04	12.92	586	987	0.81	

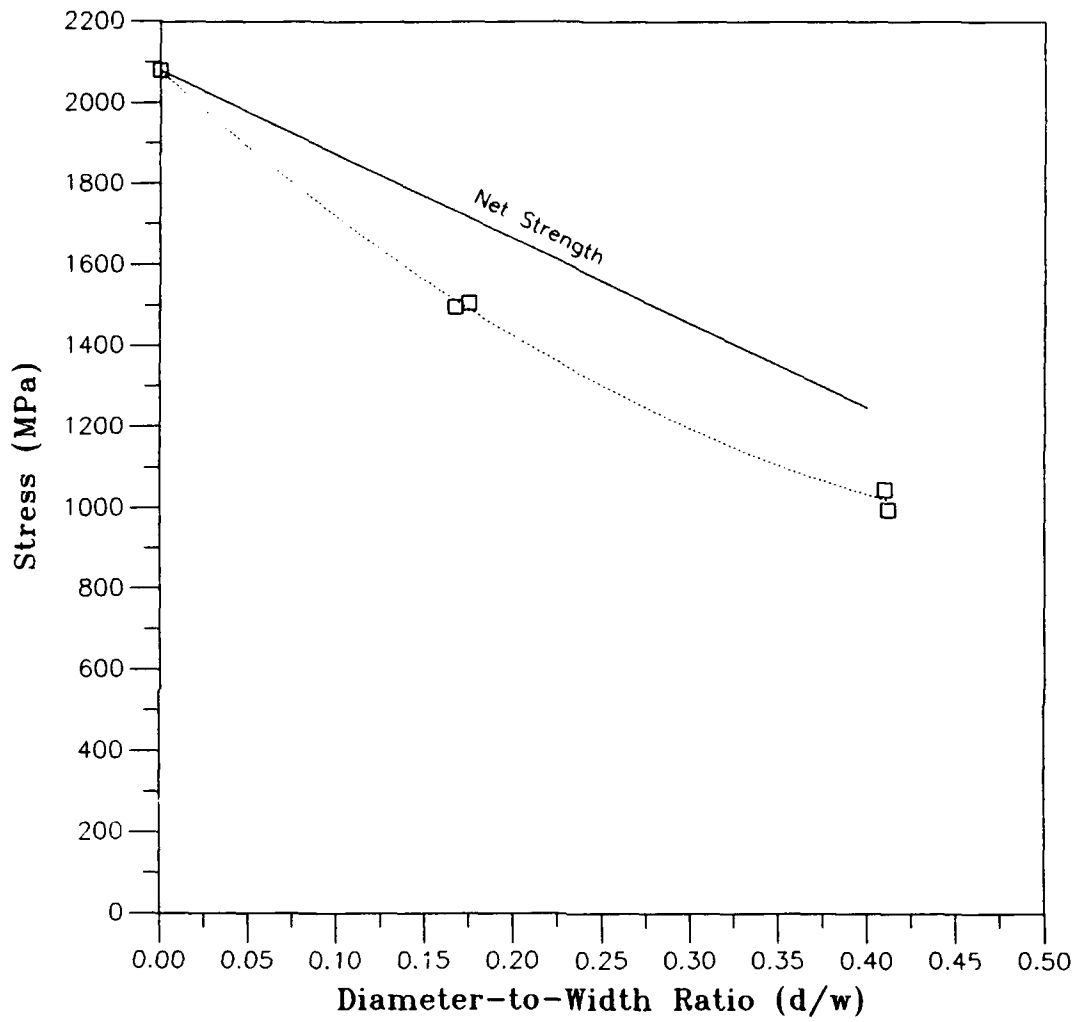


Figure 22. Room Temperature Compressive Strength, Based on Remote Area, SCS-6/Beta 21S

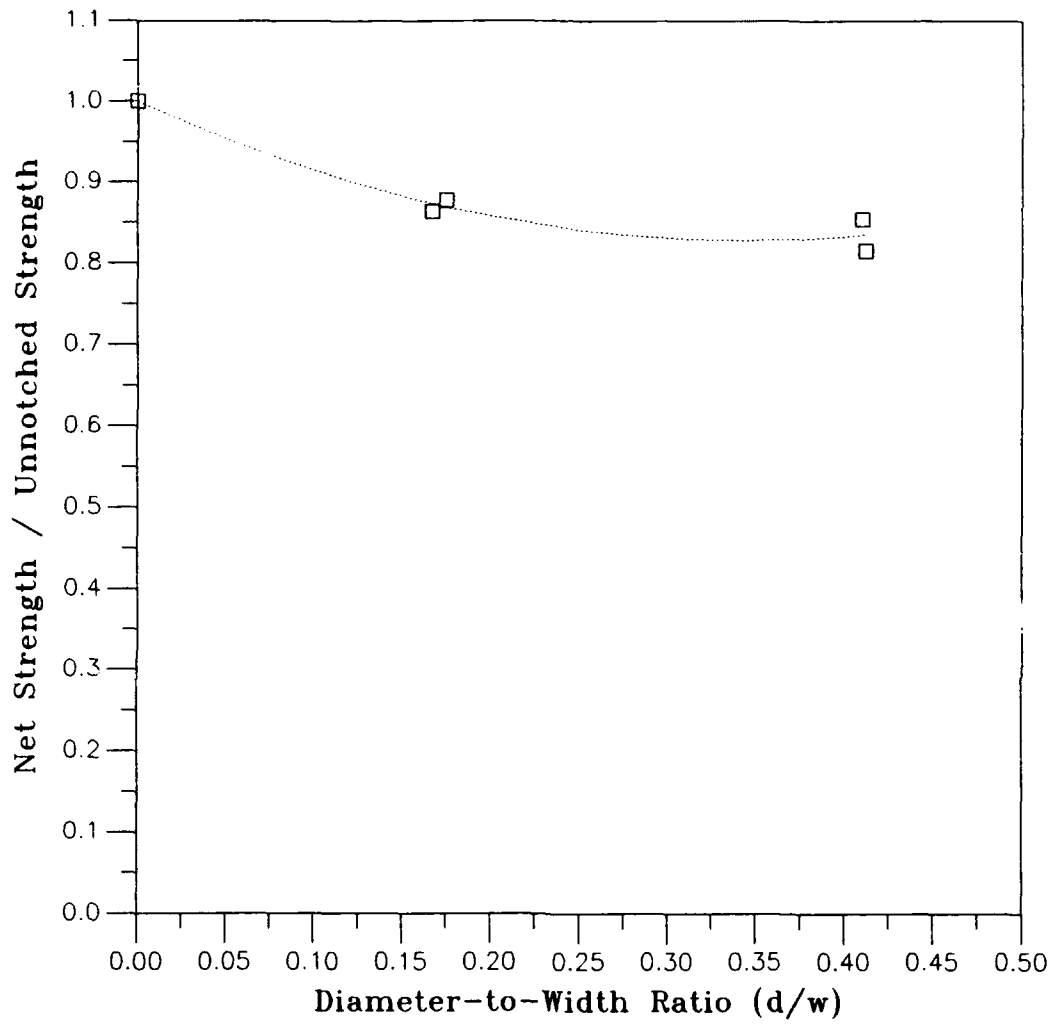


Figure 23. Normalized Strength, Room Temperature Compression, SCS-6/Beta 21S

SCS-6/Beta 21S exhibited an ultimate compressive strength at 650° C equal to approximately three times its tensile strength at 650° C. The ultimate compressive strength was 1218 MPa, while Rattray reported an average tensile strength of 397 MPa, at 650 °C (Rattray, 1992: 49-50). The elevated temperature elastic modulus in compression, 81 GPa, was similar to the elevated temperature elastic modulus in tension, 75 GPa (Rattray, 1992: 50).

Stress-strain curves for unnotched and notched SCS-6/Beta 21S specimens at 650°C were plotted on one graph to show the variations due to the circular hole (Fig. 24). The reduction in elastic modulus was attributed to the extensometer used over the gage length encompassing the hole. The curves were predominantly non-linear, indicating plastic deformation and damage. The linear portion of each curve encompassed the first 10 - 20% of the loading. The strength reduction, due to the hole, can be clearly seen in the graph.

Notch sensitivity was evaluated through the use of a theoretical net strength line. Points on the line were calculated using Equation (4). The net strength line was the basis to which experimental values were compared to assess notch sensitivity.

Using the net strength line, SCS-6/Beta 21S was assessed to exhibit notch sensitivity, increasing linearly with hole size (Fig. 25). The curve showed that small and large diameter holes reduced the strength 6% and 17% from the theoretical net strength, respectively.

The normalized strength of the laminate was calculated for each experimental ultimate compressive strength, using Equation (6). The normalized strengths were displayed in a graph as a function of diameter-to-width ratio (Fig. 26). The data points showed the same trend of notch sensitivity, linearly

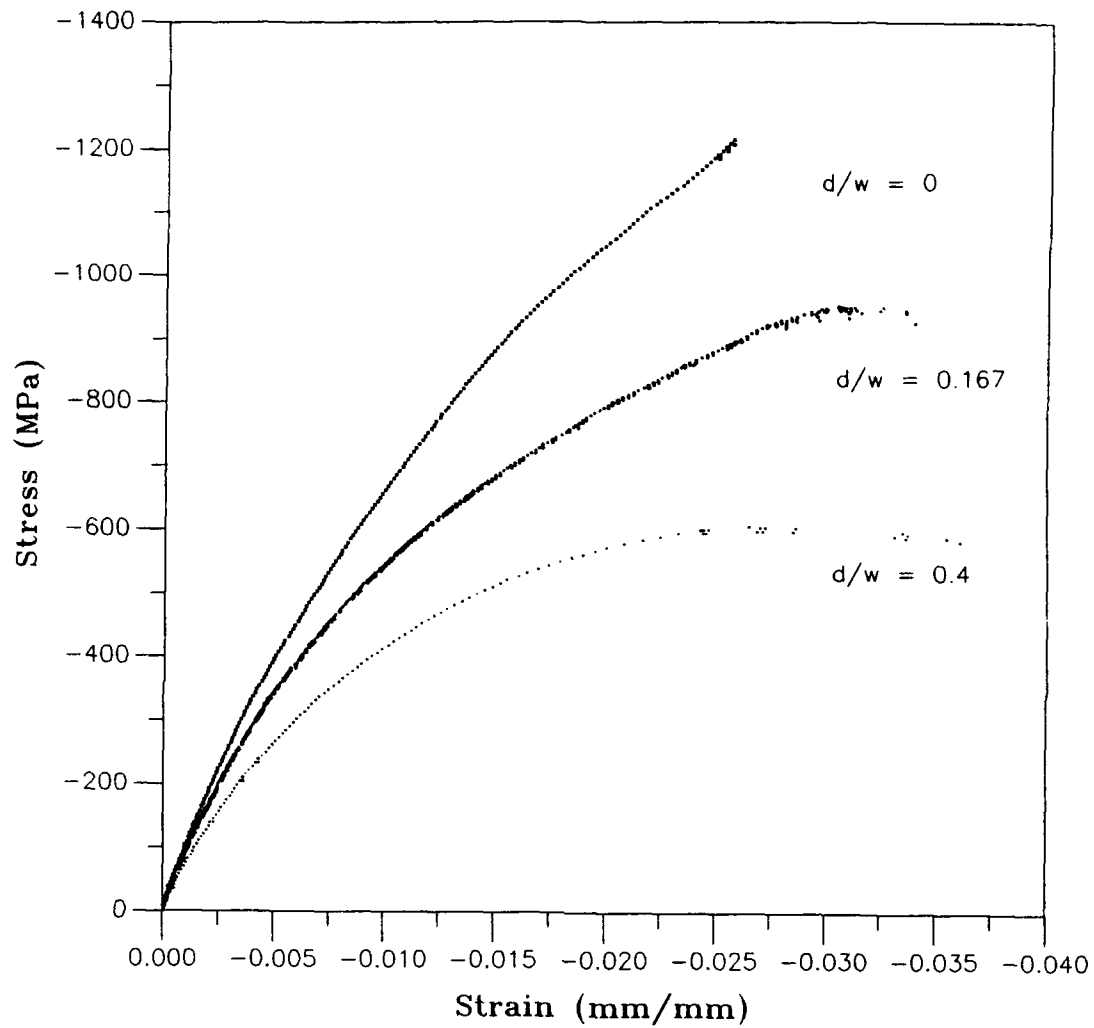


Figure 24. Elevated Temperature Compression, SCS-6/Beta 21S

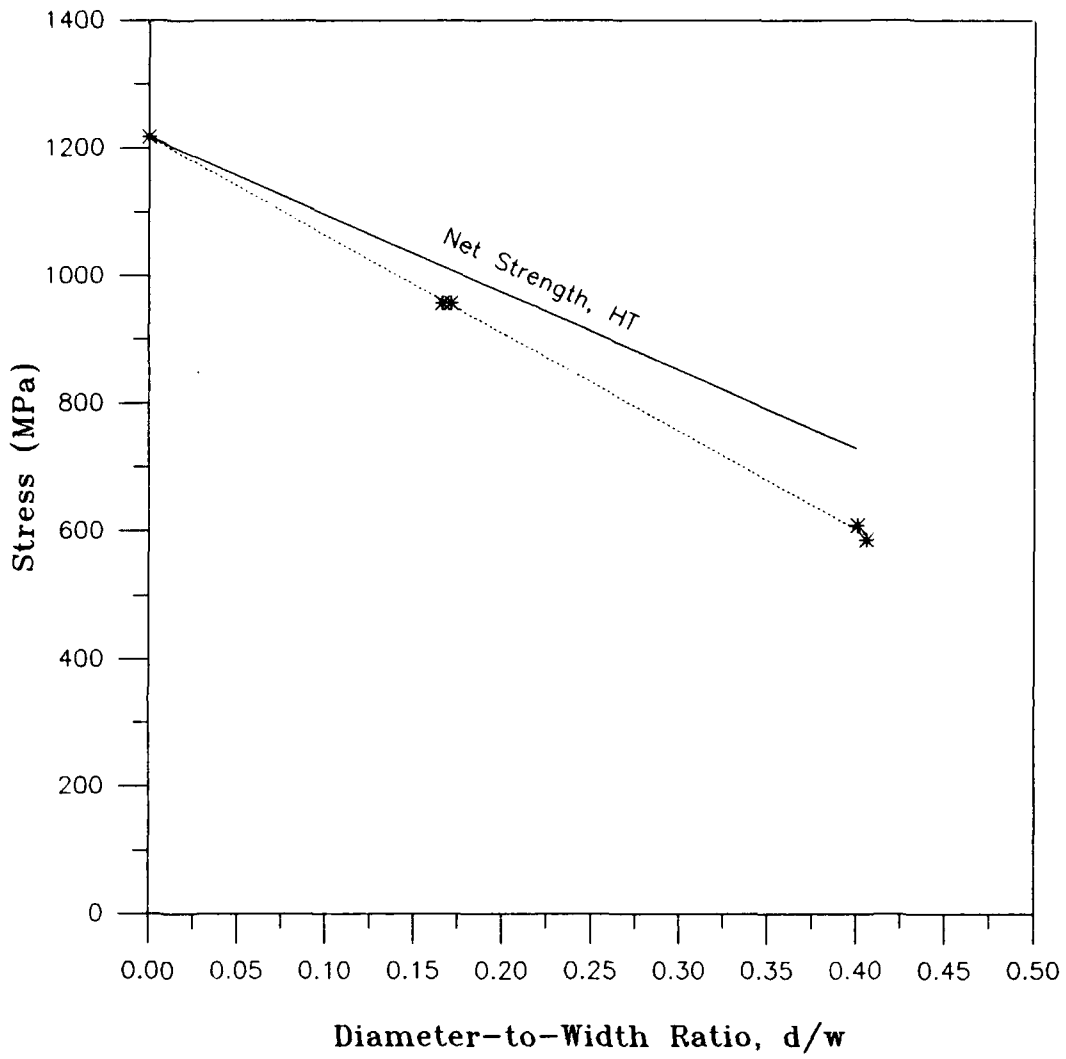


Figure 25. Elevated Temperature Compressive Strength, Based on Remote Area, SCS-6/Beta 21S

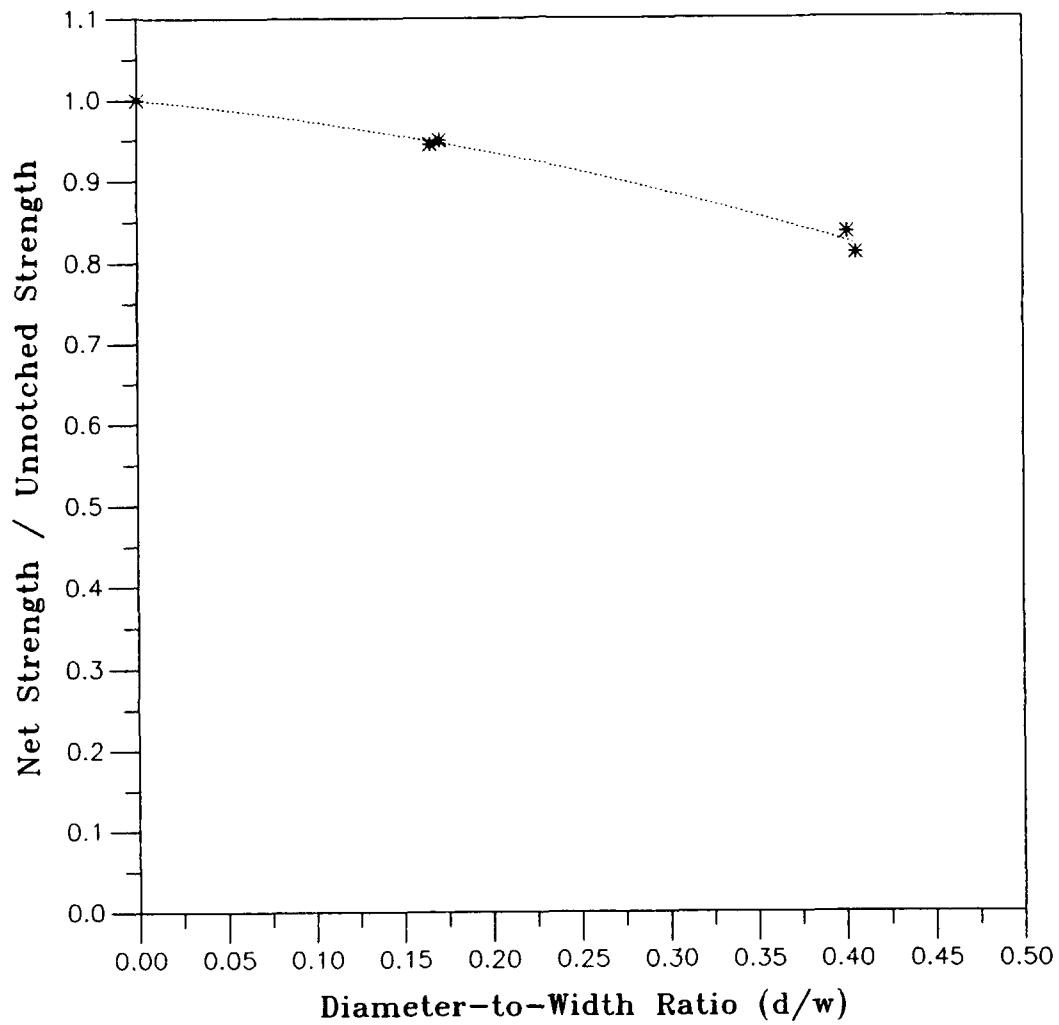


Figure 26. Normalized Strength, Elevated Temperature Compression, SCS-6/Beta 21S

increasing with diameter-to-width ratio.

Micromechanical Response

Micromechanical response is the internal behavior of the material. In MMCs, internal material failures may begin well before changes in the macromechanical response occur. In this section, the internal material failures will be investigated. Modes of internal material failure are fiber cracking, matrix yielding (plasticity), matrix cracking, separation (debonding) of the fibers from the matrix, and separation (delamination) of two adjacent lamina. In MMCs which have a relatively low fiber volume fraction, an additional internal material failure mode (in compression) is fiber microbuckling (Agarwal and Broutman, 1990: 87,92). The sequence of internal failures that constitute damage progression is identified in this section.

Sigma/Beta 21S, Room Temperature. The unnotched Sigma/Beta 21S specimen consistently failed near the outer edge of the gage length. Failure occurred at 90° to the loading axis (Figs. 27 and 28).

Scanning Electron Microscope (SEM) photographs taken of a specimen that had been loaded to 25% of the ultimate strength showed fiber debonding (Figs. 29 and 30). Before loading, The polished edge of the specimen showed fibers nearly flush with the matrix surface. After loading to 25% of the ultimate strength, the edge of the specimen showed protruding fibers as evidence of debonding between the fiber and matrix.

The tendency of the fibers to protrude from the matrix occurred in all specimens of both materials. This occurrence could not be predicted from the micromechanical response in compression prior to this experimentation. However, debonding allowed a relaxation of the fibers as they were released

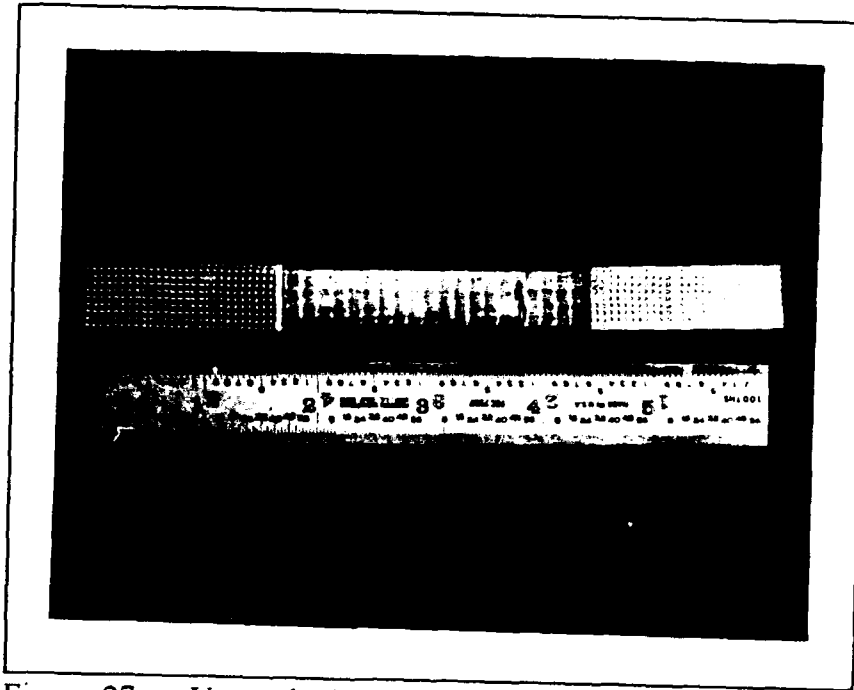


Figure 27. Unnotched Sigma/Beta 21S Compression Failure

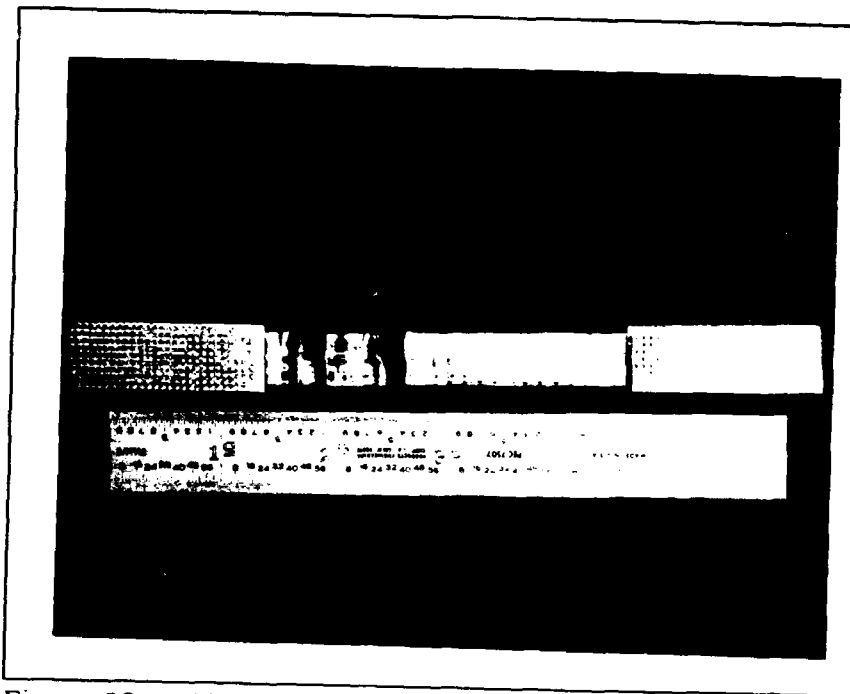


Figure 28. Unnotched Sigma/Beta 21S Compression Failure

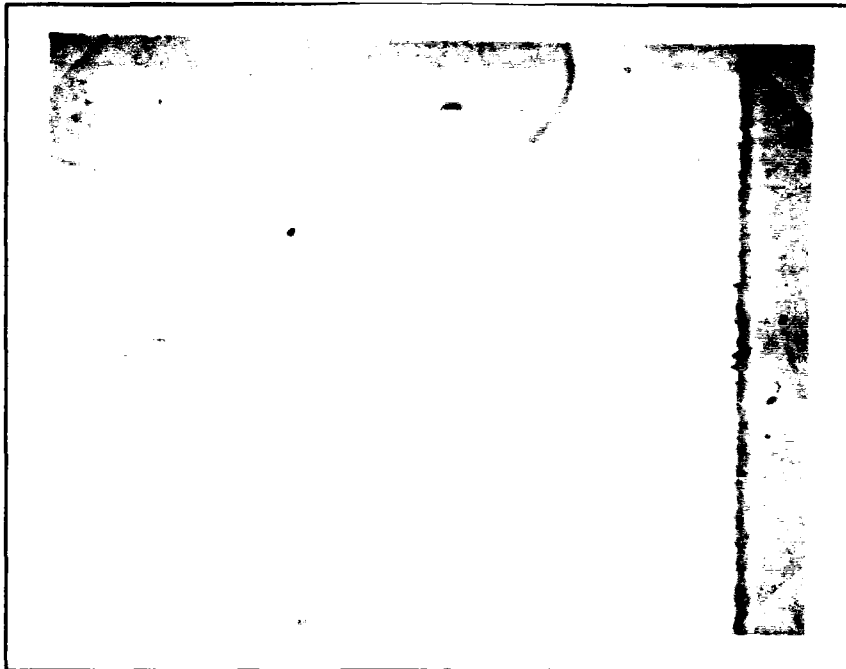


Figure 29. Sigma/Beta 21S, Polished Edge of Specimen, before Testing, 850X

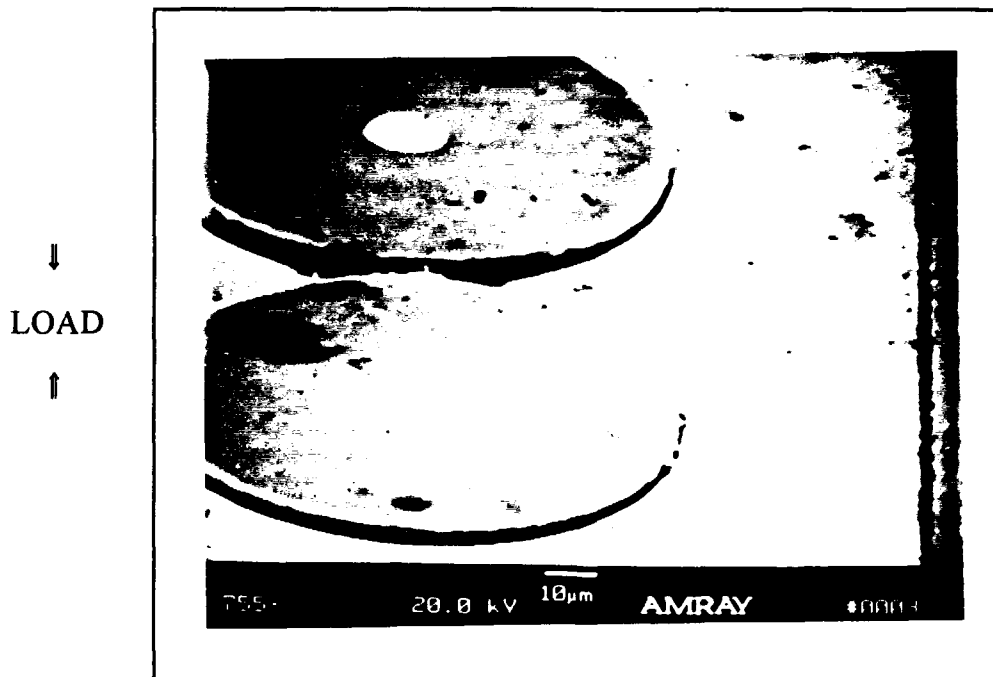


Figure 30. Sigma/Beta 21S, Polished Edge of a Specimen Tested to 25% of Ultimate Strength, 750X

from residual compressive stresses. The amount of debonding determined the length of fiber protrusion. (Pickard and others, 1993:1-2).

Matrix cracking was observed using the SEM on specimen edges which had been loaded to 90% of the ultimate stress. Longitudinal cracks in the matrix along the 0° fibers and between the 90° fibers were found widely over the entire gage length (Figs. 31-33).

No fiber damage was observed prior to specimen failure. The fracture surface showed matrix cracking between 0° fibers and along 90° fibers along the foil interface (Figs. 34 and 35). Matrix cracks had grown completely around the fibers at the fracture surface, resulting in massive debonding.

Matrix plasticity appeared as dimples on the fracture surface of the failed Sigma/Beta 21S specimens (Fig. 36). No plasticity in the matrix was evident at any point during the loading. The speculative conclusion was made that fiber microbuckling occurred, preceded by massive debonding, causing failure in an extensional mode. Extensional mode failure occurs when the lateral deformation of two adjacent fibers is out of phase. When lateral deformation of fibers is in phase, the failure occurs in a shear mode (Agarwal and Broutman, 1990: 92,93). The fracture surfaces of the unnotched Sigma/Beta 21S specimens support the conclusion that failure occurred in an extensional mode. The fracture surface showed the matrix separated from the fibers in all 0° plies. Stresses induced by 0° fiber microbuckling may have caused this separation.

The notched Sigma/Beta 21S specimens consistently failed at 90° to the loading axis (Figs. 37 and 38). Prior to the 90° (transverse) failure, the specimens with a hole of diameter-to-width ratio equal to 0.4 failed parallel to the loading axis (longitudinally). The longitudinal failure was observed at 90%

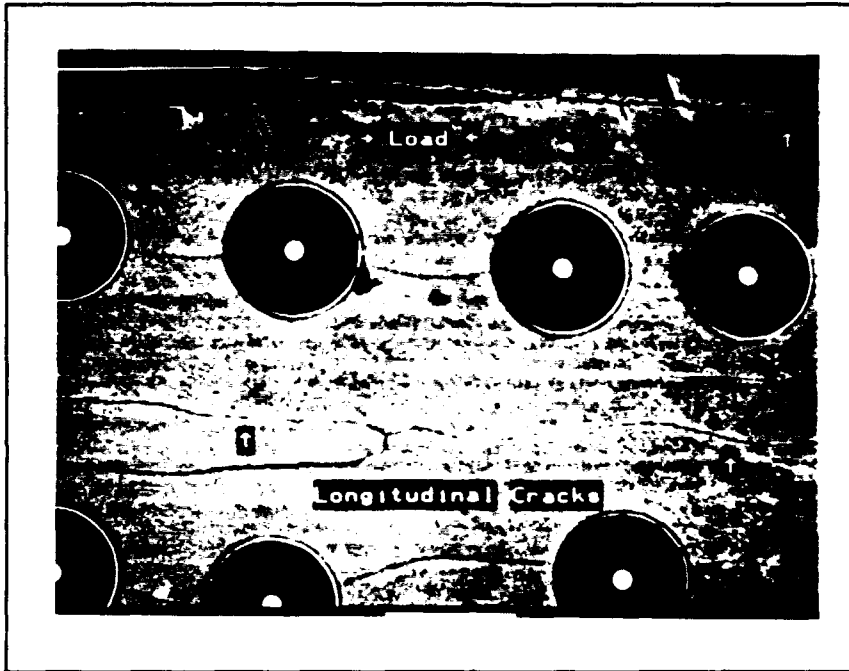


Figure 31. Sigma/Beta 21S, Longitudinal Matrix Cracks at 0° Fibers, 186X

→ LOAD ←

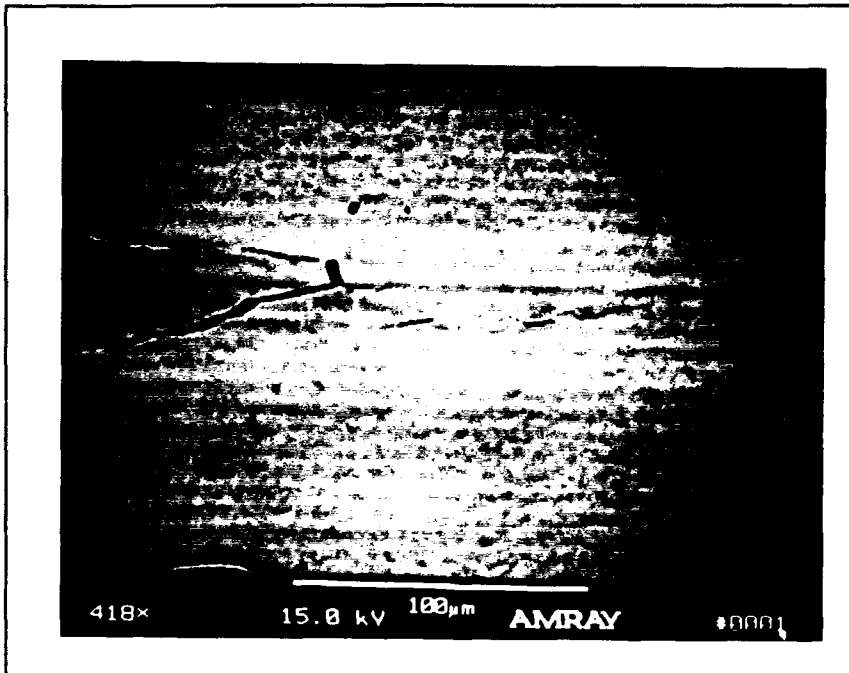


Figure 32. Sigma/Beta 21S, Longitudinal Matrix Cracks at 0° Fibers, 418X

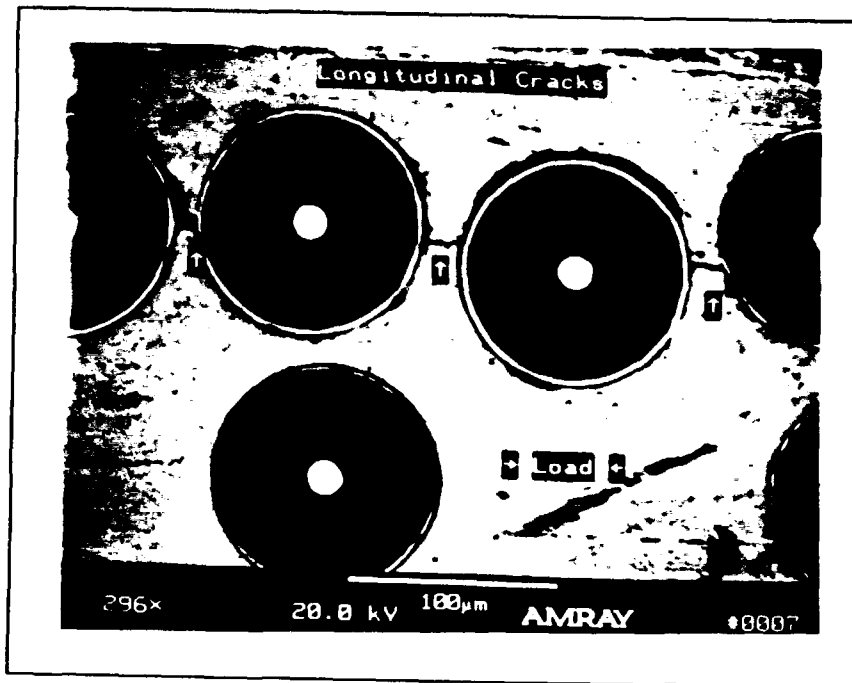


Figure 33. Sigma/Beta 21S, Longitudinal Matrix Cracks between 90° Fibers, 296X

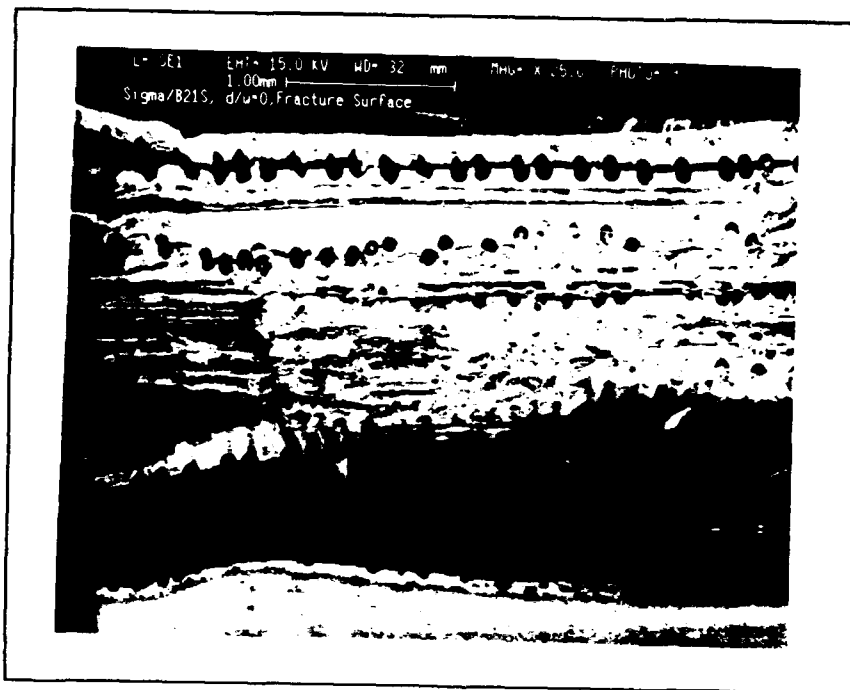


Figure 34. Unnotched Sigma/Beta 21S, Fracture Surface, 25X

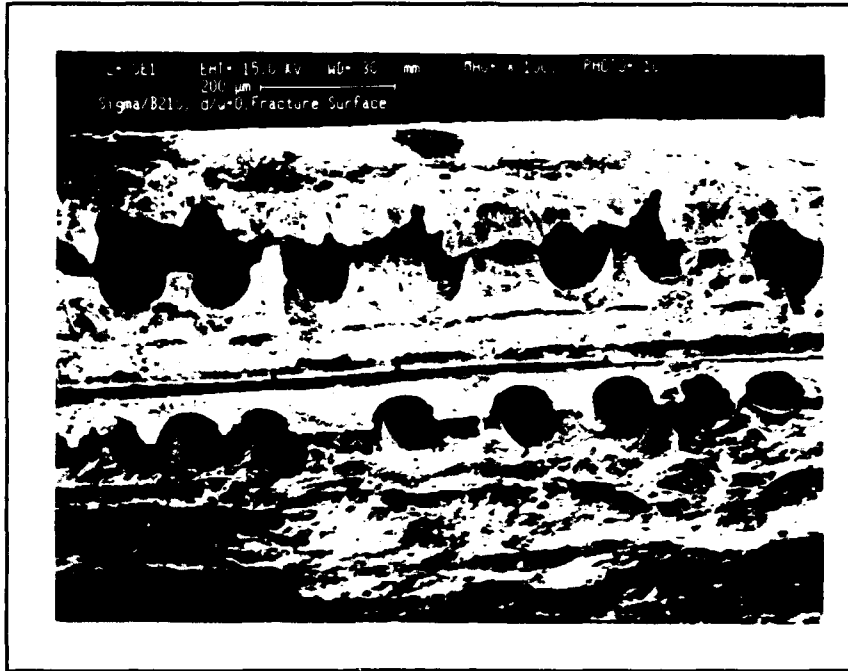


Figure 35. Unnotched Sigma/Beta 21S, Fracture Surface, 100X

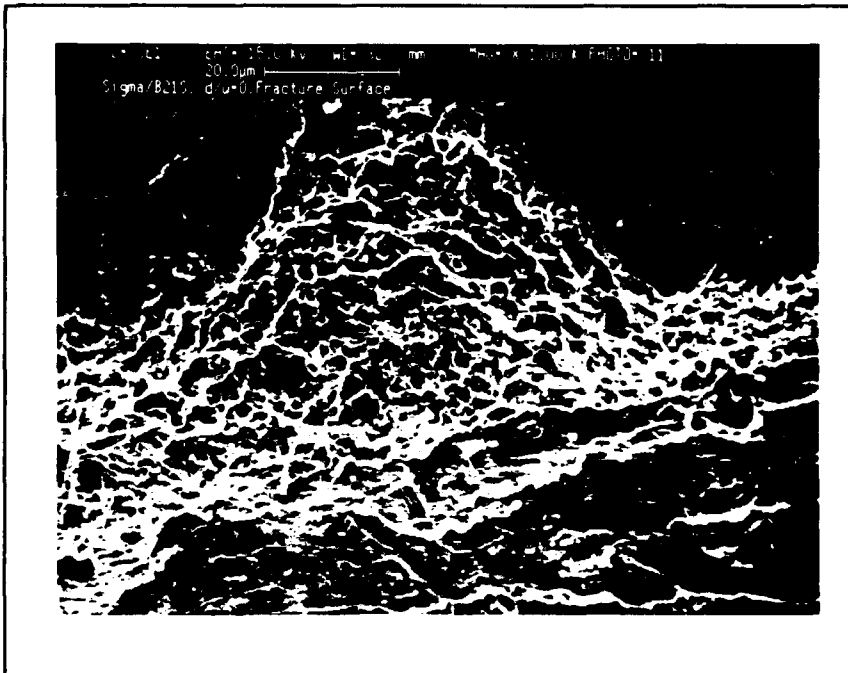


Figure 36. Unnotched Sigma/Beta 21S, Fracture Surface, Showing Matrix Plasticity, 1000X

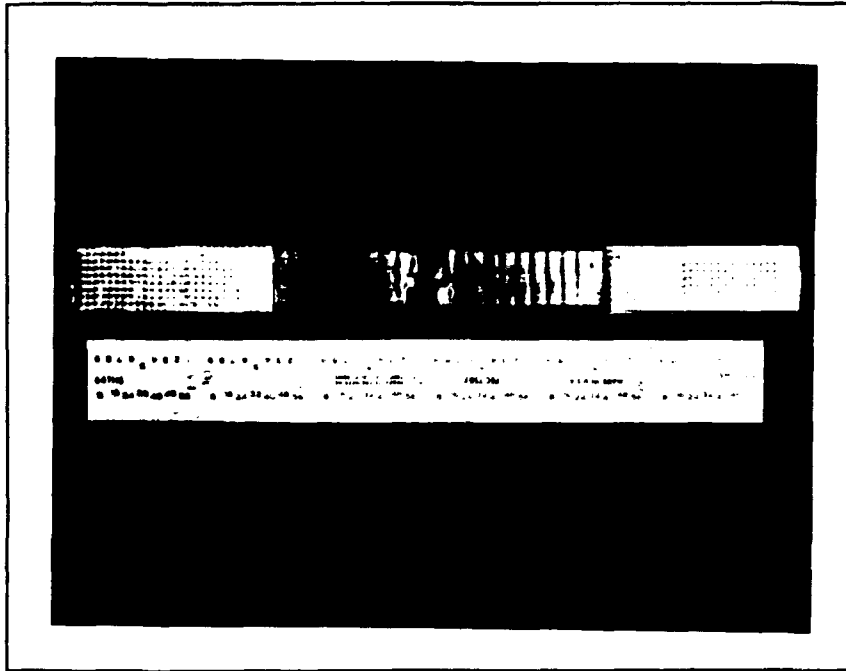


Figure 37. Notched Sigma/Beta 21S, Room Temperature Compression Failure, $d/w=0.167$

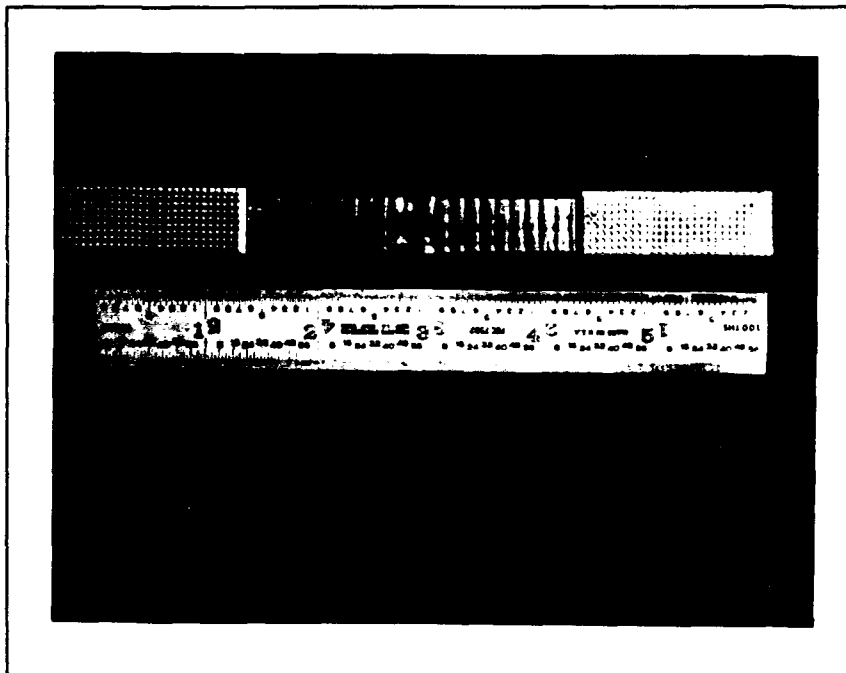


Figure 38. Notched Sigma/Beta 21S, Room Temperature Compression Failure, $d/w=0.4$

of the ultimate strength.

SEM investigation showed that the failure progression of notched specimens paralleled that of unnotched specimens. However, the damage was initially observed in the edge region adjacent to the hole.

The transverse fracture surface was similar to the unnotched specimen fracture surface, showing matrix plasticity and massive debonding resulting from matrix cracking (Figs. 39 and 40). SEM examination of the longitudinal fracture surface revealed 0° fiber debonding and matrix plasticity (Fig. 41 and 42).

Notched specimens which had been loaded to 90% of the ultimate strength were etched until the matrix was removed. This facilitated examination of the fibers near the hole. At 90° to the loading, no fiber damage (other than that caused by machining of the hole) was observed at the hole (Figs. 43 and 44).

The region above and below the hole was examined on the etched surface. The longitudinal cracks were found emanating from the top and bottom of the $d/w = 0.4$ hole. Broken 90° fibers were observed through the longitudinal matrix cracks between the 0° fibers reaction zones (Figs. 45 - 47).

The speculative conclusion is made that fiber microbuckling occurred, preceded by massive debonding, causing failure in an extensional mode. The transverse and longitudinal fracture surfaces of the notched Sigma/Beta 21S specimens support the conclusion that failure occurred in an extensional mode. The transverse fracture surface showed the matrix separated from the fibers in all 0° plies. Stress induced by fiber microbuckling may have caused this separation. The longitudinal fracture surface showed bent 0° fibers, possibly an

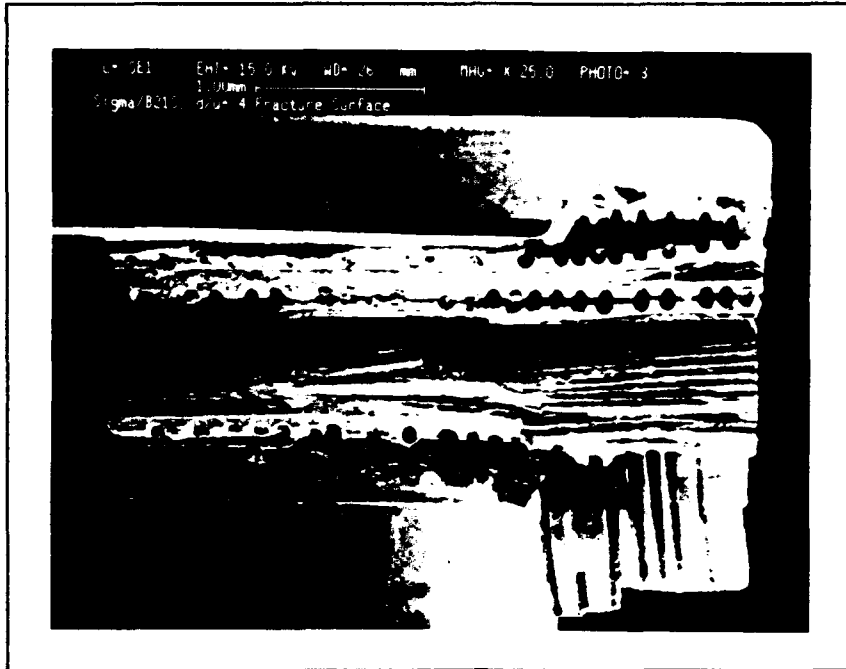


Figure 39. Notched Sigma/Beta 21S, Fracture Surface, 25X

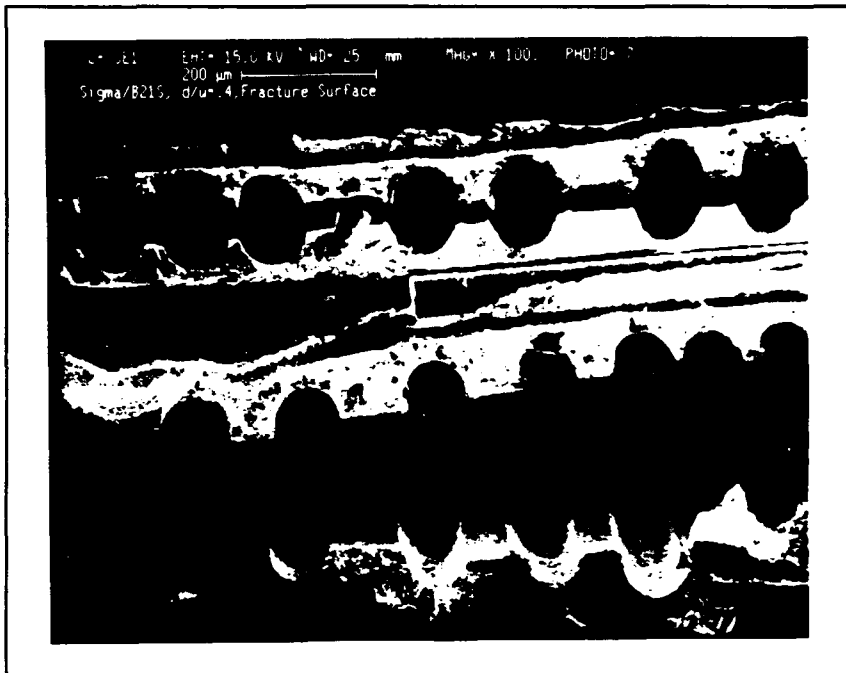


Figure 40. Notched Sigma/Beta 21S, Fracture Surface, 100X

↓
LOAD
↑



Figure 41. Notched Sigma/Beta 21S, Longitudinal Fracture Surface, 150X

↓
LOAD
↑

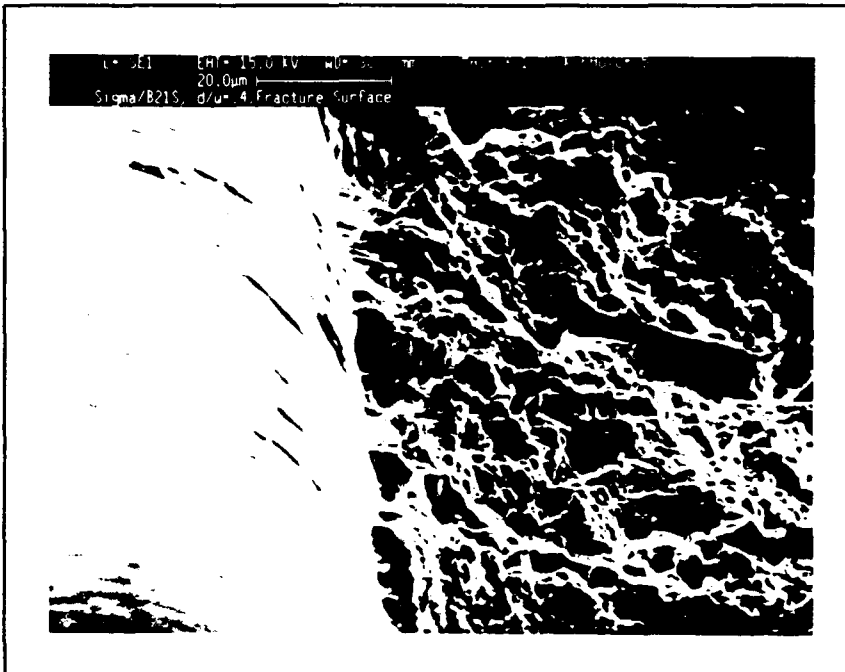


Figure 42. Notched Sigma/Beta 21S, Longitudinal Fracture Surface, 1000X

→ LOAD ←

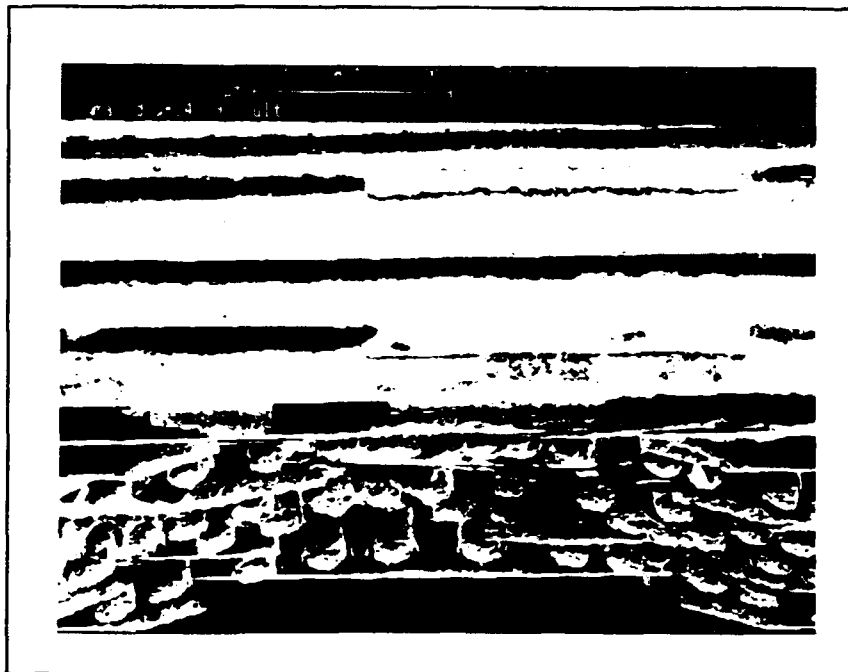


Figure 43. Notched Sigma/Beta 21S, Etched Face, Hole Boundary at 90°, 50X

→ LOAD ←



Figure 44. Notched Sigma/Beta 21S, Etched Face, Lateral Hole Boundary, 150X

↓
LOAD
↑

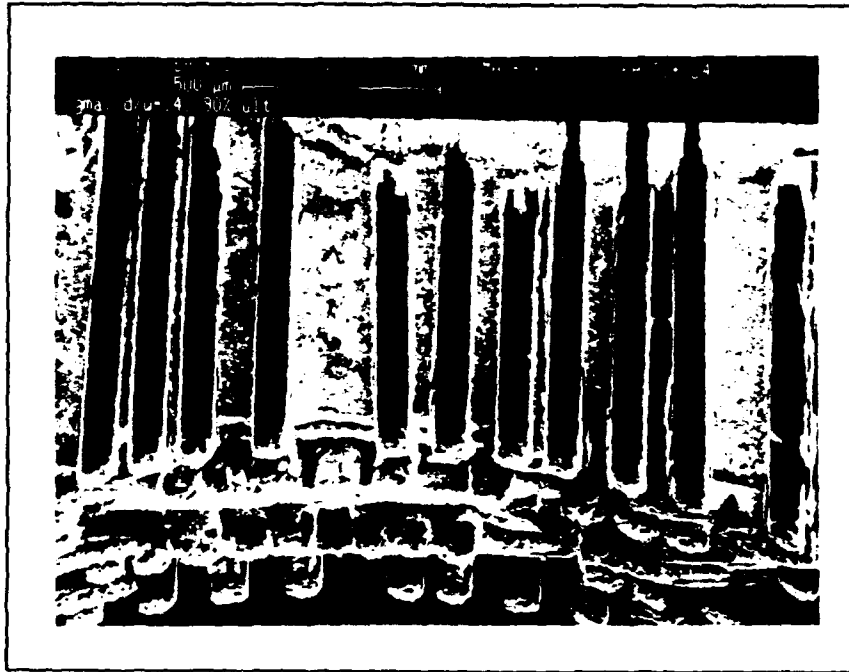


Figure 45. Notched Sigma/Beta 21S, Etched Face, Top of Hole, Showing Matrix Cracking, 50X

⇒ LOAD ⇐

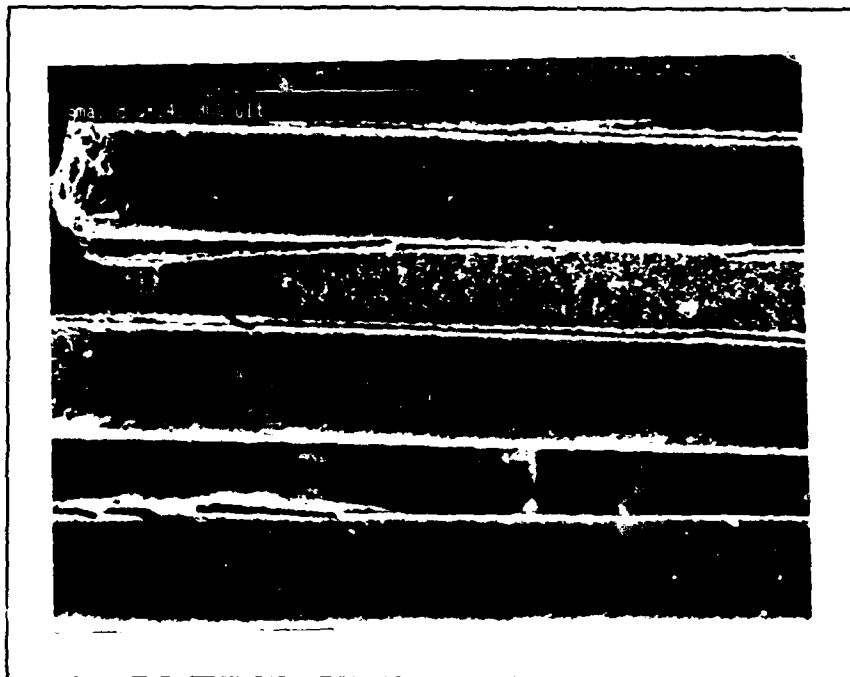


Figure 46. Notched Sigma/Beta 21S, Etched Face, Top of Hole, Showing Matrix Cracking, 150X

⇒ LOAD ⇐

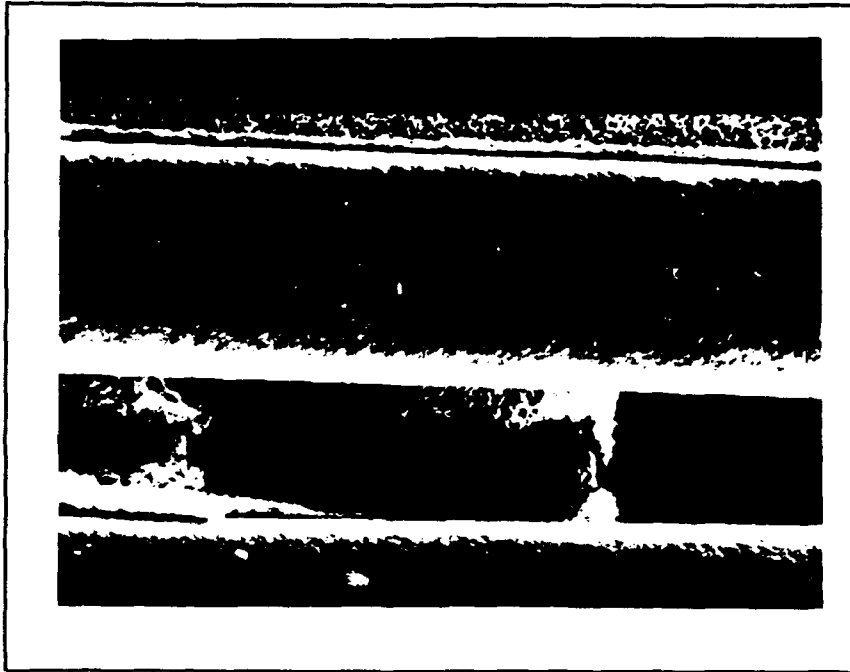


Figure 47. Notched Sigma/Beta 21S, Etched Face, Showing 90° Fiber Cracking, 300X

indication of fiber microbuckling. The extensional stresses in the matrix (at the top and bottom of the hole) due to fiber microbuckling may have caused in longitudinal matrix cracking.

SCS-6/Beta 21S, Room Temperature. At room temperature, the unnotched SCS-6/Beta 21S specimens consistently failed at 90° to the loading axis near the outer edge of the gage length (Fig. 48). Matrix plasticity was visually observed in the failed specimens by the expanded specimen width near the fracture surface.

SEM photographs taken of a specimen that had been loaded to 20% of the ultimate strength showed fiber debonding in the 45° and 90° plies (Figs. 49 and 50). Before loading, the polished edge of the specimen showed fibers nearly flush with the matrix surface. After loading to 20% of ultimate strength, the edge of the specimen showed protruding fibers as evidence of debonding between the fiber and matrix.

Matrix plasticity initiated at the reaction zone (fiber/matrix junction), became evident in the 45° plies at 40% of the ultimate stress. Matrix plasticity appeared as V shapes in the matrix emanating from reaction zone cracks (Figs. 51 and 52). Radial cracks in the 90° fibers and matrix plasticity in those plies were observed at 50% of the ultimate stress (Fig. 53). Matrix plasticity was observed on the polished edge of a failed, unnotched specimen (Fig. 54). Matrix plasticity appeared as parallel lines in the matrix, called slip bands, and as deformation surrounding the fibers (Figs. 55 and 56).

Matrix plasticity appeared as dimples on the fracture surface of the failed SCS-6/Beta 21S specimens (Fig. 57). The bulged cross section suggests the possibility that fiber microbuckling occurred, preceded by matrix yielding,

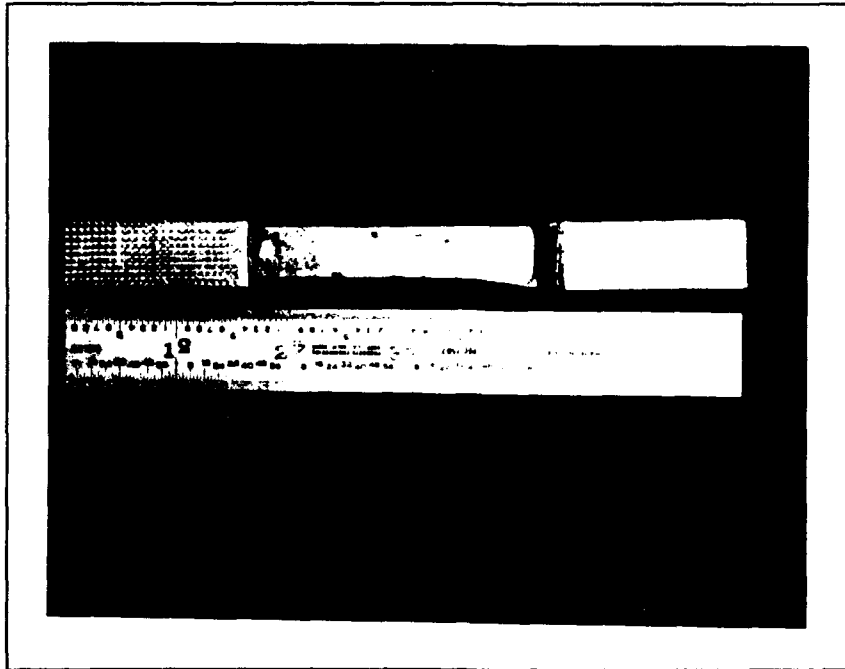


Figure 48. Unnotched SCS-6/Beta 21S, Room Temperature Compression Failure

↓
LOAD
↑

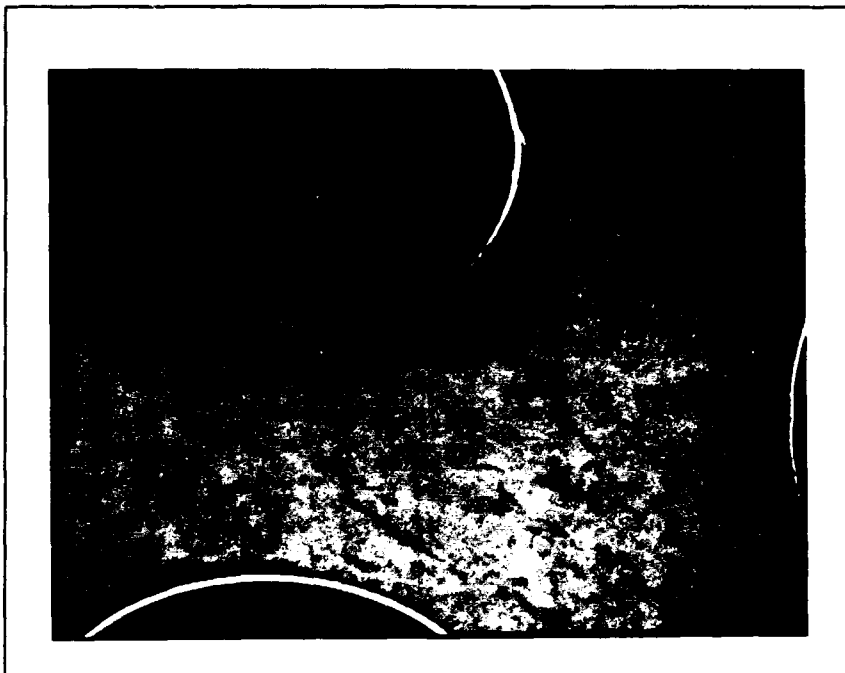


Figure 49. SCS-6/Beta 21S, Polished Edge of an Untested Specimen, 45° and 90° Fibers, 400X

↓
LOAD
↑

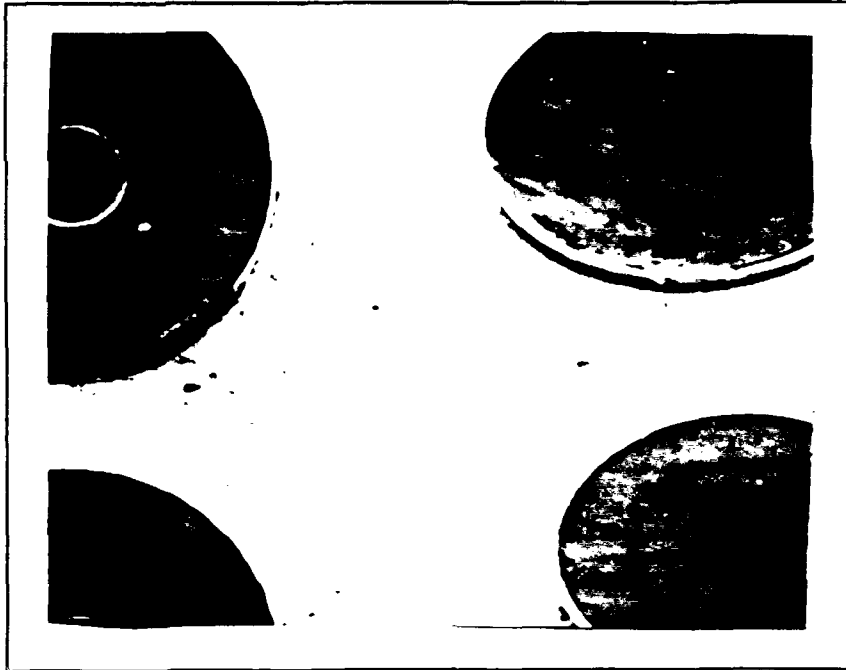


Figure 50. SCS-6/Beta 21S, 45° and 90° Fibers of a Specimen Tested to 20% of Ultimate Strength, 334X

⇒ LOAD ⇐

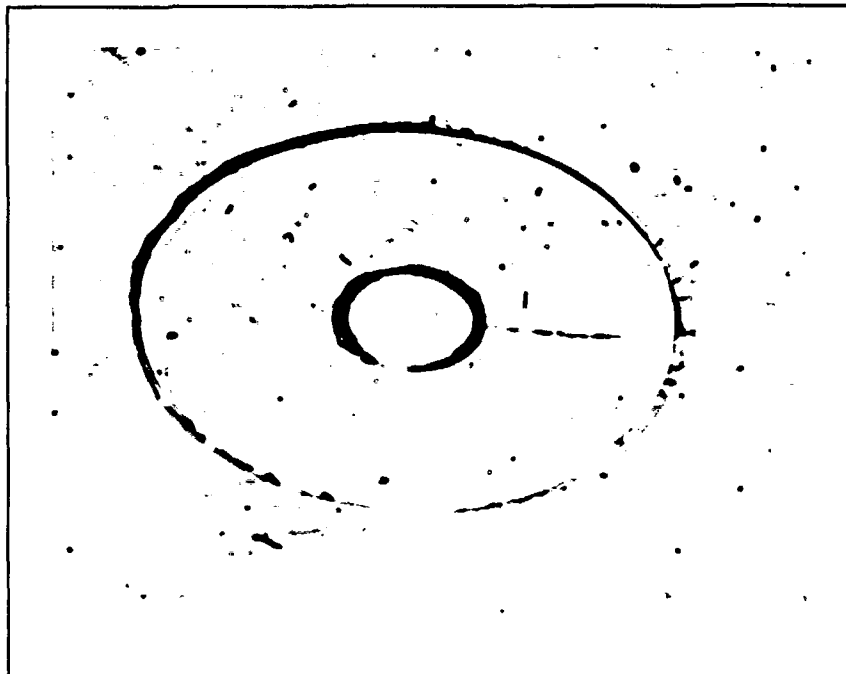


Figure 51. SCS-6/Beta 21S, 45° Fiber of a Specimen Tested to 40% of Ultimate Strength, 500X

→ LOAD ←

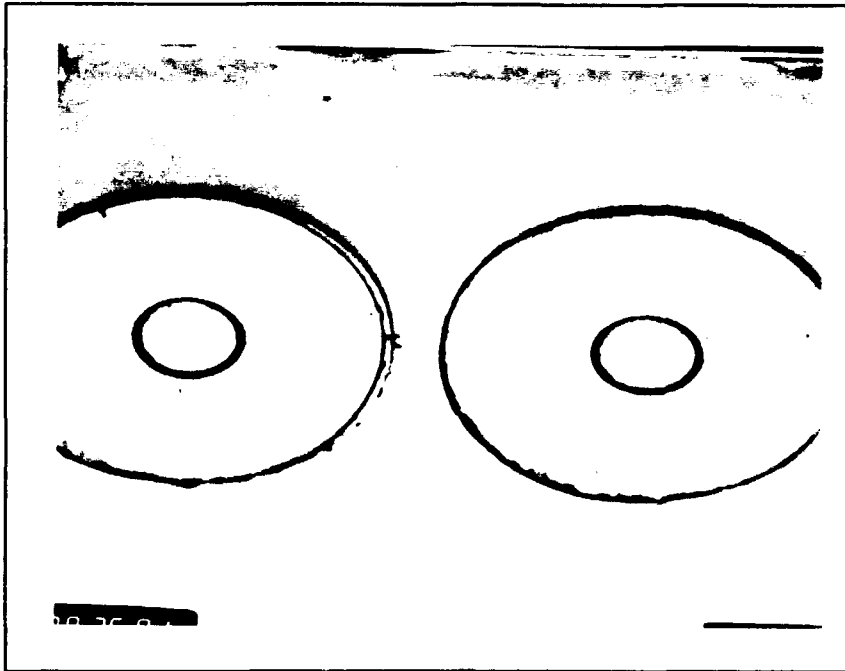


Figure 52. SCS-6/Beta 21S, 45° Fibers Tested to 40% of Ultimate Strength, Showing Matrix Plasticity, 300X

→ LOAD ←

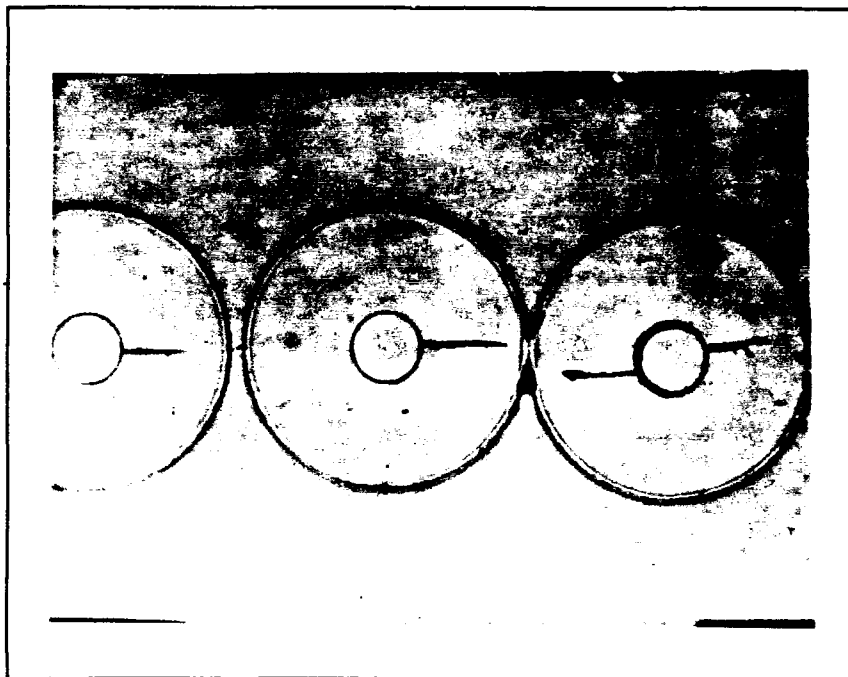


Figure 53. SCS-6/Beta 21S, Edge Replica of 90° Fibers, 50% of Ultimate Strength, Showing Radial Cracks, 300X

↓
LOAD
↑

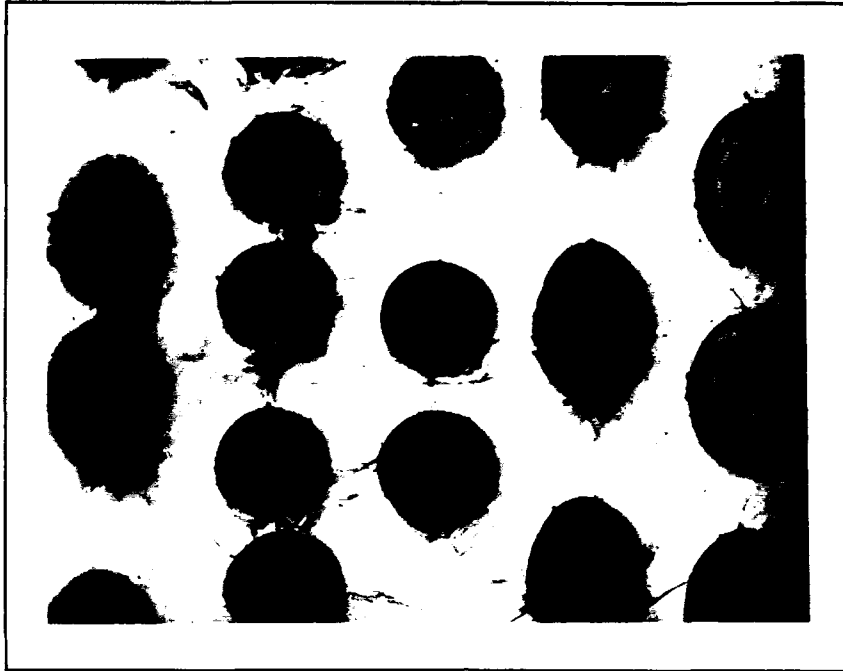


Figure 54. SCS-6/Beta 21S, Polished Edge of a Failed Room Temperature Specimen, 100X

↓
LOAD
↑



Figure 55. SCS-6/Beta 21S, Polished Edge of a Failed, Room Temperature Specimen, Showing Slip Bands, 1000X

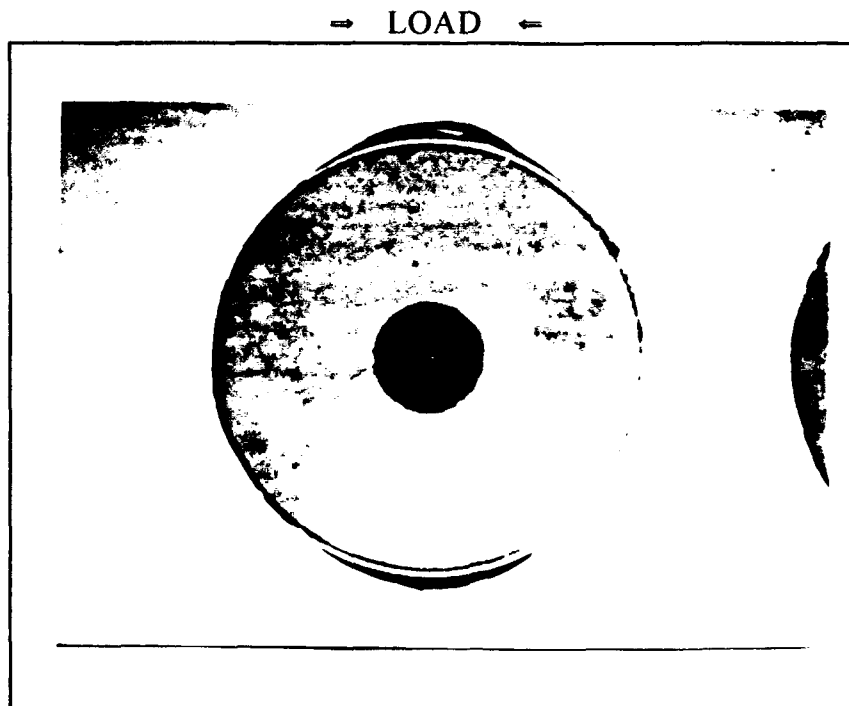


Figure 56. SCS-6/Beta 21S, Room Temperature Specimen, Showing Matrix Deformation, 350X

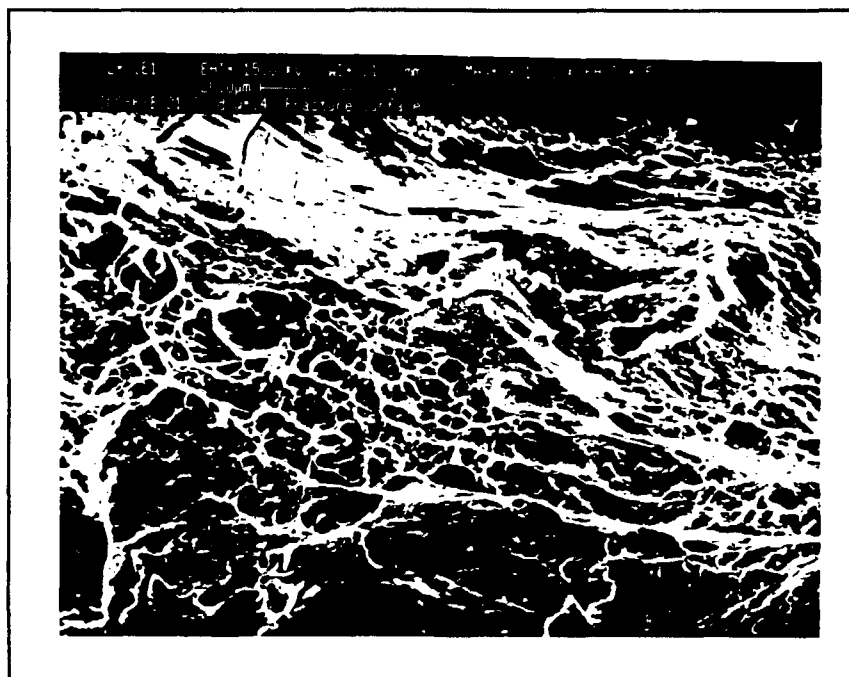


Figure 57. Unnotched SCS-6/Beta 21S, Fracture Surface, Showing Matrix Plasticity, 1000X

causing failure in an extensional mode (Figs. 58 and 59).

The notched SCS-6/Beta 21S specimens consistently failed at 45° to the loading axis, indicating failure in a shear mode (Figs. 60 and 61). Matrix plasticity was visually observed through deformation of the specimen in the region of the hole.

SEM investigation showed that the failure progression of notched specimens paralleled that of unnotched specimens. However, the damage was initially observed in the edge region adjacent to the hole. The fracture surface showed matrix cracking and matrix plasticity (Figs. 62 and 63). The notched failure of SCS-6/Beta 21S at room temperature was a result of fiber failure, possibly due to in phase fiber microbuckling, preceded by matrix shear failure.

SCS-6/Beta 21S, Elevated Temperature. At elevated temperature, the unnotched SCS-6/Beta 21S specimens consistently failed at 90° to the loading axis near the outer edge of the gage length (Fig. 64). The specimen edge revealed the orientation of the fracture surface at 45° to the loading axis, indicating failure in a shear mode.

Edge replicas of a specimen that had been loaded to 20% of the ultimate strength (at 650° C) showed fiber debonding in the 90° plies (Fig. 65). Fiber debonding appeared as smudges of acetate on the circumference of the fiber.

SEM examination of specimens, which had been loaded to 90% of ultimate strength, revealed extensive matrix cracking and plasticity on the specimen edges (Figs. 66 and 67). Matrix cracking was initiated at the reaction zone. Matrix plasticity appeared as deformation around the fiber. At very high magnification, diffused slip bands and reaction zone cracks were detected (Fig. 68).



Figure 58. Unnotched SCS-6/Beta 21S, Fracture Surface, Bulging Cross Section, 25X

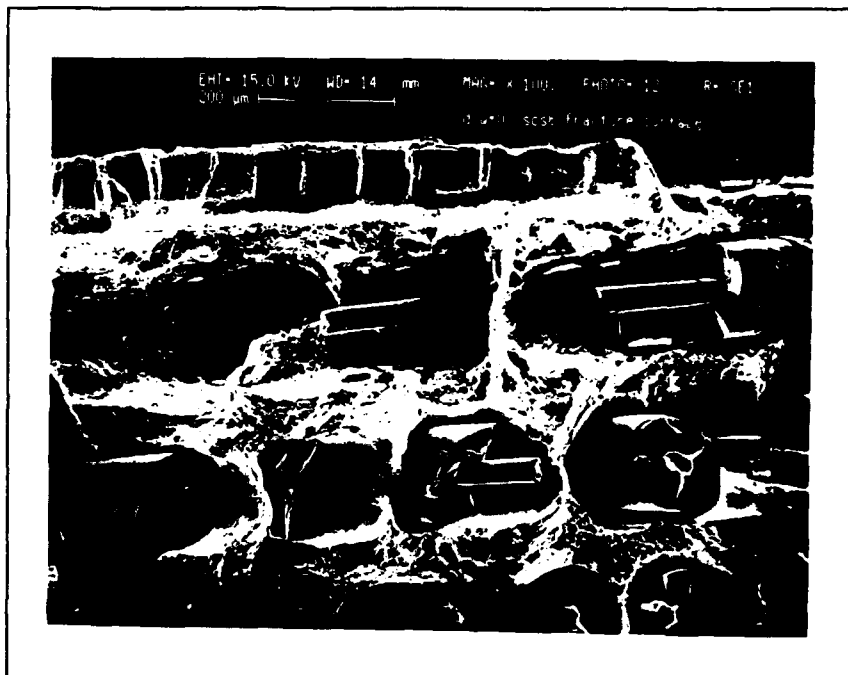


Figure 59. Unnotched SCS-6/Beta 21S, Fracture Surface, 100X

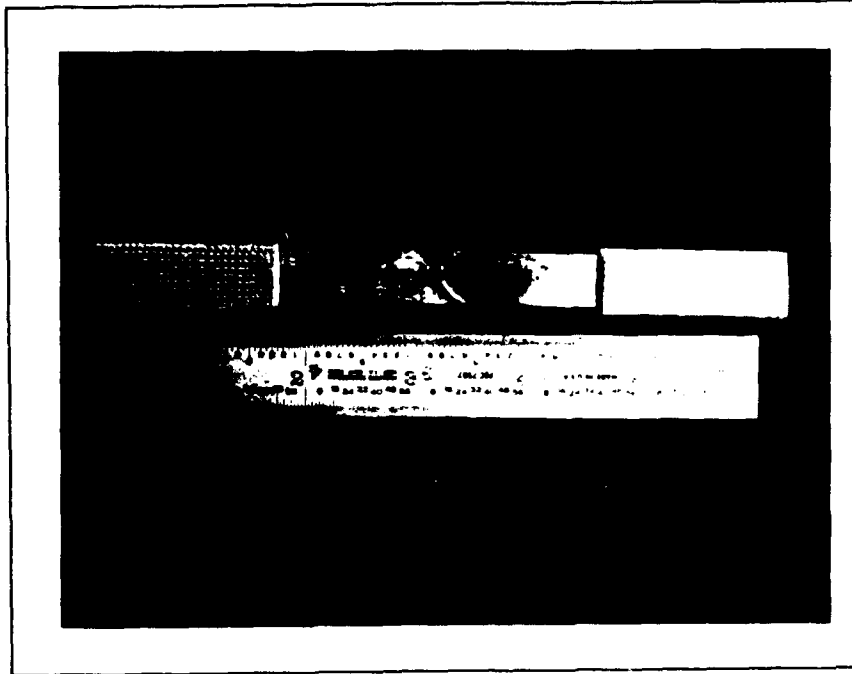


Figure 60. Notched SCS-6/Beta 21S, Room Temperature Compression Failure, $d/w=0.167$

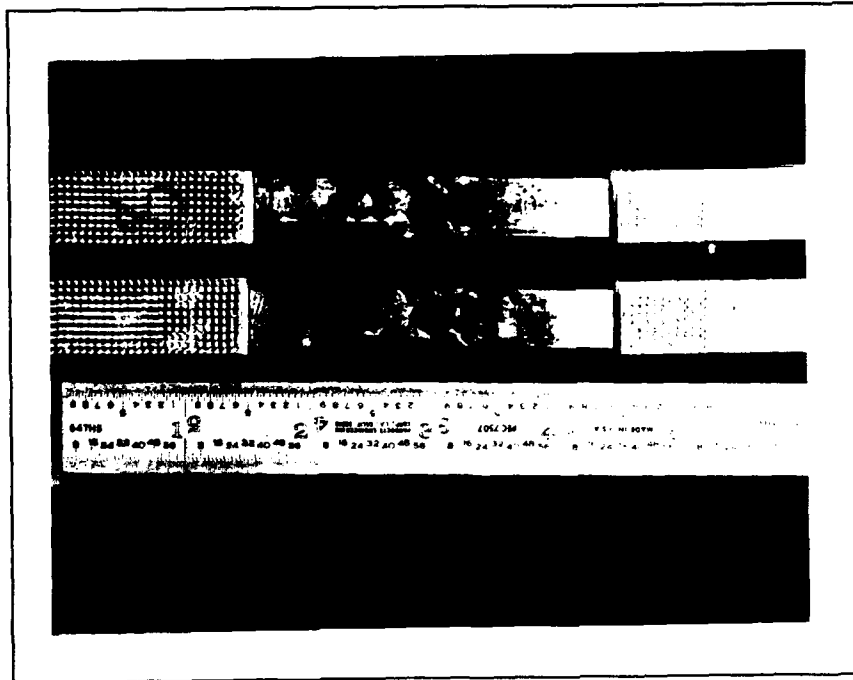


Figure 61. Notched SCS-6/Beta 21S, Room Temperature Compression Failure, $d/w=0.4$

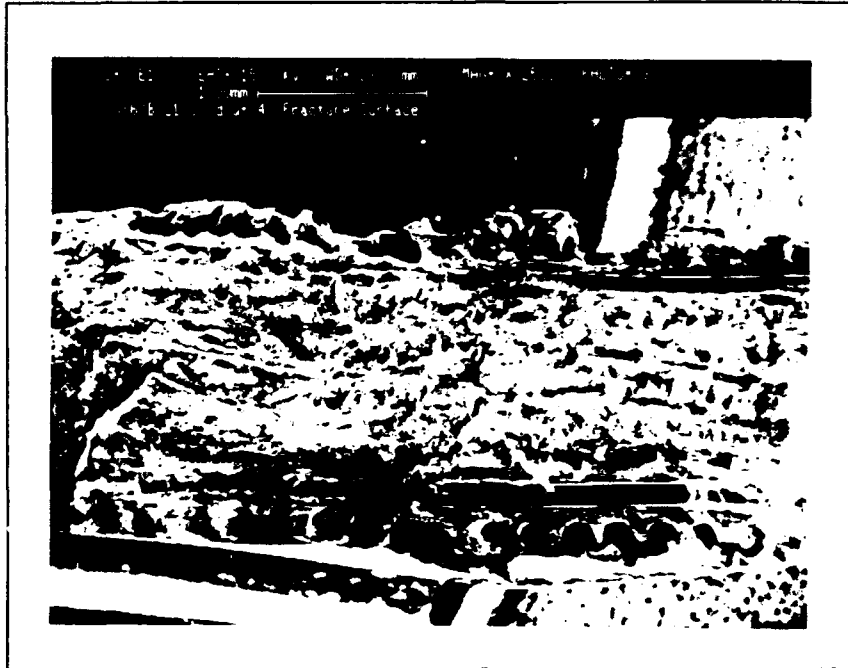


Figure 62. Notched SCS-6/Beta 21S, Fracture Surface of Room Temperature Specimen, 25X

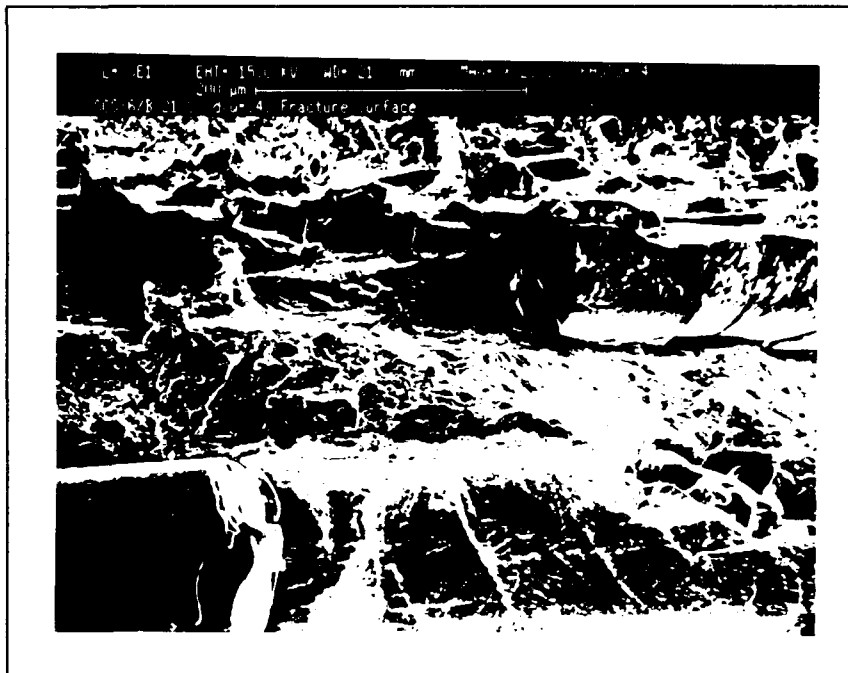


Figure 63. Notched SCS-6/Beta 21S, Fracture Surface of Room Temperature Specimen, 200X

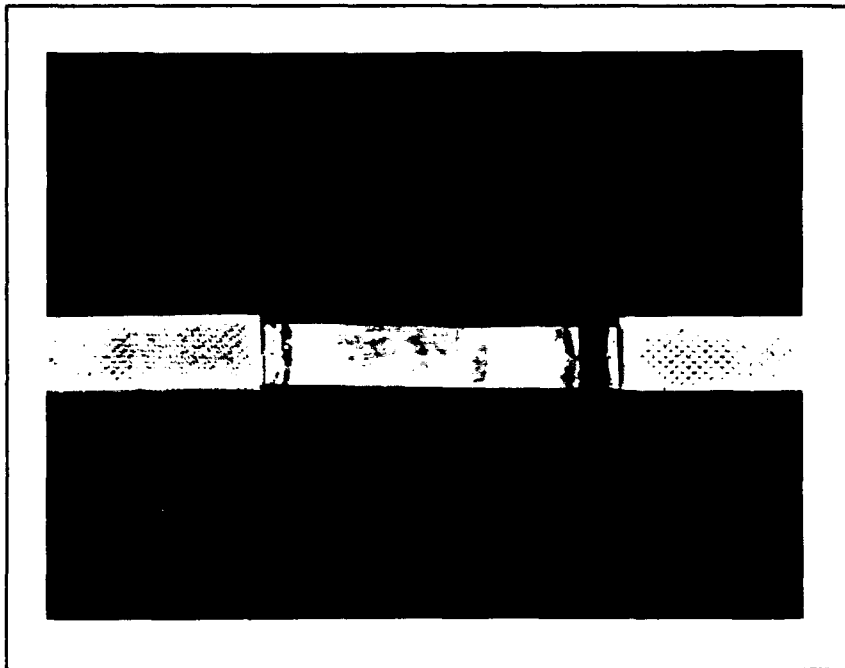


Figure 64. Unnotched SCS-6/Beta 21S, Elevated Temperature Compression Failure

⇒ LOAD ⇐

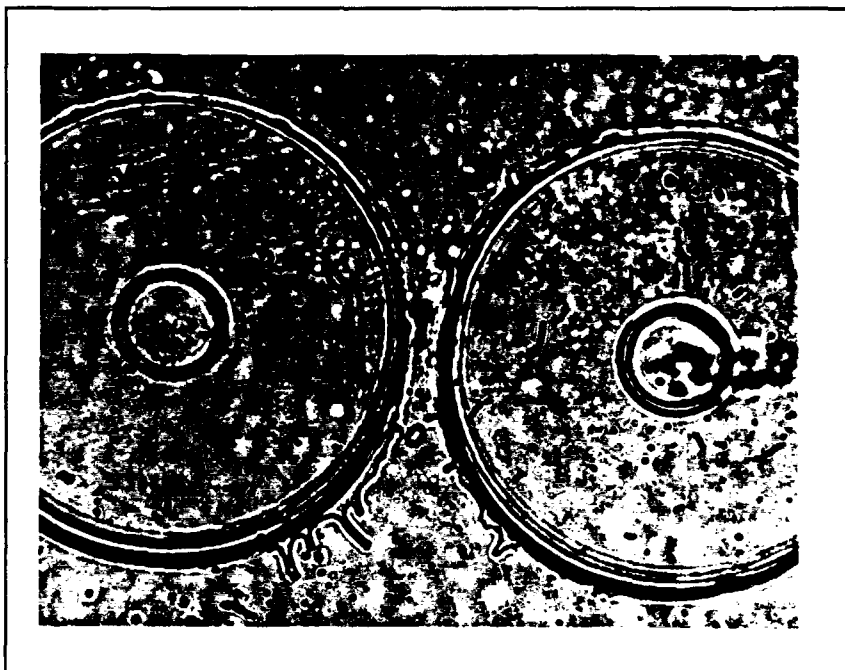


Figure 65. SCS-6/Beta 21S, Edge Replica of Elevated Temperature Specimen, Tested to 20% of Ultimate Strength, Showing 90° Fiber Debonding

↓
LOAD
↑

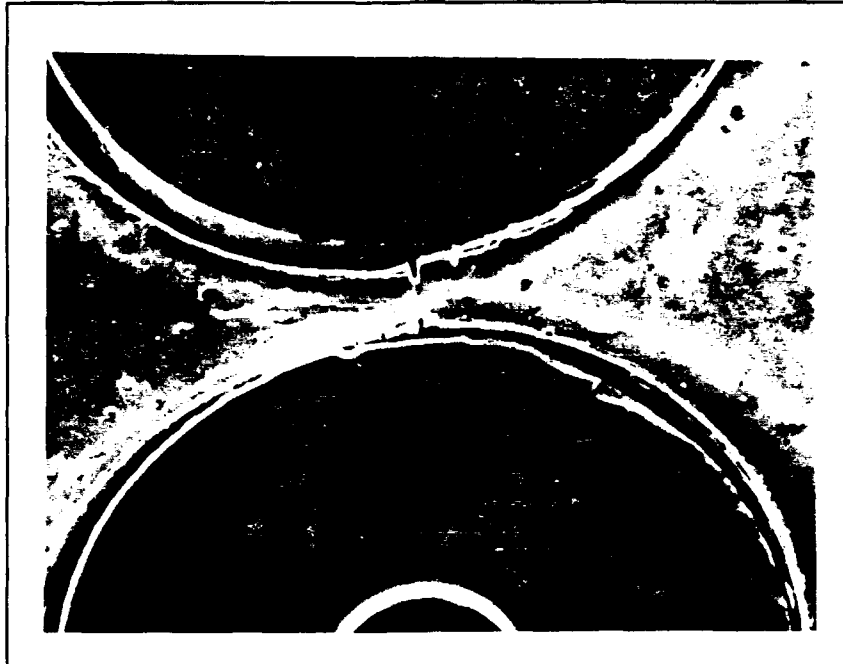


Figure 66. SCS-6/Beta 21S, Elevated Temperature Specimen, 90° Fibers at 90% of Ultimate Strength, 750X

↓
LOAD
↑

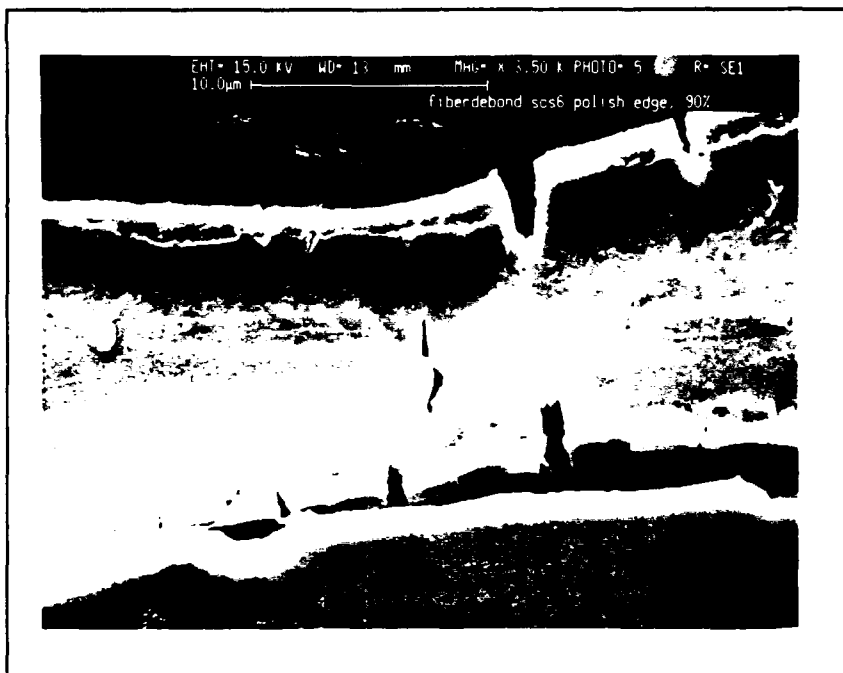


Figure 67. SCS-6/Beta 21S, Elevated Temperature Specimen, 90° Fibers at 90% of Ultimate Strength, 3500X

↓
LOAD
↑



Figure 68. SCS-6/Beta 21S, Elevated Temperature Specimen, 90° Fiber at 90% of Ultimate Strength, Showing Diffusiveness of Slip and Matrix Cracking, 2000X

Matrix plasticity appeared as extensive deformation on the fracture surface of the unnotched SCS-6/Beta 21S specimens (Fig. 69). Fiber debonding was evident on the fracture surface where the outer surface of the specimen was completely removed from a section of 0° fibers (Fig. 70). A higher magnification photo of that region showed that the outer carbon/titanium diboride (C/Ti B₂) coating of the fibers had separated and remained on the matrix surface in the fiber channels (Fig. 71). The unnotched failure of SCS-6/Beta 21S at 650° C occurred due to fiber failure, possibly as a result of in phase fiber microbuckling preceded by matrix shear failure and fiber debonding.

At 650° C, the notched SCS-6/Beta 21S specimens consistently failed at 45° to the loading axis, indicating failure in a shear mode (Figs. 72 and 73). Matrix plasticity was visually observed as deformation of the specimen in the region of the hole. The fracture surfaces were fused together in the failed specimens.

Edge replication showed that the elevated temperature failure progression of notched specimens paralleled that of unnotched specimens. However, the damage was initially observed in the edge region adjacent to the hole.

Notched specimens which had been loaded to 90% of ultimate strength were etched in the region adjacent to the hole and examined in the SEM. Fiber failure had occurred in the second fiber from the hole (Fig. 74). The first fiber did not appear to be damaged. It was not restricted from elastically deforming into the space of the hole.

The face of a failed notched specimen with $d/w = 0.167$ was examined in the SEM. The 0° fibers at the top and bottom of the hole were protruding into the space of the hole, indicating a great amount of fiber debonding (Fig. 75).



Figure 69. Unnotched SCS-6/Beta 21S, Fracture Surface of Elevated Temperature Specimen, 34X



Figure 70. Unnotched SCS-6/Beta 21S, Fracture Surface of an Elevated Temperature Specimen, Showing Fiber Debonding, 100X

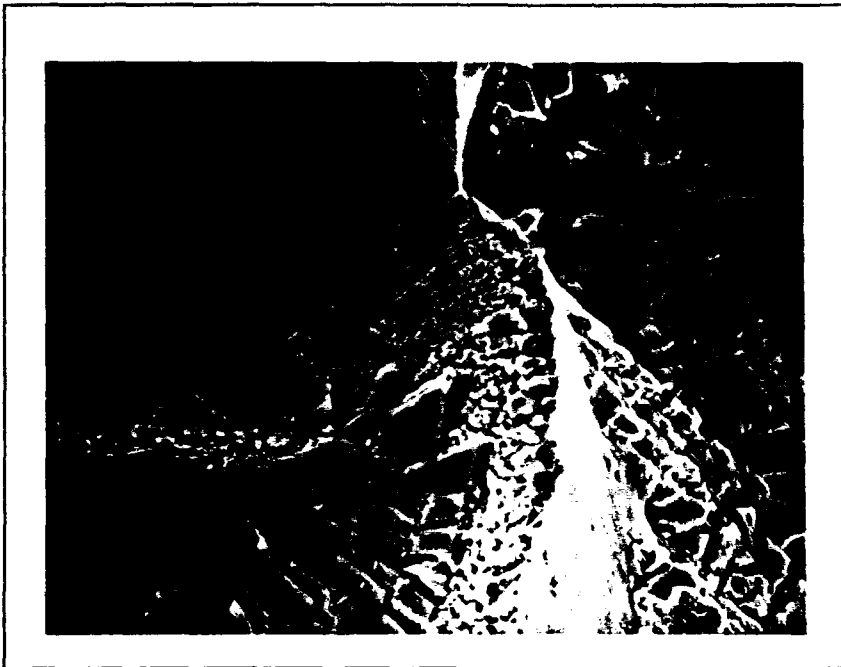


Figure 71. Unnotched SCS-6/Beta 21S, Fracture Surface of Elevated Temperature Specimen, Showing Separated C/TiB₂ Fiber Coating, 1000X

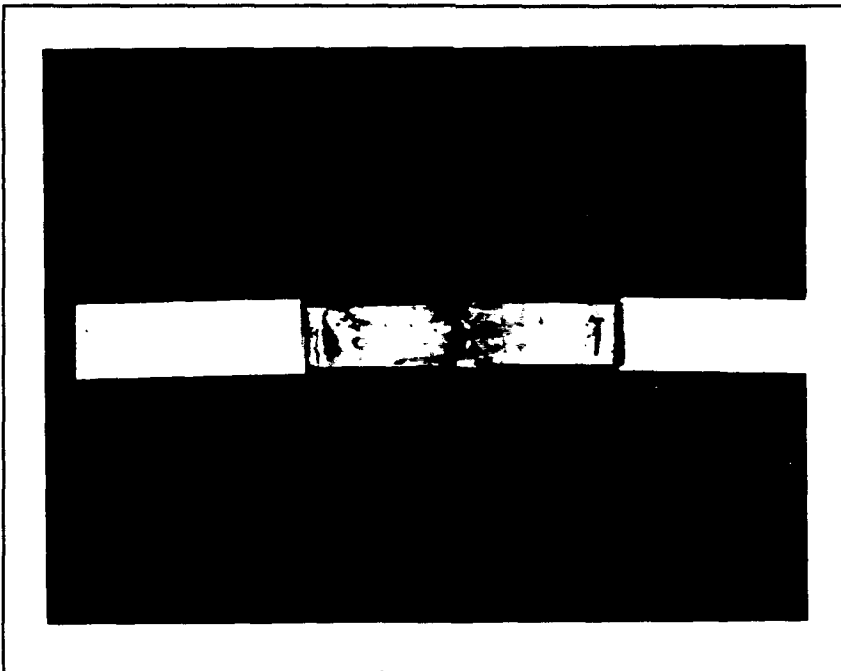


Figure 72. Notched SCS-6/Beta 21S, Elevated Temperature Failure Specimen, $d/w=0.167$

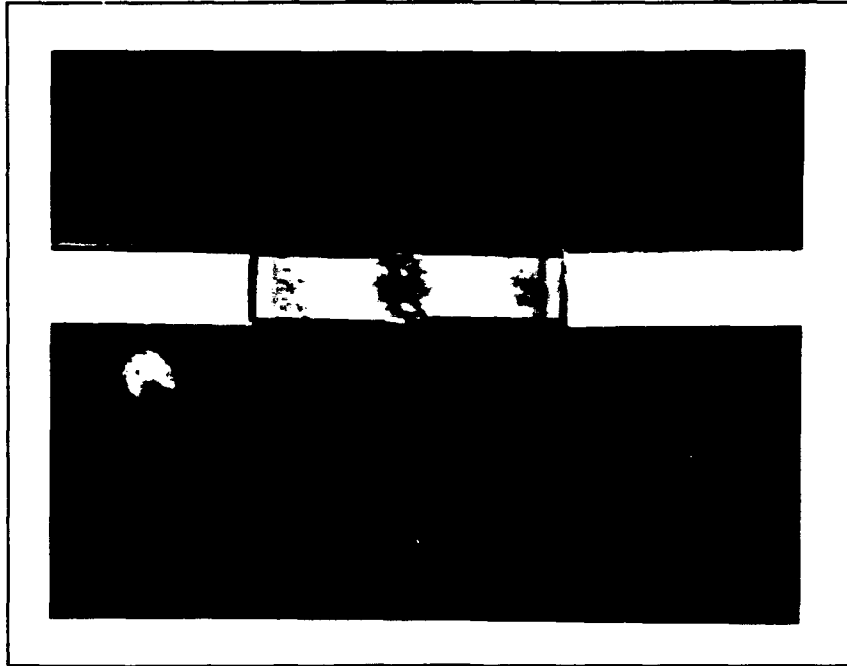


Figure 73. Notched SCS-6/Beta 21S, Elevated Temperature Failure Specimen, $d/w=0.4$

⇒ LOAD ⇐

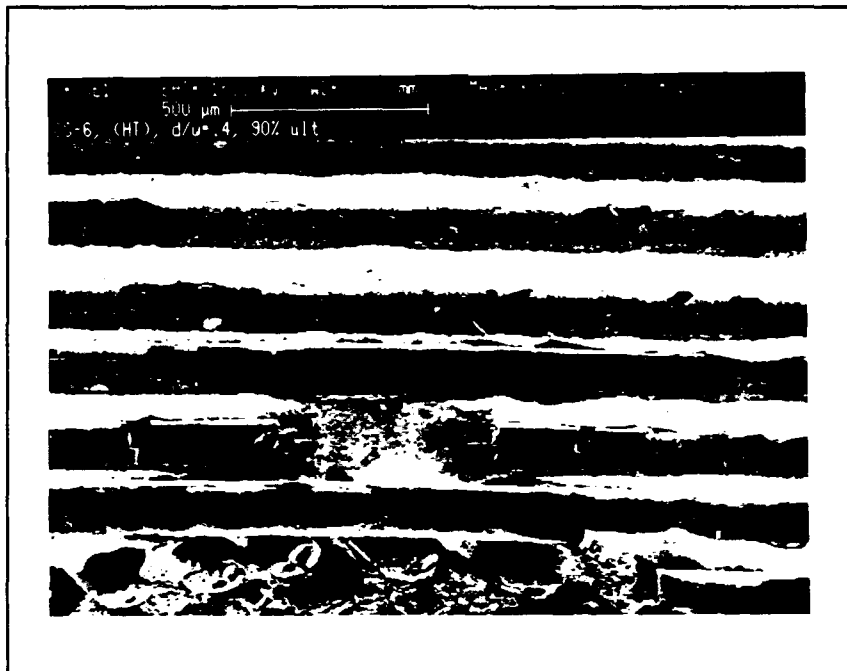


Figure 74. Notched SCS-6/Beta 21S, Etched Face of Elevated Temperature Specimen, 0° Fibers at 90% of Ultimate Strength, $d/w=0.4$, 50X

↓
LOAD
↑

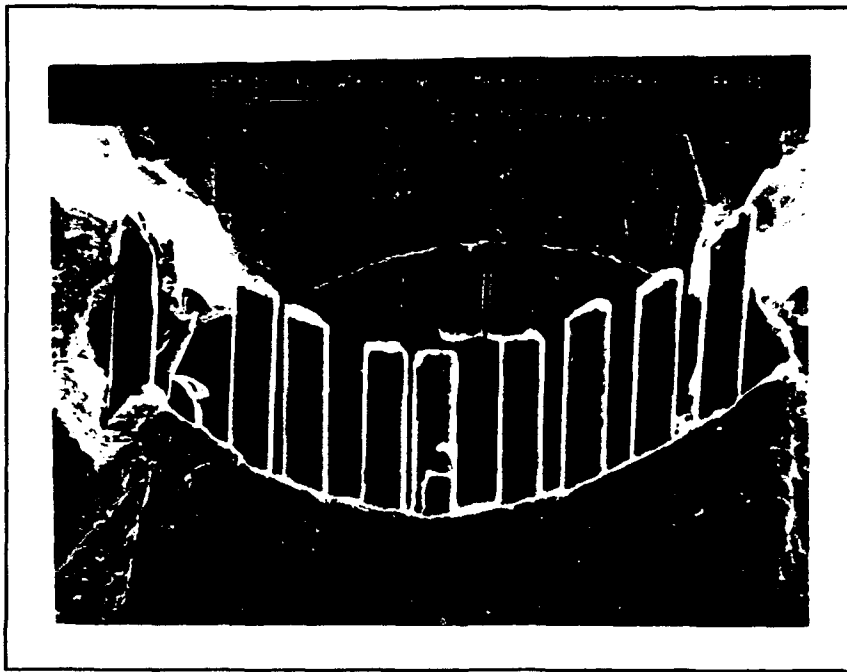


Figure 75. Notched SCS-6/Beta 21S, Face of Failed Elevated Temperature Specimen, $d/w=0.167$, Showing 0° Fiber Debonding Near the Hole, 50X

The edge of the failed specimen was analyzed and extensive 45° fiber protrusion, indicating extensive debonding, was observed along both edges (Figs. 76 and 77).

Failed notched specimens with $d/w=0.167$ were etched and examined in the SEM. The fibers around the hole were microbuckled, in phase, and broken at 45° to the loading axis (Figs. 78 and 79). This was the concrete evidence that fiber microbuckling had occurred, resulting in fiber cracking and matrix shear failure. The orientation of the fracture surface at 45° to the loading axis indicated failure in a shear mode. The notched failure of SCS-6/Beta 21S at 650° C was a result of fiber failure, caused by fiber microbuckling, preceded by matrix shear failure and fiber debonding.

⇒ LOAD ←

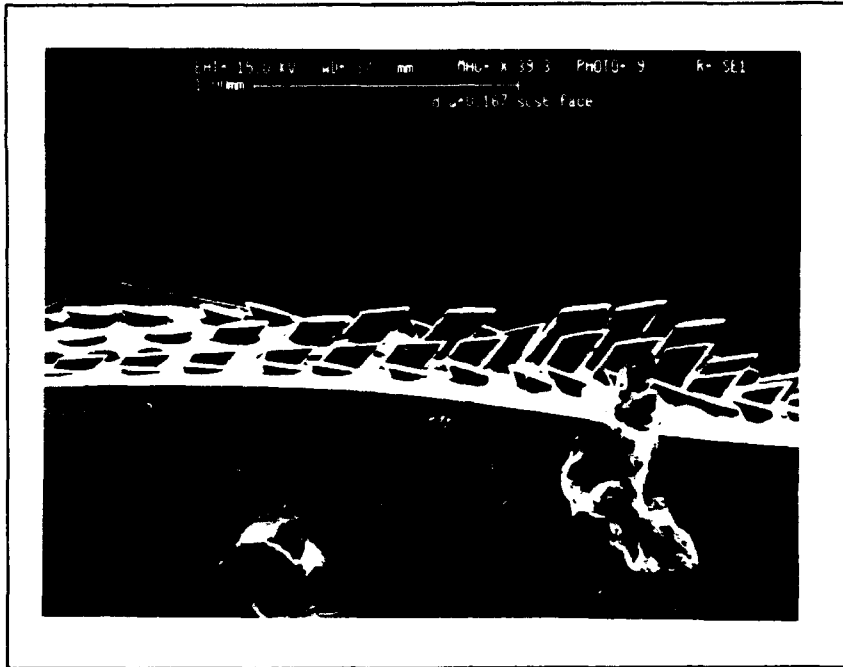


Figure 76. Notched SCS-6/Beta 21S, Elevated Temperature $d/w = 0.167$ Specimen, Showing 45° Fiber Debonding, 39X

⇒ LOAD ←



Figure 77. Notched SCS-6/Beta 21S, Elevated Temperature $d/w=0.167$ Specimen, 150X

↓
LOAD
↑



Figure 78. Notched SCS-6/Beta 21S, Etched Face of Elevated Temperature $d/w=0.167$ Specimen, 10X

↓
LOAD
↑



Figure 79. Notched SCS-6/Beta 21S, Etched Face of Elevated Temperature $d/w=0.167$ Specimen, 25X

V. Discussion

This chapter provides discussion on the analytical predictions, micro/macro mechanic relations, elevated temperature effects, and comparisons with previous work. In these sections, the analytical predictions and experimental test results are compared and discussed. Finally, comparisons are made with a previous unnotched compression study, and a previous notched tension study.

Analytical Predictions

This section is provided to show the strengths and weaknesses of the analytical predictions used in this research. METCAN and STRESS are discussed with reference to the usefulness of each for prediction of mechanical behavior.

METCAN. METCAN predicted internal failure mechanisms and composite elastic modulus of the Sigma/Beta 21S and SCS-6/Beta 21S using linear analysis. Reductions in elastic modulus due to plasticity and damage are not considered. METCAN was not used to model fiber/matrix interface because the interface properties are unknown. Without modeling the interface, fiber debonding cannot be predicted. These limitations contributed to inaccuracies in METCAN predictions. Another source of error is the database values for fiber compression and shear strengths. These fiber properties are difficult to measure, hence, they are provided with some uncertainty. The METCAN and experimental results are consolidated in Table 5.

Table 5. METCAN and Experimental Results

	Ply	Sigma/Beta 21S		SCS-6/Beta 21S Room Temperature		SCS-6/Beta 21S 650° C	
		METCAN	Experimental	METCAN	Experimental	METCAN	Experimental
Composite Modulus		177.3	157	152.6	139	133.3	81
Matrix Yield (MPa)	90°	600-800	1750	800-1000	831	350-400	Unknown
	45°			>1400	831	350-400	Unknown
	0°	1600-1800	1750	>1400	2079	>550	1218
Fiber Failure (MPa)	90°	>2000	1943	>1400	1040	>550	608
	45°			600-800	2079	500-550	1218
	0°	>2000	1943	1200-1400	2079	>550	1218

The elastic modulus predictions from METCAN were consistently high, but were within 13% error for Sigma/Beta 21S and SCS-6/Beta 21S at room temperature. The elastic modulus prediction for SCS-6/Beta 21S at 650° C was more than twice the experimental value. This error is attributed to the non-linear behavior of the material at elevated temperature. METCAN was used as a linear model which did not model the non-linearity of the elevated temperature material response.

Internal failure predictions were not extraordinarily accurate, but generally predicted internal failure at realistic stress levels. For Sigma/Beta 21S METCAN predicted matrix yield in the 90° plies at 30-40% of the ultimate strength. Experimentally, matrix yield in the 90° plies was not observed until 90% of ultimate strength. METCAN accurately predicted matrix yield in the 0° plies which occurred at 90% of ultimate strength. METCAN predicted no fiber failure in the Sigma/Beta 21S laminate before 2000 MPa. Experimentally,

fiber failure did not occur prior to specimen failure at 1943 MPa.

For room temperature SCS-6/Beta 21S METCAN accurately predicted matrix yield in the 90° plies which occurred at 38-48% of the ultimate strength. Experimentally, matrix yield was also observed in the 45° plies at 40% of the ultimate strength. METCAN inaccurately predicted fiber failure in the 45° plies instead. This error is attributed to the uncertainty of the fiber properties in shear. METCAN also inaccurately predicted 0° fiber failure at 60-70% of the ultimate strength and did not predict breakage (radial cracking) in the 90° fibers.

For elevated temperature SCS-6/Beta 21S METCAN predicted matrix yield in the 90° and 45° plies at 29-33% of the ultimate strength. Experimentally, matrix yield occurred extensively in those plies, but the initiation was not determined. METCAN inaccurately predicted breakage in the 45° fibers at 41-45% of ultimate strength, and failed to predict 90° fiber failure at 50%.

STRESS. STRESS was used to predict stress concentrations caused by a circular hole in Sigma/Beta 21S and SCS-6/Beta 21S laminates. For the two hole sizes, STRESS predicted large stress concentrations at the lateral edge of the hole. This result suggests that internal material failures should occur first in the region near the lateral edge of the hole. Experimentally, failure mechanisms were first observed on the specimen edges adjacent to the hole. However, in Sigma/Beta 21S, a longitudinal failure initiated at the top and bottom of the large size hole, $d/w=0.4$. Longitudinal failure was not expected, based on stress concentration factors calculated by STRESS. Longitudinal failure was a result of an internal failure mechanism, namely fiber microbuckling, which STRESS has no ability to model.

Micro/Macromechanical Relations

In MMCs, micromechanical (or internal) failures occur well before global material failure, affecting the macromechanical properties. The effect of micromechanical failures on the macromechanical properties of unnotched specimens is discussed in this section.

Sigma/Beta 21S, Room Temperature. The stress-strain curves for unnotched Sigma/Beta 21S specimens did not show non-linearity caused by fiber debonding at 25% of ultimate strength. In tensile tests, fiber debonding in a cross-ply MMC caused a non-linearity, or "knee", in the stress-strain curve (Roush, 1992: 51-55). In tension, debonding prevents load transfer into the fibers and matrix of affected plies, resulting in a laminate stiffness reduction. This reduction appears as a "knee" in the stress-strain curve. In compression, the Sigma/Beta 21S curve remained linear, suggesting purely elastic deformation, possibly fiber microbuckling, until matrix yielding occurred at 80-90% of the ultimate strength.

SCS-6/Beta 21S, Room Temperature. The stress-strain curves for unnotched SCS-6/Beta 21S specimens at room temperature did not show non-linearity caused by fiber debonding at 20% of ultimate strength. In tensile tests fiber debonding in this MMC caused a "knee" in the stress-strain curve at 15% of the ultimate strength (Rattray, 1992: 51-55). In compression, the curve became non-linear at 40-50% of the ultimate strength due to matrix plasticity in the 45° and 90° plies and fiber cracking in the 90° plies.

SCS-6/Beta 21S, Elevated Temperature. The stress-strain curves for unnotched SCS-6/Beta 21S specimens at 650° C showed non-linearity at 10-20% of the ultimate strength. This stress level coincided with fiber debonding.

However, the curve remained non-linear, indicating matrix plasticity may have contributed to the non-linearity.

Elevated Temperature Effect

Elevated temperature effects on macromechanical behavior, micromechanical behavior, and notch sensitivity are summarized in this section.

Macromechanical Behavior. The stress-strain curves for room and elevated temperature SCS-6/Beta 21S specimens were graphed simultaneously to clarify temperature effects (Fig. 80). Ultimate compressive strength and elastic modulus reductions are evident in the graph. The unnotched compressive strength was reduced 41% at 650° C. The elevated temperature elastic modulus was reduced 42% from the room temperature value. The elevated temperature curves exhibited a much earlier plasticity initiation, as observed in the non-linearity of the curves.

Micromechanical Behavior. The micromechanical behavior of SCS-6/Beta 21S was similar at room and elevated temperatures. Fiber debonding was evident at 20% of the ultimate strength at both temperatures. Matrix plasticity was extensive at both temperatures, but stress-strain curves indicate an earlier onset at 650° C. Fiber microbuckling may have occurred at both temperatures.

Notch Sensitivity. The effect of temperature on the notch sensitivity of SCS-6/Beta 21S was assessed through the use of net strength and normalized strength curves. The net strength line for each temperature was graphed as a theoretical prediction for notched strength (Fig. 81). The graph shows a slight decrease in notch sensitivity at elevated temperature. The same temperature effect may be illustrated using the normalized strength curve (Fig. 82).

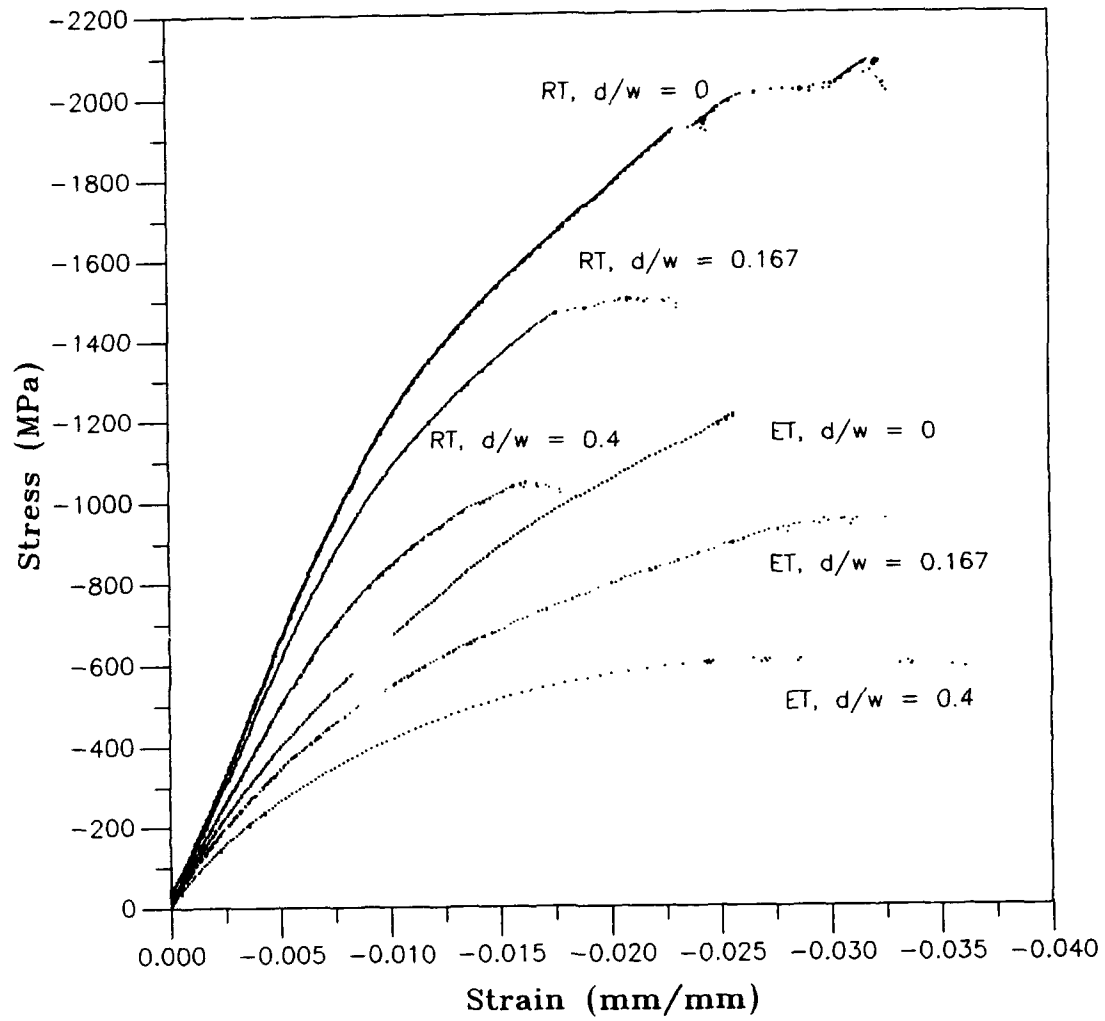


Figure 80. Room and Elevated Temperature Compression, SCS-6/Beta 21S

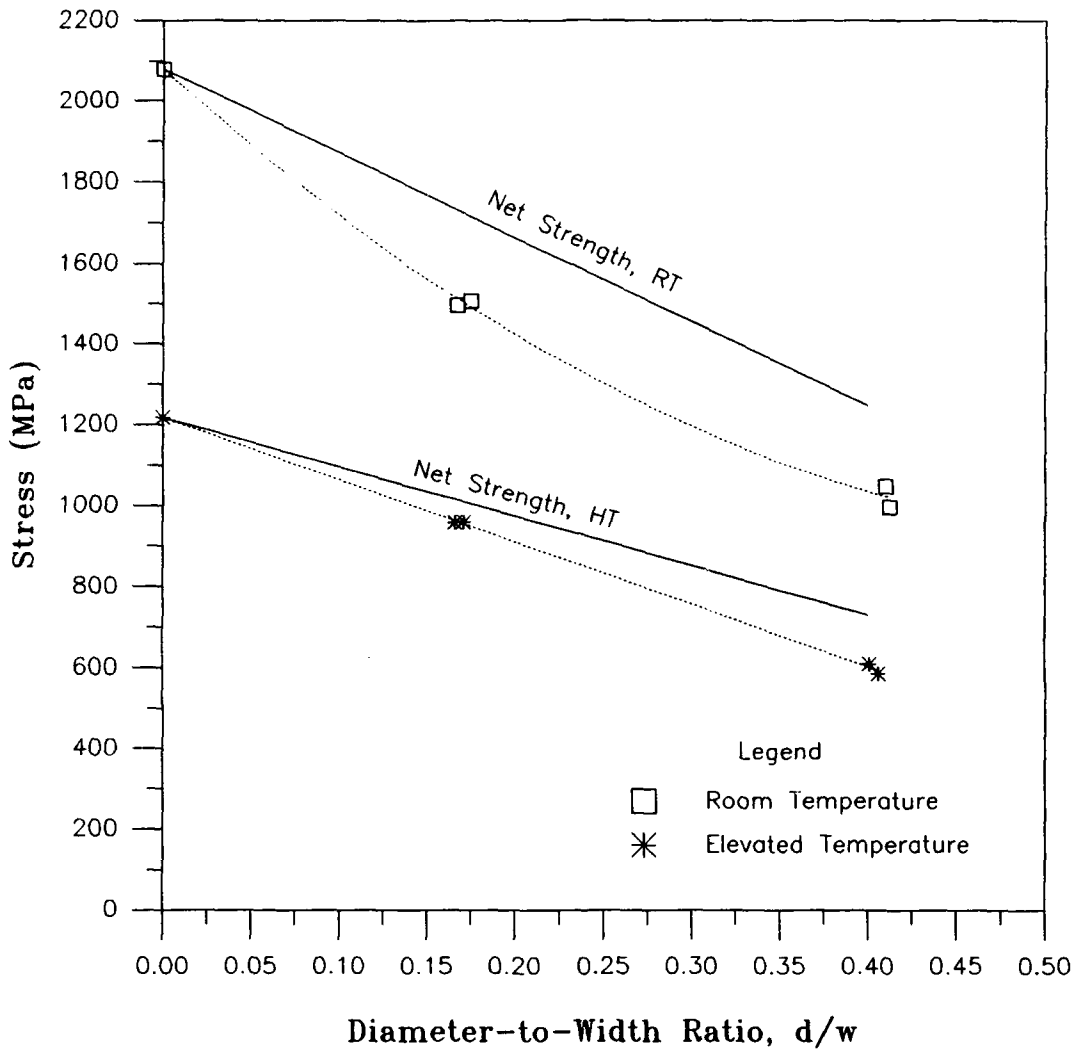


Figure 81. Room and Elevated Temperature Compressive Strength, Based on Remote Area, SCS-6/Beta 21S

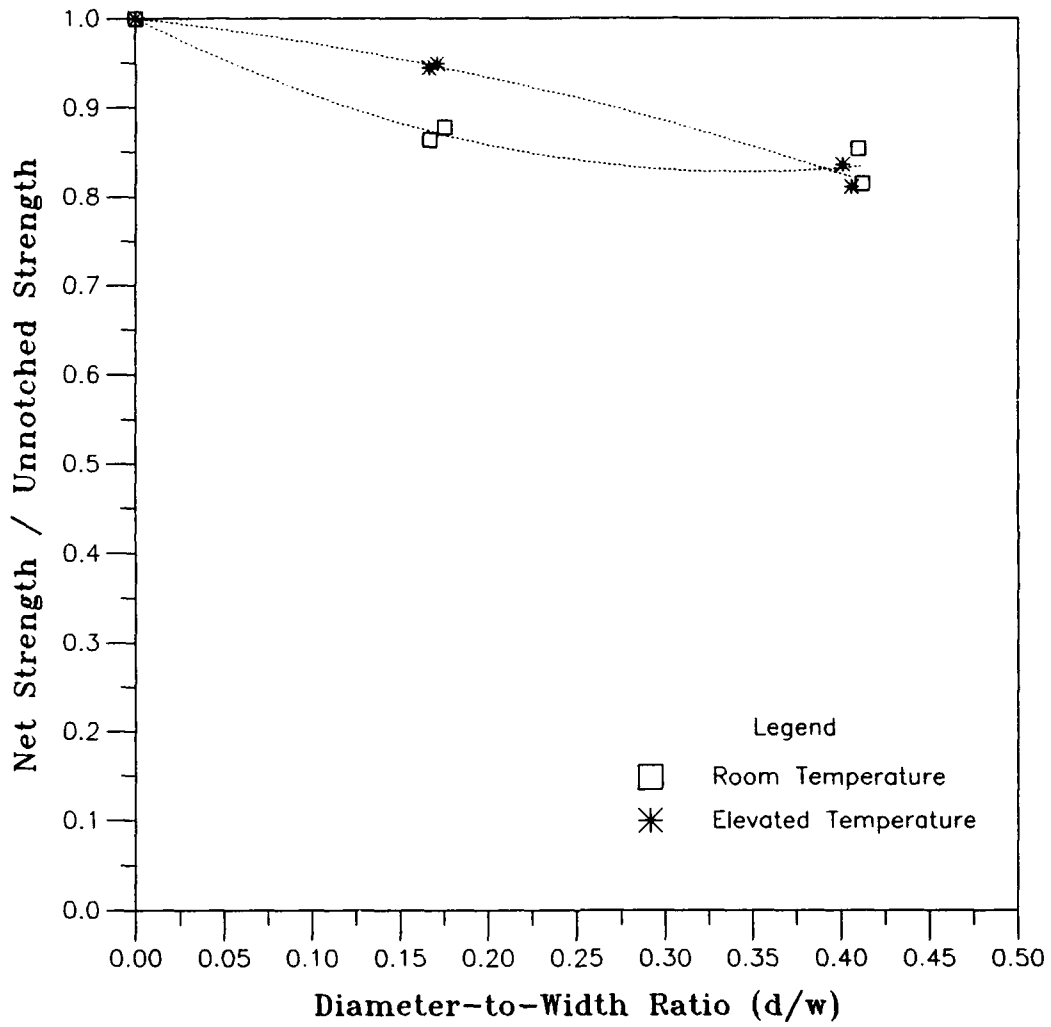


Figure 82. Normalized Strength, Room and Elevated Temperature Compression, SCS-6/Beta 21S

Comparison with A Previous Unnotched Compression Study

In this section, the failure modes for SCS-6/Beta 21S reported in this study are compared with a previous compression study on this MMC (Newaz and Majumdar, 1993).

The room temperature failure modes of unnotched SCS-6/Beta 21S, $[0/\pm 45/90]_8$, were fiber failure, preceded by fiber debonding, extensive matrix yielding, and radial fiber cracking. The failure mode at 650° C was fiber failure, preceded by matrix shear failure and fiber debonding. Newaz and Majumdar (1993) reported the room temperature and 650° C failure modes of SCS-6/Beta 21S, $[90]_8$, as matrix shear failure with fiber debonding and radial fiber cracking.

The explanation for the different combinations of failure modes lies in the construction of the MMC. The ply orientation is the most significant factor determining the modes of failure, given the same fiber and matrix. The $[0/\pm 45/90]_8$ orientation provides greater longitudinal support, due to the 0° fibers, which may prevent some of the damage observed in $[90]_8$.

Comparison with Previous Notched Tension Study

In this section, notched compressive behavior of SCS-6/Beta 21S is compared with its notched tensile behavior. The room temperature tensile failure modes of SCS-6/Beta 21S were reported by Rattray (1991) as ductile matrix failure, preceded by fiber failure. The 650° C failure modes were the same, exhibiting more matrix ductility. Rattray concluded that the notched tensile strength of the MMC is a function of the strength of the matrix. In compression, the room and elevated temperature failure modes of notched specimens were characterized by fiber failure, preceded by matrix yielding.

Hence, the notched compressive strength of the MMC is a function of the strength of the fibers.

SCS-6/Beta 21S in tension, exhibited mild notch sensitivity at room and elevated temperatures. In compression SCS-6/Beta 21S exhibited mild notch sensitivity at room temperature and slightly less notch sensitivity at 650° C.

VI. Conclusions and Recommendations

The main conclusions of this research are presented in this chapter. Material properties and macromechanical behavior of Sigma/Beta 21S and SCS-6/Beta 21S under compression at room temperature are quantified. The nature of micromechanical damage prior to specimen failure is described. The notch sensitivity of these materials is shown. Finally, the effect of temperature on material properties and behavior, damage progression and notch sensitivity is shown for SCS-6/Beta 21S. Recommendations for future research in related areas are submitted in this section.

The conclusions drawn from this research are:

1. Sigma/Beta 21S, $[0/90]_{2s}$, exhibited a room temperature compressive strength of 1943 MPa and an elastic modulus of 157 GPa. The material's stress-strain behavior was predominately elastic, but plastic in the final 10-20% of loading.
2. Sigma/Beta 21S, $[0/90]_{2s}$, sustained 90° fiber debonding and matrix cracking in 0° and 90° plies prior to specimen failure. For unnotched and notched specimens, fiber failure, due to fiber microbuckling preceded by massive fiber debonding, resulted in extensional mode failure.
3. Sigma/Beta 21S, $[0/90]_{2s}$, was mildly notch sensitive at room temperature.
4. SCS-6/Beta 21S, $[0/\pm 45/90]_s$, exhibited a room temperature compressive strength of 2079 MPa and an elastic modulus of 139 GPa. The material's stress-strain behavior was first elastic, then plastic for the final 50-60% of loading.

5. At room temperature, SCS-6/Beta 21S, $[0/\pm 45/90]_n$, sustained 45° and 90° fiber debonding and extensive matrix plasticity prior to specimen failure. For unnotched specimens, fiber failure, due to fiber microbuckling preceded by matrix yielding, resulted in extensional mode failure. For notched specimens, fiber failure, due to in phase fiber microbuckling preceded by matrix yielding, resulted in shear mode failure.

6. SCS-6/Beta 21S, $[0/\pm 45/90]_n$, was mildly notch sensitive at room temperature.

7. Elevated temperature reduced the strength and stiffness of SCS-6/Beta 21S, $[0/\pm 45/90]_n$. The elevated temperature compressive strength was 1218 MPa and stiffness was 81 GPa. The material's stress-strain behavior was predominately plastic, with a small elastic region in the first 10-20% of loading.

8. Elevated temperature did not significantly affect internal failure mechanisms of SCS-6/Beta 21S, $[0/\pm 45/90]_n$. The laminate sustained 45° and 90° fiber debonding and extensive matrix plasticity prior to specimen failure. For unnotched specimens, fiber failure, possibly due to fiber microbuckling preceded by extensive matrix yielding, resulted in shear mode failure. For notched specimens, fiber failure, due to in phase fiber microbuckling preceded by extensive matrix yielding, resulted in shear mode failure.

9. Elevated temperature reduced notch sensitivity of SCS-6/Beta 21S, $[0/\pm 45/90]_n$, in comparison to room temperature.

Recommendations for future research are:

1. Future work with MMCs should be conducted on heat treated materials. Industry and the engineering community are more concerned with experimental results obtained for heat treated materials.

2. The effect of a notch should be characterized in the tensile loading condition, for Sigma/Beta 21S.
3. Future notch effect studies should be conducted on any other MMCs in compression.
4. Tensile and compressive behavior studies should be conducted using unidirectional panels of new MMCs to evaluate lamina properties. The use of unidirectional laminates would allow comparisons between different fiber/matrix systems.

Bibliography

- Adams, D.F., "Test Methods for Composite Materials," Seminar Notes, Composite Materials Research Group, University of Wyoming. Lancaster: Technomic Publishing Company, March, 1991.
- Agarwal, B.D., and Broutman, L.J., *Analysis and Performance of Fiber Composites* (2nd Edition). New York: John Wiley and Sons, Inc., 1990.
- Ashbaugh, N., Memorandum on Beta 21S Test Characterization Data, WL/MLLN, Wright Laboratory, Wright-Patterson AFB, OH, 1993.
- American Society for Testing and Materials (ASTM), "Standard Test Method for Compressive Properties of Unidirectional or Crossply Fiber-Resin Composites," *ASTM Designation: D 3410-87*, Reprinted from the Annual Book of ASTM Standards, 1987.
- Awerbuch, J. and Madhukar, M., "Notched Strength of Composite Laminates: Predictions and Experiments--A Review," *Journal of Reinforced Plastics and Composites, Vol 4*, Technomic Publishing Co., 1985.
- Bearden, K. L. *Behavior of a Titanium Matrix Composite Under Quasi-Static Tensile and Compressive Loading*, MS Thesis, School of Engineering, Air Force Institute of Technology, Wright-Patterson AFB, OH, 1992.
- British Petroleum, "Sigma Monofilament: Fiber Performance Assurance", Unpublished Report for Materials Directorate of Wright Laboratory, 1991.
- Camponeschi, E.T., Jr., "Compression of Composite Materials: A Review," *Composite Materials: Fatigue and Fracture (Third Volume)*, ASTM STP 1110, T.K. O'Brien, Ed., American Society for Testing and Materials, Philadelphia, Pennsylvania, 1991, pp. 550-578.
- Cooke, C.M., Cammett, J.T., Eylon, D., and Smith, P.R., "Edge Preparation of Titanium Matrix Composite Specimens for Mechanical Testing," Elsevier Science Publishing Co., Inc., 1982.
- Daniel, I.M., "Chapter VI, Methods of Testing Composite Materials," *Handbook of Composites, Vol.3-Failure Mechanics of Composites*, Sih, G.C., and Skudra, A.M., Eds., The Netherlands: Elsevier Science Publishers B.V., 1985, pp. 277-327.

- Derriso, M. and Sanders, B., "STATIC", Version 1.0, AFIT/ENY, Data Acquisition Software, Unpublished, 1992.
- Duffy, L.B., "Manufacture of Carbon Fiber Reinforced Structural Tubular Struts Using Liquid Pressure Forming Process," *Space Applications of Advanced Structural Materials*, ESA Publications Division, ESTEC, Noordwijk, The Netherlands, June, 1990.
- Hansen, D.G., *Thermomechanical Fatigue of SCS-6/Beta 21S [0/90]_{2s} Composite*, MS Thesis, AFIT/GAE/ENY/91D-9, School of Engineering, Air Force Institute of Technology, Wright-Patterson AFB, OH, 1991.
- Harmon, D.M., Saff, C.R., and Graves, D.L., "Strength Predictions for Metal Matrix Composites," *Metal Matrix Composites: Testing, Analysis, and Failure Modes, ASTM STP 1032*, W.S. Johnson, Ed., American Society for Testing and Materials, Philadelphia, Pennsylvania, 1989, pp. 222-236.
- Hopkins, D.A., and Chamis, C.C., "A Unique Set of Micromechanical Equations for High Temperature Metal Matrix Composites," (Prepared for the First Symposium on Testing Technology of Metal Matrix Composites, American Society for Testing and Materials, Tennessee), NASA Lewis Research Center, Cleveland, Ohio, 1985.
- , and Murthy, P.L.N., "Metal Matrix Composite Analyzer User's Guide" (Version 3.0), NASA Lewis Research Center, Cleveland, Ohio, 1989.
- Johnson, W.S., "Fatigue Testing and Damage Development in Continuous Fiber Reinforced Metal Matrix Composites," *NASA TM-100628*, June, 1988.
- , Lubowinski, S.J., Brewer, W.D. and Hoogstraten, C.A., "Mechanical Characterization of SCS6/Ti 15-3 Metal Matrix Composite at Room Temperature", NASP Technical Memorandum No. 1014 (Langley Research Center, NASA), 1988.
- Kennedy, J.M., "Tension and Compression Testing of Metal Matrix Composite Materials," *Metal Matrix Composites: Testing, Analysis, and Failure Modes, ASTM STP 1032*, W.S. Johnson, Ed., American Society for Testing and Materials, Philadelphia, Pennsylvania, 1989, pp. 7-18.

- Lamothe, R.M., and Nunes, J., "Evaluation of Fixturing for Compression Testing Of Metal Matrix and Polymer/Epoxy Composites," *Compression Testing of Homogeneous Materials and Composites, ASTM STP 808*, Richard Chait and Ralph Paprino, Eds., American Society for Testing and Materials, 1983, pp. 241-253.
- Larson, J.M., and Russ, S.M., Memorandum for Record, "Machining and Heat Treating Guidelines for NIC Beta 21S Composite Specimens," Wright Laboratory, Wright-Patterson AFB, OH, (Meeting Summary) 25 September 1991.
- Lee, J.H. and Mall, S., "Experimental Investigation of Quasi-Isotropic Graphite/Epoxy Laminate with a Reinforced Hole," Proceedings of 3rd Technical Conference on Composite Materials 384-391, Seattle, WA, 1988.
- Lekhnitskii, S.G., *Anisotropic Plates*, Translated from The Second Russian Edition by S.W. Tsai and T. Cheron. New York: Gordon and Breach Science Publishers, 1968.
- Macoma Incorporated, "Bioden R.F.A., Acetylcellulose Replicating Film for New Two-Step Replica Method (Filmy Replica System)," Directions for Use, Undated.
- Majumdar, B.S., and Newaz, G.M., "Inelastic Deformation of Metal Matrix Composites: Compression and Fatigue," Proceedings of the 5th Annual *HITEMP Review*, Cleveland, Ohio, 1992a.
- , and Newaz, G.M., "Inelastic Deformation of Metal Matrix Composites: Plasticity and Damage Mechanisms," *Philosophical Magazine A*, Vol. 66, No. 2, Columbus, Ohio, 1992b, pp. 187-212.
- , and Newaz, G.M., "Inelastic Deformation of Metal Matrix Composites: Plasticity and Damage Mechanisms--Part II," NASA Contractor Report 189096--Part II, Columbus, Ohio, 1992c.
- , Newaz, G.M., and Brust, F.W., "Constitutive Behavior of Metal Matrix Composites," MD-Vol. 40, *Constitutive Behavior of High-Temperature Composites*, ASME, 1992.
- Mitnick, M.A., and McElman, J., "Continuous Silicon Carbide Reinforced Metal Matrix Composites," Proceedings of 3rd Technical Conference on Composite Materials at Seattle, WA, 26-29 September, 1988, pp. 395-403.

- Newaz, G.M., and Majumdar, B.S., "Crack Initiation Around Holes in A Unidirectional MMC under Fatigue Loading," *Engineering Fracture Mechanics*, Vol. 42, No. 4, Pergamon Press Ltd., Great Britain, 1992, pp. 699-711.
- , and Majumdar, B.S., "Failure Modes in Transverse Metal-Matrix Composite Lamina under Compression", *Journal of Materials Science Letters 12*, Chapman and Hall, 1993, 551-552.
- , and Majumdar, B.S., "Inelastic Deformation Mechanisms in A Transverse MMC Lamina under Compression," AD-Vol. 27, *Fracture and Damage*, ASME, 1992.
- , PhD, Battelle Memorial Institute, Columbus, OH. Personal Interview, 4 August, 1993.
- Ontko, N., Memorandum on NASP Data Base--Tensile Data, WL/MSLE, Wright Laboratory, Wright-Patterson AFB, OH, 1993.
- Park, H.S., Zong, G.S., Brown, L.D., Rabenberg, L., and Marcus, H.L., "Fiber-Matrix Interface Failures," *Metal Matrix Composites: Testing, Analysis, and Failure Modes*, ASTM STP 1032, W.S. Johnson, Ed., American Society for Testing and Materials, Philadelphia, Pennsylvania, 1989, pp. 270-279.
- Pickard, S.M., Miracle, D.B., Majumdar, B., Kendig, K., Rothenflue, L., and Coker, D., "An Experimental Study of Residual Fiber Strains in Ti-15-3 Continuous Fiber Composites," Unpublished, 1993.
- Prewo, K.M., "The Notched Tensile Behavior of Metal Matrix Composites," *Composite Materials: Testing and Design (Third Conference)*, ASTM STP 546, American Society for Testing and Materials, 1974, pp. 507-522.
- Rattray, J., *Tensile Characterization of a Metal Matrix Composite with Circular Holes*, MS Thesis, School of Engineering, Air Force Institute of Technology, Wright-Patterson AFB, OH, 1991.
- Roush, J.T., *Open and Filled Hole Static Tensile Strength Characterization of Metal Matrix Composite SCS-9/Beta 21S*, MS Thesis, School of Engineering, Air Force Institute of Technology, Wright-Patterson AFB, OH, 1992.

- Santhosh, U., Ahmad, J., and Nagar, A., "Non-Linear Micromechanics Analysis Prediction of the Behavior of Titanium Alloy Matrix Composites," *Fracture and Damage, ASME, Vol. 27*, 1992.
- Sinclair, J.H., and Chamis, C.C., "Compressive Behavior of Unidirectional Fibrous Composites," *Compression Testing of Homogeneous Materials and Composites, ASTM STP 808*, Richard Chait and Ralph Paprino, Eds., American Society for Testing and Materials, 1983, pp. 155-174.
- Soutis, C., Fleck, N.A., and Curtis, P.T., "Hole-Hole Interaction in Carbon Fibre/Epoxy Laminates under Uniaxial Compression," *Composites*, Vol. 22, No. 1, January 1991.
- Tan, S.C., "Finite-Width Correction Factors for Anisotropic Plate Containing a Central Opening," *Journal of Composite Materials*, Vol. 22, November 1988, pp. 1080-1097.
- Tarnopol'skii, Y.M., and Kincis, T., "Chapter V, Static Testing, " *Failure Mechanics of Composites, Handbook of Composites, Vol. 3*, Sih, G.C., and Skudra, A.M., Volume Eds. The Netherlands: Elsevier Science Publishers, B.V., 1985, pp. 229-231.
- TIMET, "Data Sheet TIMETAL[®] 21S (Ti-15Mo-3Nb-3Al-.2Si) High Strength, Oxidation Resistant Strip Alloy," Unpublished Report to WL/MLLN, Undated.

APPENDIX A

Sigma/Beta 21S [0/90]_{2s} Predictions

Constituent properties

$$E_m := 115 \cdot 10^9 \text{ Pa} \quad E_f := 400 \cdot 10^9 \text{ Pa} \quad V_f := 0.31$$

Rule of Mixtures $E_1 := V_f E_f + (1 - V_f) \cdot E_m$ $E_1 = 2.0335 \cdot 10^{11} \text{ Pa}$

Halpin-Tsai Equations

Let $\xi := 2$

$$\eta := \frac{\left(\frac{E_f}{E_m}\right) - 1}{\left(\frac{E_f}{E_m}\right) + \xi} \quad \eta = 0.4524$$

$$E_2 := E_m \cdot \left(\frac{1 + \xi \cdot \eta \cdot V_f}{1 - \eta \cdot V_f}\right) \quad E_2 = 1.7127 \cdot 10^{11} \text{ Pa}$$

For shear properties, let $\xi := 1$

Let $\nu_m := 0.34$ $\nu_f := 0.26$

$$G_m := \frac{E_m}{2 + 2 \cdot \nu_m} \quad G_f := \frac{E_f}{2 + 2 \cdot \nu_f}$$

$$\eta := \frac{\left(\frac{G_f}{G_m}\right) - 1}{\left(\frac{G_f}{G_m}\right) + \xi} \quad \eta = 0.5744$$

$$G_m = 4.291 \cdot 10^{10} \text{ Pa} \quad G_f = 1.5873 \cdot 10^{11} \text{ Pa}$$

$$G_{12} := G_m \cdot \left(\frac{1 + \xi \cdot \eta \cdot V_f}{1 - \eta \cdot V_f}\right) \quad G_{12} = 6.1502 \cdot 10^{10} \text{ Pa}$$

$$\nu_{12} := V_f \nu_f + (1 - V_f) \cdot \nu_m \quad \nu_{12} = 0.3152$$

$$\nu_{21} := \frac{\nu_{12} \cdot E_2}{E_1} \quad \nu_{21} = 0.2655$$

Classical laminated plate theory

The reduced stiffness matrix

$$Q := \begin{bmatrix} \frac{E_1}{1 - \nu_{12} \cdot \nu_{21}} & \frac{\nu_{12} \cdot E_2}{1 - \nu_{12} \cdot \nu_{21}} & 0 \\ \frac{\nu_{12} \cdot E_2}{1 - \nu_{12} \cdot \nu_{21}} & \frac{E_2}{1 - \nu_{12} \cdot \nu_{21}} & 0 \\ 0 & 0 & G_{12} \end{bmatrix} \quad Q = \begin{bmatrix} 2.2192 \cdot 10^{11} & 5.8916 \cdot 10^{10} & 0 \\ 5.8916 \cdot 10^{10} & 1.8691 \cdot 10^{11} & 0 \\ 0 & 0 & 6.1502 \cdot 10^{10} \end{bmatrix}$$

The transformation matrix

$$T(\theta) := \begin{bmatrix} \cos(\theta)^2 & \sin(\theta)^2 & 2 \cdot \sin(\theta) \cdot \cos(\theta) \\ \sin(\theta)^2 & \cos(\theta)^2 & -2 \cdot \sin(\theta) \cdot \cos(\theta) \\ -\sin(\theta) \cdot \cos(\theta) & \sin(\theta) \cdot \cos(\theta) & \cos(\theta)^2 - \sin(\theta)^2 \end{bmatrix}$$

$$Qbar_0 := Q$$

$$Qbar_{90} := T\left(\frac{\pi}{2}\right)^{-1} \cdot Q \cdot T\left(\frac{\pi}{2}\right) \quad Qbar_{90} = \begin{bmatrix} 1.8691 \cdot 10^{11} & 5.8916 \cdot 10^{10} & 0 \\ 5.8916 \cdot 10^{10} & 2.2192 \cdot 10^{11} & 0 \\ 0 & 0 & 6.1502 \cdot 10^{10} \end{bmatrix}$$

Laminate thickness

Single ply thickness

$$t := 1.097 \cdot 10^{-3}$$

$$t_k := \frac{t}{8}$$

$$t_k = 1.3713 \cdot 10^{-4}$$

$$A := 4 \cdot t_k \cdot (Qbar_0 + Qbar_{90})$$

$$A = \begin{bmatrix} 2.2425 \cdot 10^8 & 6.463 \cdot 10^7 & 0 \\ 6.463 \cdot 10^7 & 2.2425 \cdot 10^8 & 0 \\ 0 & 0 & 6.7468 \cdot 10^7 \end{bmatrix}$$

For balanced-symmetric
ply orientation

$$E_x := \frac{A_{1,1} \cdot A_{2,2} - (A_{1,2})^2}{A_{2,2} \cdot t} \quad E_x = 1.8744 \cdot 10^{11} \text{ Pa}$$

$$E_y := \frac{A_{1,1} \cdot A_{2,2} - (A_{1,2})^2}{A_{1,1} \cdot t} \quad E_y = 1.8744 \cdot 10^{11} \text{ Pa}$$

$$\nu_{xy} := \frac{A_{1,2}}{A_{2,2}} \quad \nu_{xy} = 0.2882$$

$$G_{xy} := \frac{A_{3,3}}{t} \quad G_{xy} = 6.1502 \cdot 10^{10} \text{ Pa}$$

SCS-6/Beta 21S [0/±45/90] Predictions

Constituent properties $E_m = 89 \cdot 10^9 \text{ Pa}$ $E_f = 414 \cdot 10^9 \text{ Pa}$ $V_f = 0.35$

Rule of mixtures $E_1 = V_f E_f + (1 - V_f) \cdot E_m$ $E_1 = 2.0275 \cdot 10^{11} \text{ Pa}$

Halpin-Tsai Equations

Let $\xi = 2$

$$\eta = \frac{\left(\frac{E_f}{E_m}\right) - 1}{\left(\frac{E_f}{E_m}\right) + \xi} \quad \eta = 0.549$$

$$E_2 = E_m \cdot \left(\frac{1 + \xi \cdot \eta \cdot V_f}{1 - \eta \cdot V_f}\right) \quad E_2 = 1.525 \cdot 10^{11} \text{ Pa}$$

For shear properties, let $\xi = 1$

$$v_m = 0.34 \quad v_f = 0.26 \quad G_m = \frac{E_m}{2 + 2 \cdot v_m} \quad G_f = \frac{E_f}{2 + 2 \cdot v_f}$$

$$G_m = 3.3209 \cdot 10^{10} \text{ Pa} \quad G_f = 1.6429 \cdot 10^{11} \text{ Pa}$$

$$\eta = \frac{\left(\frac{G_f}{G_m}\right) - 1}{\left(\frac{G_f}{G_m}\right) + \xi} \quad \eta = 0.6637$$

$$G_{12} = G_m \cdot \left(\frac{1 + \xi \cdot \eta \cdot V_f}{1 - \eta \cdot V_f}\right) \quad G_{12} = 5.3306 \cdot 10^{10} \text{ Pa}$$

$$v_{12} = V_f v_f + (1 - V_f) \cdot v_m \quad v_{12} = 0.312$$

$$v_{21} = \frac{v_{12} \cdot E_2}{E_1} \quad v_{21} = 0.2347$$

Classical laminated plate theory

$$Q_{bar}_0 = Q \quad \left[\begin{array}{ccc} 2.2192 \cdot 10^{11} & 5.8916 \cdot 10^{10} & 0 \\ 5.8916 \cdot 10^{10} & 1.8691 \cdot 10^{11} & 0 \\ 0 & 0 & 6.1502 \cdot 10^{10} \end{array} \right]$$

$$\bar{Q}_{90} := T\left(\frac{\pi}{2}\right)^{-1} \cdot Q \cdot T\left(\frac{\pi}{2}\right)^{-1}$$

$$\bar{Q}_{90} = \begin{bmatrix} 1.8691 \cdot 10^{11} & 5.8916 \cdot 10^{10} & 0 \\ 5.8916 \cdot 10^{10} & 2.2192 \cdot 10^{11} & 0 \\ 0 & 0 & 6.1502 \cdot 10^{10} \end{bmatrix}$$

$$\bar{Q}_{45} := T\left(\frac{\pi}{4}\right)^{-1} \cdot Q \cdot T\left(\frac{\pi}{4}\right)^{-1}$$

$$\bar{Q}_{45} = \begin{bmatrix} 1.9317 \cdot 10^{11} & 7.0164 \cdot 10^{10} & 8.7513 \cdot 10^9 \\ 7.0164 \cdot 10^{10} & 1.9317 \cdot 10^{11} & 8.7513 \cdot 10^9 \\ 8.7513 \cdot 10^9 & 8.7513 \cdot 10^9 & 7.2751 \cdot 10^{10} \end{bmatrix}$$

$$\bar{Q}_{-45} := T\left(-\frac{\pi}{4}\right)^{-1} \cdot Q \cdot T\left(-\frac{\pi}{4}\right)^{-1}$$

$$\bar{Q}_{-45} = \begin{bmatrix} 1.9317 \cdot 10^{11} & 7.0164 \cdot 10^{10} & -8.7513 \cdot 10^9 \\ 7.0164 \cdot 10^{10} & 1.9317 \cdot 10^{11} & -8.7513 \cdot 10^9 \\ -8.7513 \cdot 10^9 & -8.7513 \cdot 10^9 & 7.2751 \cdot 10^{10} \end{bmatrix}$$

Laminate thickness

Single ply thickness

$$t := 1.745 \cdot 10^{-3}$$

$$t_k := \frac{t}{8}$$

$$t_k = 0.000218$$

$$A := 2 \cdot t_k \cdot (\bar{Q}_{00} + \bar{Q}_{90} + \bar{Q}_{45} + \bar{Q}_{-45})$$

$$A = \begin{bmatrix} 3.4689 \cdot 10^8 & 1.1262 \cdot 10^8 & 0 \\ 1.1262 \cdot 10^8 & 3.4689 \cdot 10^8 & 0 \\ 0 & 0 & 1.1714 \cdot 10^8 \end{bmatrix}$$

For balanced-symmetric ply orientation

$$E_x := \frac{A_{1,1} \cdot A_{2,2} - (A_{1,2})^2}{A_{2,2} \cdot t}$$

$$E_x = 1.7784 \cdot 10^{11} \text{ Pa}$$

$$E_y := \frac{A_{1,1} \cdot A_{2,2} - (A_{1,2})^2}{A_{1,1} \cdot t}$$

$$E_y = 1.7784 \cdot 10^{11} \text{ Pa}$$

$$\nu_{xy} := \frac{A_{1,2}}{A_{2,2}}$$

$$\nu_{xy} = 0.3247$$

$$G_{xy} := \frac{A_{3,3}}{t}$$

$$G_{xy} = 6.7127 \cdot 10^{10} \text{ Pa}$$

APPENDIX B

Table 6. METCAN Definitions

Property	Symbol	Unit
ELASTIC MODULUS	E	psi
SHEAR MODULUS	G	psi
POISSON'S RATIO	NU	non-dim
THERM. EXP. COEFF.	CTE	in/in/F
DENSITY	RHO	lb/in**3
FIBER DIAMETER	Df	in
HEAT CAPACITY	C	BTU/lb/F
HEAT CONDUCTIVITY	K	BTU-in/HR/in**2/F
STRENGTH	S	psi
MOISTURE EXP. COEFF.	BTA	in/in/1% moisture
MOISTURE DIFFUSIVITY	DP	in**2/sec
THICKNESS	T	in
DISTANCE TO MIDPLANE	Z	in
ANGLE TO AXES	TH	degrees
TEMPERATURE	TEMP	F
STRAIN	EPS	in/in
STRESS	SIG	psi
MEMBRANE LOADS	N	lb/in
BENDING LOADS	M	lb-in/in
MOISTURE	MPC	% by wt
FIBER VOLUME RATIO	Kf	non-dim
FIBER VOID RATIO	Kv	non-dim
PLY RELATIVE ROTATION	DELFI	radian

Table 7. Fiber Properties from METCAN Database

PROP.	UNITS	FIBER CODE NAMES	
		SCS6	SIGM
Df	mils	5.600	3.937
Rhof	lb/in**3	0.110	0.123
Tempmf	Deg. F	2700.000	4870.000
Ef11	Mpsi	57.300	58.000
Ef22	Mpsi	57.300	58.000
Nuf12	in/in	0.260	0.260
Nuf23	in/in	0.260	0.260
Gf12	Mpsi	23.200	23.000
Gf23	Mpsi	23.200	23.000
Alfaf11	Ppm/F	2.700	2.700
Alfaf22	Ppm/F	2.700	2.700
Kf11	BTU/hr/in/F	0.750	0.750
Kf22	BTU/hr/in/F	0.750	0.750
Cf	BTU/lb	0.290	0.290
Sf11T	Ksi	500.000	545.000
Sf11C	Ksi	650.000	1000.000
Sf22T	Ksi	500.000	545.000
Sf22C	Ksi	650.000	1000.000
Sf12S	Ksi	300.000	300.000
Sf23S	Ksi	300.000	300.000

SCS6 SILICON CARBIDE ON CARBON

SIGM (SIGMA) SILICON CARBIDE ON TUNGSTEN

Table 8. Matrix Properties from METCAN Database

PROP.	UNITS	MATRIX CODE NAMES		
		B21S	B21D	B21H
Rhom	Lb/in**3	0.178	0.178	0.178
Em	Mpsi	16.200	12.900	10.300
Num	in/in	0.340	0.340	0.340
Alfam	Ppm/F	6.090	5.280	5.280
Km	BTU/hr/in/F	0.814	0.814	0.814
Cm	BTU/lb	0.142	0.142	0.142
SmT	Ksi	112.000	130.000	45.000
SmC	Ksi	152.000	190.000	65.800
SmS	Ksi	85.000	85.000	32.900
EpsmT	%	1.000	1.200	1.200
EpsmC	%	0.900	1.200	1.200
EpsmS	%	1.000	1.000	1.000
EpsmTOR	%	1.000	1.000	1.000
Kvoid	BTU/hr/in/F	0.019	0.019	0.019
Tempmm	Deg. F	1650.000	1650.000	1650.000

B21S BETA 21S METAL MATRIX

B21D BETA 21S METAL MATRIX (as delivered)

B21H BETA 21S METAL MATRIX (elevated temp)

APPENDIX C

Given: $\sigma_o = \frac{P_f}{A} = \frac{P_f}{t \cdot w}$ $A = t \cdot w$

Define: $\sigma_{net} = \frac{P_f}{A^{star}}$ where $A^{star} = t \cdot (w - d)$

$$\sigma_{net} = \frac{P_f}{A^{star}} \cdot \frac{A}{A} = \left(\frac{P_f}{A} \right) \cdot \frac{A}{A^{star}}$$

recall $\sigma_o = \frac{P_f}{A}$

$$\sigma_{net} = \sigma_o \cdot \frac{A}{A^{star}} = \sigma_o \cdot \frac{t \cdot w}{t(w - d)} = \sigma_o \cdot \frac{w}{w - d}$$

$$\sigma_{net} = \sigma_o \cdot \frac{w}{w - d} \cdot \left(\frac{1}{\frac{1}{w}} \right) \quad \Rightarrow \quad \sigma_{net} = \frac{\sigma_o}{1 - \frac{d}{w}}$$

REPORT DOCUMENTATION PAGE			Form Approved OMB No 0704-0188	
Public reporting burden for this collection of information is estimated to average 1 hour per response, including the time for reviewing instructions, searching existing data sources, gathering and maintaining the data needed, and completing and reviewing the collection of information. Send comments regarding this burden estimate or any other aspect of this collection of information, including suggestions for reducing this burden, to Washington Headquarters Services, Directorate for Information Operations and Reports, 1215 Jefferson Davis Highway, Suite 1204, Arlington, VA 22202-4302, and to the Office of Management and Budget, Paperwork Reduction Project (0704-0188), Washington, DC 20503.				
1. AGENCY USE ONLY (Leave blank)	2. REPORT DATE December 1993	3. REPORT TYPE AND DATES COVERED Master's Thesis		
4. TITLE AND SUBTITLE INVESTIGATION OF COMPRESSIVE BEHAVIOR OF METAL MATRIX COMPOSITES WITH A CIRCULAR HOLE			5. FUNDING NUMBERS	
6. AUTHOR(S) Janet L. Gooder, Captain, USAF				
7. PERFORMING ORGANIZATION NAME(S) AND ADDRESS(ES) Air Force Institute of Technology, WPAFB, OH 45433			8. PERFORMING ORGANIZATION REPORT NUMBER AFIT/GAE/ENY/93D-15	
9. SPONSORING / MONITORING AGENCY NAME(S) AND ADDRESS(ES) Capt. John Pernot WL/MLLN Wright-Patterson AFB OH, 45433			10. SPONSORING / MONITORING AGENCY REPORT NUMBER Capt. K.A. Hart WL/FIBEC Wright-Patterson AFB OH, 45433	
11. SUPPLEMENTARY NOTES				
12a. DISTRIBUTION / AVAILABILITY STATEMENT Approved for public release; distribution unlimited			12b. DISTRIBUTION CODE	
13. ABSTRACT (Maximum 200 words) This study investigated the notched and unnotched macromechanical response due to micromechanical behavior of [0/±45/90] _s SCS-6/β 21S and [0/90] _s Sigma/β 21S subjected to static compressive loads at room temperature. The stress-strain behavior and mechanical response in the presence of a circular hole was examined. A clear description of the progressive nature of damage, which ultimately resulted in failure, was provided. The effect of elevated temperature was shown for SCS-6/β 21S. The ultimate compressive strength and elastic modulus were reported for both MMCs. Sigma/β 21S and SCS-6/β 21S were mildly notch sensitive at room temperature. Notch sensitivity of SCS-6/β 21S was slightly reduced at 650° C. Internal failure mechanisms of fiber debonding, matrix cracking, matrix yielding, fiber failure, and fiber microbuckling were observed in various combinations during the loading. Damage mechanisms were observed similarly in notched and unnotched specimens. Damage initiation in the notched specimens was concentrated in the region adjacent to the hole. Sigma/β 21S and unnotched SCS-6/β 21S at room temperature failed in an extensional mode, while notched SCS-6/β 21S and unnotched SCS-6/β 21S at 650° C failed in a shear mode. The ultimate compressive failure of each depended on the ultimate strength of the fibers.				
14. SUBJECT TERMS Metal Matrix Composite, Elevated Temperature, Compression, Titanium, Silicon Carbide, Sigma, Notch			15. NUMBER OF PAGES 134	
			16. PRICE CODE	
17. SECURITY CLASSIFICATION OF REPORT Unclassified	18. SECURITY CLASSIFICATION OF THIS PAGE Unclassified	19. SECURITY CLASSIFICATION OF ABSTRACT Unclassified	20. LIMITATION OF ABSTRACT UL	